

NOVEL APPROACHES TO SEAFLOOR MAPPING IN THE  
NORTHWEST ATLANTIC

by

Meghan L Troup

Submitted in partial fulfillment of the requirements  
for the degree of Doctor of Philosophy

at

Dalhousie University  
Halifax, Nova Scotia  
August 2023

Dalhousie University is located in Mi'kma'ki,  
the ancestral and unceded territory of the Mi'kmaq.  
We are all Treaty people.

© Copyright by Meghan L Troup, 2023

# TABLE OF CONTENTS

<b>List of Tables</b> . . . . .	<b>vi</b>
<b>List of Figures</b> . . . . .	<b>vii</b>
<b>Abstract</b> . . . . .	<b>xi</b>
<b>List of Abbreviations and Symbols Used</b> . . . . .	<b>xii</b>
<b>Acknowledgements</b> . . . . .	<b>xvi</b>
<b>Chapter 1 Introduction</b> . . . . .	<b>1</b>
1.1 Autonomous Data Collection Platforms . . . . .	2
1.2 Seafloor Mapping Methods . . . . .	3
1.2.1 <i>In Situ</i> Methods . . . . .	3
1.2.2 Optical Remote Sensing Methods . . . . .	4
1.2.3 Acoustic Remote Sensing Methods . . . . .	5
1.3 Acoustic Seabed Classification . . . . .	7
1.4 Objectives . . . . .	10
<b>Chapter 2 Hovercraft Development</b> . . . . .	<b>11</b>
2.1 Introduction . . . . .	11
2.2 Objectives . . . . .	12
2.3 Development . . . . .	13

2.3.1	Hovercraft Design . . . . .	13
2.3.2	Electronics and Navigation . . . . .	14
2.3.3	Sensors . . . . .	14
2.3.4	Software . . . . .	15
2.4	Initial Hovercraft Field Testing . . . . .	16
2.4.1	Study Site . . . . .	17
2.4.2	Tuning Parameters . . . . .	18
2.4.3	Data Processing and Analysis . . . . .	19
2.4.4	Depth Calculation and Rotations . . . . .	20
2.5	Results and Discussion . . . . .	23
2.5.1	Autonomy . . . . .	23
2.5.2	Bathymetry of Horseshoe Island Park . . . . .	29
2.5.3	Cost-Benefit Analysis . . . . .	30
2.6	Conclusion . . . . .	32
<b>Chapter 3</b>	<b>Eelgrass Mapping in Cole Harbour, Nova Scotia . . . . .</b>	<b>34</b>
3.1	Introduction . . . . .	34
3.2	Objectives . . . . .	39
3.3	Approach . . . . .	39
3.3.1	Study Site . . . . .	39
3.3.2	Data Collection . . . . .	40
3.3.3	Acoustic Theory: Near-field and Far-field . . . . .	45
3.3.4	Data Processing . . . . .	46
3.4	Results . . . . .	53
3.4.1	Shallow Water: Seagrass-Transducer Interactions . . . . .	54

3.4.2	Vegetation in Deeper Water . . . . .	59
3.4.3	Effects of Hovercraft Motion . . . . .	66
3.4.4	Transect Comparisons . . . . .	69
3.4.5	Seafloor Segmentation . . . . .	72
3.5	Discussion . . . . .	76
3.5.1	Single Beam Classification . . . . .	79
3.5.2	Evaluating the SWASH System for Seabed Mapping . . . . .	81
3.6	Conclusions . . . . .	82
<b>Chapter 4</b>	<b>Sediment Distribution at Roseway Basin . . . . .</b>	<b>85</b>
4.1	Introduction . . . . .	85
4.2	Objectives . . . . .	88
4.3	Study Site . . . . .	88
4.4	The Data Sets . . . . .	90
4.4.1	Glider Data Collection . . . . .	90
4.4.2	Seafloor Environmental Data Sets . . . . .	93
4.5	Data Processing . . . . .	97
4.5.1	Segmentation Methods . . . . .	97
4.5.2	Impedance and Effective backscattering Coefficient Calculations .	101
4.6	Results . . . . .	110
4.6.1	Seafloor Segmentation . . . . .	110
4.6.2	Effective Backscattering and Reflection Coefficients . . . . .	123
4.7	Discussion . . . . .	132
4.7.1	Environmental Seafloor Data Sets . . . . .	132

4.7.2	Seafloor Segmentation . . . . .	132
4.7.3	Effective backscattering and Reflection Coefficients . . . . .	136
4.7.4	Limitations . . . . .	138
4.8	Conclusion . . . . .	141
<b>Chapter 5</b>	<b>Conclusions . . . . .</b>	<b>143</b>
5.1	Key Findings and Implications . . . . .	144
5.1.1	Seafloor Mapping with Novel Platforms in Shallow Water . . . . .	144
5.1.2	Novel Approaches to Data Analysis for the Purpose of Seafloor Mapping . . . . .	146
5.2	The Future of Ocean Mapping with Uncrewed Vehicles . . . . .	147
<b>Appendix A</b>	<b>Supplementary Materials for Chapter 2 . . . . .</b>	<b>149</b>
<b>Appendix B</b>	<b>Supplemental Figures for Chapter 3 . . . . .</b>	<b>152</b>
<b>Bibliography</b>	. . . . .	<b>164</b>

# LIST OF TABLES

2.1	Autonomous test missions 28 April 2019. . . . .	23
2.2	Monetary value of the SWASH system . . . . .	32
3.1	Hovercraft surveys in Cole Harbour . . . . .	41
3.2	Statistics calculated on each rectangle patch for shallow and deep side-scan backscatter transects. . . . .	51
3.3	Cluster number and classification of feature type for shallow water clusters. Regions that have cluster 5 and 6 bordered by cluster 1 are classified as eelgrass. Cluster 7 only exists at nadir and was omitted from the figures presented in this study. . . . .	56
3.4	Cluster number and classification of feature type for shallow water clusters. Regions which have cluster 5 bordered by cluster 1 are classified as eelgrass. Clusters 6 and 7 only exist at and near nadir and were omitted from the figures presented in this study. . . . .	63
4.1	Glider mission information . . . . .	92
4.2	Descriptions of the geological units at Roseway Basin from <i>Philibert et al.</i> (2022). . . . .	96
4.3	Geophysical and acoustic property estimates for surficial geology units in <i>Philibert et al.</i> (2022). . . . .	109
4.4	Mission 38 clusters by transect . . . . .	110
4.5	Mission 51 clusters by transect . . . . .	113
4.6	Suggested sediment types . . . . .	134
B.1	Hovercraft transects not thoroughly discussed in the main text of Chapter 3 . . . . .	154

# LIST OF FIGURES

2.1	Hovercraft diagram . . . . .	13
2.2	Data collection electronics diagram . . . . .	15
2.3	Navigation electronics diagram . . . . .	16
2.4	Map of Horseshoe Island Park and base station. . . . .	18
2.5	Hovercraft flight path example. . . . .	24
2.6	Differences in heading. . . . .	25
2.7	Differences in direction of motion. . . . .	26
2.8	Accuracy of headings . . . . .	27
2.9	Accuracy of direction of motion . . . . .	27
2.10	Bathymetry at Horseshoe Island Park . . . . .	29
2.11	CHS data compared to Horseshoe Island Park depth data . . . . .	30
3.1	<i>Z. marina</i> global distribution . . . . .	37
3.2	DEM of study site . . . . .	40
3.3	A map of the study site including the spatial distribution of data analyzed in this chapter . . . . .	43
3.4	Segment of Raw ES data before removal of continuous high backscatter returns. . . . .	49
3.5	Single beam echo sounder data in shallow and deeper water. . . . .	49
3.6	Side-scan backscatter standard deviation for (a) high resolution and (b) low resolution. . . . .	51
3.7	Shallow water transect SBES and SSS backscatter data, and ground truth imagery. . . . .	55
3.8	Side-scan segmentation for a shallow water transect: Transect 1, 29 July 2020. . . . .	57

3.9	Single beam echo sounder segmentation for all shallow water transects. . . . .	58
3.10	Individual cluster outputs by k-means clustering for shallow water SBES data. . . . .	59
3.11	Deep water transect, SSS, SBES, and ground truth imagery. . . . .	61
3.12	Raw side-scan backscatter data for Track 2 on 25 September 2020. . . . .	62
3.13	Side-scan segmentation for a deeper water transect: Transect 2, 25 September 2020. . . . .	63
3.14	Single beam echo sounder segmentation for all deep water transects. . . . .	65
3.15	Individual cluster outputs by k-means clustering for deeper water SBES data. . . . .	66
3.16	Hovercraft transect, SSS, SBES, and ground truth images for a transect affected by motion. . . . .	67
3.17	Side-scan segmentation for a transect exhibiting hovercraft motion: Transect 2, 18 August 2020. . . . .	68
3.18	Hovercraft transect, SSS and SBES backscatter data, and classification of a motion artifact. . . . .	69
3.19	Sonar backscatter data compared between for Transect 1, 29 July 2020 and Transect 3, 29 July 2021. . . . .	70
3.20	Sonar backscatter data compared between for Transects 2 on 01 September 2020 and 25 September 2020. . . . .	72
3.21	Side-scan segmentation for all transects in Cole Harbour with a resolution of 50x20 pixels. . . . .	74
3.22	Side-scan segmentation for all transects in Cole Harbour with a resolution of 100x50 pixels. . . . .	75
3.23	An infographic detailing three scenarios that can affect sonar backscatter data. . . . .	76
4.1	Bathymetry of Roseway Basin . . . . .	90
4.2	Physical grab samples in Roseway Basin . . . . .	94

4.3	Roseway Basin surficial geology from <i>Philibert et al. (2022)</i> . . . . .	95
4.4	Slocum glider infographic . . . . .	97
4.5	Backscatter amplitudes from extracted glider downcasts at (a) their original heights above the seafloor (b) after range-normalization. . . . .	100
4.6	Scattering infographic adapted from <i>Jackson and Richardson (2006)</i> . . . . .	103
4.7	Geometry relevant to the derivation of backscattered energy used in this thesis. . . . .	105
4.8	Mission 38 transects . . . . .	111
4.9	Mission 51 transects . . . . .	112
4.10	Segmentation results of missions 38 and 51. . . . .	114
4.11	Box and whisker plot mission 38 . . . . .	116
4.12	Box and whisker plot mission 51 . . . . .	117
4.13	Georeferenced surficial geology map from <i>Philibert et al. (2022)</i> with grab sample data and cluster results. . . . .	119
4.14	Mission 38 transects 5 and 6 normalized seafloor returns . . . . .	121
4.15	Mission 51 transects 3, 6, 12, and 14 normalized seafloor returns . . . . .	122
4.16	Mission 38 effective backscattering coefficients . . . . .	124
4.17	Mission 51 effective backscattering coefficients . . . . .	125
4.18	Reflection coefficients calculated from grab samples and surficial geology units from <i>Philibert et al. (2022)</i> . . . . .	127
4.19	Glider-derived effective backscattering coefficients compared to reflection coefficients calculated from grab samples. . . . .	129
4.20	Glider-derived effective backscattering coefficients compared to estimated reflection coefficients from the surficial geology units in <i>Philibert et al. (2022)</i> . . . . .	131
A.1	Wind direction and speed at two locations on the Halifax peninsula on 28 April 2019. . . . .	149
A.2	Hovercraft Mission 1 from 28 April 2019 . . . . .	150

A.3	Hovercraft Mission 3 from 28 April 2019 . . . . .	150
A.4	Hovercraft Mission 4 from 28 April 2019 . . . . .	151
B.1	Short eelgrass blade measured from end of roots to tallest blade tip collected on 29, July, 2020. This blade measured approximately 15in long. . . . .	152
B.2	Eelgrass blade measured from end of roots to tallest blade tip collected on 29, July, 2020. This blade measured approximately 56in long. . . . .	153
B.3	Hovercraft transect, ground truth, and sonar imagery examples for Scenario C: in which effects created by hovercraft movement can be seen in sonar imagery. . . . .	155
B.4	Side-scan segmentation for Scenario C: Transect 2, 29 July 2020. .	156
B.5	August 18, 2020, Transect 1 . . . . .	157
B.6	July 29, 2021, Transect 1 . . . . .	157
B.7	July 29, 2021, Transect 3 . . . . .	158
B.8	September 1, 2020, Transect 1 . . . . .	158
B.9	September 1, 2020, Transect 2 . . . . .	159
B.10	September 25, 2020, Transect 1 . . . . .	159
B.11	September 25, 2020, Transect 3 . . . . .	160
B.12	September 25, 2020, Transect 4 . . . . .	160
B.13	October 15, 2020, Transect 1 . . . . .	161
B.14	October 15, 2020, Transect 2 . . . . .	162
B.15	July 29, 2021, Transect 2 . . . . .	163

# ABSTRACT

Although oceans cover nearly three-quarters of the earth, studies estimate that only a fraction of the seafloor has been mapped at a resolution higher than  $1km^2$ . On the continental shelf and in nearshore regions, there are significant gaps in information about the seafloor, including sediment and habitat distribution data. Surveying frequently in these regions can be costly, dangerous, and inefficient without the use of uncrewed vehicles. Furthermore, the cost of surveying infrequently is a lack of understanding geophysical or ecological dynamics and processes in these environments. In this thesis, novel uncrewed vehicles are utilized to evaluate whether the data they collect could be used to increase the resolution or accuracy of maps. The design, construction, and testing of an autonomous hovercraft are outlined in Chapter 2. The hovercraft's autonomy was tested via four autonomous flight paths and the desired path was compared to both the observed heading and direction of motion. Although the accuracy is variable, most headings and direction of motion of the hovercraft were within 50 degrees of the desired direction. The hovercraft was then used to map an eelgrass bed in Cole Harbour, Nova Scotia in Chapter 3. Eelgrass was identified visually through sonar imagery and analytically through a classification algorithm. The eelgrass bed was thickest close to the shore of the tidal flat in the very shallow subtidal/intertidal zone and became patchier with deeper water further from the shore. In Chapter 4 seafloor returns from a glider-mounted single-beam echo sounder were used to create maps of the surficial sediment in Roseway Basin. While these gliders are typically deployed to track whales and copepod distributions in the water column, the backscatter from seafloor returns has not yet been used for ground discrimination. Effective scattering coefficients and density-based clustering were used to characterize the surficial sediment, and these results agreed with other seafloor datasets. Each of the chapters in this thesis describes a novel way of using uncrewed data collection platforms for seafloor mapping. By creatively utilizing data collected by these platforms, spatial or temporal gaps created from infrequent monitoring could be filled, which can strengthen our understanding of coastal and shelf waters.

# LIST OF ABBREVIATIONS AND SYMBOLS USED

---

Abbreviation	Description
ACV	Air Cushion Vehicle
ADCP	Acoustic Doppler Current Profiler
ASV	Autonomous Surface Vehicle
AUV	Autonomous Underwater Vehicle
Br	Bedrock
CEOTR	Coastal Environmental Observation Technology and Research
CHS	Canadian Hydrographic Service
D	Derivative
DEM	Digital Elevation Model
DFO	Fisheries and Oceans Canada
ES	Echo Sounder
FF	Feed Forward
GEBCO	General Bathymetric Chart of the Oceans
Gd	Glacial Diamict
GLCM	Gray-Level Co-Occurrence Matrix
GMm	Glacial Marine Mud
GPS	Global Positioning System
GSC	Geological Survey of Canada
I	Integral
IMU	Internal Measurement Unit
LiDAR	Light Detection and Ranging

---

---

Abbreviation	Description
LgSLs	Late Glacial Sublittoral Sand
NONNA	Non-Navigational Bathymetric data
OTN	Ocean Tracking Network
P	Proportional
PCA	Principal Component Analysis
PgMm	Postglacial Marine Mud
PgTsg	Postglacial Transgressive Sand and Gravel
QTC	Quester Tangent Corporation
RTK	Real Time Kinematic
SBES	Single-beam Echo Sounder
SONAR	Sound Navigation and Ranging
SSE	Sum of Squared Errors
SSS	Side-scan Sonar
SWASH	Shallow Water Autonomous Surveying Hovercraft
USGS	United States Geological Survey
USV	Uncrewed Surface Vehicle
VBT	Visual Bottom Typer

---

Roman symbol	Description	Units
$A$	Area	$\text{m}^2$
$c_w$	Sound speed in water	$\text{m/s}$
$c_2$	Sound speed in sediment	$\text{m/s}$
$f$	Sonar frequency	$\text{kHz}$
$k_i$	Wave vector of incident wave	$\text{rad/m}$
$Mz$	Mean grain size	$\phi$
$\langle P \rangle$	Mean complex pressure	$\text{kg m}^{-1}\text{s}^{-2}$
$P_i$	Pressure wave from source (i.e. incident wave)	$\text{kg m}^{-1}\text{s}^{-2}$
$P_i0$	Complex pressure wave from source	$\text{kg m}^{-1}\text{s}^{-2}$
$P_r$	Reflected pressure wave	$\text{kg m}^{-1}\text{s}^{-2}$
$P_s$	Scattered portion of pressure field pressure wave	$\text{kg m}^{-1}\text{s}^{-2}$
$Q$	Full Quaternion	
$q_n$	Quaternion vector	
$R$	Reflection Coefficient	
$RL$	Signal noise ratio	$\text{dB}$
$r$	Range from transducer	$\text{m}$
$S$	Salinity	$\text{ppt}$
$S_b$	Seafloor scattering strength	$\text{dB}$
$SL$	Source level of transducer	$\text{dB}$
$T$	Temperature	$^{\circ}\text{C}$
$TL$	Transmission loss	$\text{dB}$
$V_w w$	Complex reflection coefficient	

Greek symbol	Description	Units
$\alpha$	Sound absorption in water	dB/km
$\alpha_0$	Sound absorption in water	Np/m
$\rho_1$	density of water	kg/m <sup>3</sup>
$\rho_2$	density of surficial sediment kg/m <sup>3</sup>	
$\theta_d$	Desired hovercraft heading	°
$\theta_o$	Observed hovercraft heading	°
$\theta_m$	Observed Hovercraft Direction of Motion	°
$\theta_i$	Grazing angle of incident wave onto seafloor	rad
$\theta_s$	Grazing angle of scattered wave	rad
$\Delta_H$	Difference between desired ( $\theta_d$ ) and observed ( $\theta_o$ ) heading	°
$\Delta_M$	Difference between desired heading ( $\theta_d$ ) and observed direction of motion ( $\theta_m$ )	°
$\phi_s$	Azimuth angle of scattered wave	rad
$\sigma$	Scattering cross section	

# ACKNOWLEDGEMENTS

The old cliché says it takes a village to raise a child, but I'd argue it takes a village to get you through a Ph.D. without losing your mind as well. I've been lucky enough to have a village of my own to keep me sane and relatively happy through it all. The past several years have been the most challenging of my life, but they've also given me more lifelong friends, more knowledge, and more understanding of myself than I ever expected. I am so thankful to those who have helped me make it this far; I don't think I'd be even halfway here without you.

First, I'd like to thank my supervisors, Dr. David Barclay and Dr. Craig Brown for guiding me along the way. David took a chance on me when I applied to Dalhousie with little physics or math background. He's supported me and allowed me to cultivate a project that is both creative and analytic, and encouraged me through even the hardest ups and downs of this degree. While Craig has acted as co-supervisor for less time, his guidance and advice have been absolutely necessary for getting me to this point. I appreciate both for talking me through hard problems and sometimes talking me off a cliff.

I am extremely grateful to my committee members, Dr. Jon Grant, Dr. Alex Hay, and Dr. Sebastian Krastel, for their advice throughout this entire degree. From the beginning, they've given me suggestions and have questioned my own beliefs in ways that have made me a better Oceanographer. They have helped me shape my thesis into something I can be proud to defend.

I'm thankful for the Barclay lab (and lab-adjacent) for their support and their willingness to listen to my practice presentations and talk me through aspects of acoustics that I may

be struggling with. Particularly, thanks to Richard Cheel and Jenna Hare, who helped me gain my footing when I started my degree and had no clue what I was doing, to Matt Hatcher, who taught me things about fieldwork that I didn't realize I didn't know, and to Dave Burns, who's capable hands and calm demeanor got me through multiple field trips with only minor catastrophes. Thanks as well to Emmanuelle Cooke, who made me feel less alone through this process.

A large part of my village over the past six years has been the communities I've been a part of at Dal. DOSA has been integral to my success in grad school both academically and personally. Between the more seasoned students always offering a helping hand when I was freaking out about something academic to the palpable joy at every Friday Bear or Halloween party, the people in this little community have made my time at Dalhousie more than worthwhile, but enriching and exciting. I am also so thankful for the TOSSTies and HOSSTies that I've grown close to over the years, especially Aly, Kirsten, Ben, Ricardo, Masoud, and Patrick. Wherever our next adventures take us, our past adventures will always be some of my favorites.

I'd be remiss without mentioning those who inspired me to pursue my Ph.D. in the first place. I'm thankful for my past supervisors at Coastal Carolina University (Diane Fribance, Erin Hackett, and Roi Gurka), who made Physical Oceanography seem less scary. It's also thanks to my found family from this university that I'm here today; so thanks to the Trash Gang and the Salt Squad for making sure I didn't take myself too seriously.

The support of my family is something that has kept me going throughout my degree. To my Halifax family, Katie, Meg, Meredith, Jess, Sarah, Arie, Raph, Molly, and Connor, thanks for letting me complain and for sharing with me in the weird things I find interesting. Thanks for always offering your support and being down for some (perhaps ill-advised)

shenanigans. Thanks to Erin, the best roommate I had or will ever have for putting up with me, always reminding me to do what I think is right and to save all my bad decisions for Wednesdays. Thanks to my oldest PECO friends, Hannah and Nyx, for being able to pick up where we left off, even if we have stretches of time where we're horrible at keeping in touch. Finally, I'm thankful for my family for always believing that I could do this. Thanks to my mom, Luci, for offering to fight anyone who hurts me, and to my dad, Ron, for always being the one I call when I need help being an adult. And to my siblings, Lindsey, Mitch, and Alex, thank you for supporting me and giving me a push or two when I need it; I couldn't have done this without you.

---

# CHAPTER 1

---

## INTRODUCTION

At an event hosted at Dalhousie University in 2019, six experts debated whether oceans or space would be the next frontier. Two astronauts, Kathryn Sullivan and Joshua Kutryk, and an astrophysicist, Christian Marois, went head to head against a group of marine biologists to argue their points about whether the future of scientific advancement should focus on the stars, or perhaps a bit closer to home, in the depths of the sea. While this event was for entertainment only and ended in a tie between the two groups, the question of where scientific resources are most needed persists. Oceans cover 71% of the earth, and very little of that has been mapped (*Mayer et al.*, 2018; *Wöfl et al.*, 2019). In a paper explaining the Seabed 2030 Project, *Mayer et al.* (2018) estimate that less than 18% of ocean bathymetry has been mapped at a resolution of 1 km and that only a fraction of this information is from high-resolution echo-sounder data. While the bathymetry and geomorphology of the ocean can be linked to sediment distributions, data that can provide information about seafloor properties can also be used in habitat mapping and sediment distribution models (*Finkl and Makowski*, 2016; *Kostylev et al.*, 2001). Increasing the spatial and temporal coverage of seafloor maps is a goal agreed upon by many nations and is considered a main priority for the UN Decade of Ocean Science for Sustainable Development (*Ryabinin et al.*, 2019).

Coasts and continental shelf regions are some of the most diverse and dynamic areas in the world, thus making them important areas for mapping studies (*Mehvar et al.*, 2018;

*Martinez et al.*, 2007). Coastal areas provide homes and food to not only half the world's population, but also a vast number of marine animals including seabirds and marine organisms (*Hanson*, 2004; *McCullough*, 2005; *Mehvar et al.*, 2018). These areas are the focus of many underwater mapping endeavors due to the high biodiversity of the nearshore area as well as the need for increased management in the coastal zone (*Saxena*, 1999). Even though these regions are extremely important ecologically and economically, there are still large gaps in data that large-scale mapping endeavors are consistently aiming to fill. Mapping these areas at high resolutions provides detailed geospatial information which can contribute to environmental data, allowing for a more in-depth study of many processes that occur in these dynamic environments.

## **1.1 Autonomous Data Collection Platforms**

Due to recent advancements in instrument technology, the size and battery demands of sonar instruments have decreased and therefore the use of uncrewed vehicles for seafloor mapping has increased (*Wöfl et al.*, 2019; *Finkl and Makowski*, 2016; *Mayer*, 2006; *Manley*, 2016). These vehicles can also increase the area of regions surveyed, as uncrewed vehicles are smaller than research vessels and are able to collect data in regions where ships cannot maneuver safely, and multiple vehicles may be deployed at once. Autonomous Underwater Vehicles (AUVs) are vehicles that are untethered and move through the water column following a set path. AUVs can move vertically through the water column and therefore can increase the spatial resolution of the data by decreasing the range between instruments and the seafloor (*Finkl and Makowski*, 2016; *Manley*, 2016). These vehicles are equipped with antennae that can transmit data when above the water. Uncrewed Surface Vehicles (USVs) provide a lower-cost alternative to many other surveying platforms (*Patterson et al.*, 2022). These vehicles come in a variety of sizes based on the requirements of physical capabilities and payload and are often designed using accessible materials (*Patterson et al.*, 2022; *Giordano et al.*, 2016; *Ferreira et al.*, 2009). USVs can be remotely operated

or fully autonomous, and have the ability to constantly transmit data. Although some USVs are used in the open ocean and long-term, long-range deployments (CEOTR, 2022; Stepień, 2023), many USVs are used for seafloor mapping surveys in shallow environments (Ferreira *et al.*, 2009; Kimball *et al.*, 2014; Giordano *et al.*, 2016; Jo *et al.*, 2019; Zolich *et al.*, 2022). AUVs and ASVs are equipped with a wide range of instruments tailored to the surveying purpose of individual vehicles. These instruments include oceanographic sensors that collect environmental data such as temperature, conductivity, dissolved oxygen concentrations, and fluorescence, acoustic instruments, and optical imaging instruments among others.

## 1.2 Seafloor Mapping Methods

Mapping benthic ecosystems is vital in order to mitigate the population decline of important benthic species as well as track critical physical processes such as sediment transport and erosion. Mapping surveys tend to be carried out via three methods: *in situ* physical surveys, optical surveys, or acoustic surveys (Finkl and Makowski, 2016). Each of these methods has advantages and disadvantages, and the choice or combination of choices for a particular survey often depends on the desired data resolution or detail as well as the resources available.

### 1.2.1 *In Situ* Methods

*In situ* methods refer to surveys that directly collect data in the field. These studies may use quadrats to determine the coverage of submerged vegetation (Botrel *et al.*, 2022; McKenzie *et al.*, 2001), sediment cores to determine specific grain size and thickness of surface sediment (Sarnthein *et al.*, 2003; USGS, 2014; GSC, 2020), and handheld GPS to determine specific important points relative to the environment of interest (i.e. vegetation or sediment borders). In order to determine other characteristics such as canopy height, sediment type, or estimated biomass, samples of the desired vegetation, sediment, or water

may be collected (*Finkl and Makowski, 2016; McCullough, 2005*). Often these surveys are carried out from shore, from small, crewed crafts (such as kayaks, canoes, or small crafts with engines), or by divers. Thus, this method is neither cost nor energy efficient. If larger-scale or more detailed maps are desired, this method requires spatial interpolation and estimation, which increases uncertainty.

## **1.2.2 Optical Remote Sensing Methods**

Optical methods span a wide range of technologies, from photography to lasers, and vehicles from satellites to airplanes to AUVs. Optical methods have the largest range of spatial sensing resolution (from centimeters to hundreds of kilometers), and can often provide large-scale, high-resolution maps of shallow water areas (*Finkl and Makowski, 2016*). Underwater video and imagery generally provide the highest resolution. These cameras can be towed, dropped on a frame for single-area images, or hull-mounted (*Vandermeulen, 2007*). Often, underwater imagery is used as a ground truth for other mapping methods (acoustic methods, aerial or satellite imagery, or airborne bathymetric lasers), but a towed camera can provide a continuous video stream of the seafloor that can be linked to continuous GPS positions. This technology can be used as the primary method for surveying (*Grizzle et al., 2008*). Imagery acquisition in shallow water can be difficult in regions with high turbidity. Underwater imagery also tends to produce large files that require a lot of time to process and memory to store. While a few studies use underwater imagery alone to map an area, such as *Grizzle et al. (2008); Agrafiotis et al. (2018)*, most use this method in tandem with acoustics for easier processing, more accuracy during different weather regimes, and to include bathymetric measurements (*Gumusay et al., 2019*).

Airborne optical methods include light detection and ranging (LiDAR) techniques, aerial photography, and satellite imagery. These methods can have resolutions of up to  $<1 \text{ meter}^2$  to  $\text{centimeters}^2$  and can span large areas of the earth. Distinct sediment and habitat types can be determined, as well as bathymetry. Mapping via satellite imagery

and aerial photography can utilize both multi-spectral (i.e. ultraviolet, near infra-red, and visible spectrum) as well as hyperspectral (i.e. infrared) to create habitat and bathymetry maps of the seafloor (*Finkl and Makowski, 2016; Bachmann et al., 2010*). Most aerial and satellite imagery stretches from depths of 0-15 meters. In deeper water, the seafloor return is attenuated, and therefore, seafloor properties are not detectable.

Airborne bathymetric lasers are mounted on low-flying vehicles and use a LiDAR technique that can penetrate into the water to determine water depth and seafloor features such as surficial and sub-bottom geomorphological features, surface roughness, and seafloor hardness (*Finkl and Makowski, 2016; Guenther, 2007*). The spatial resolution of the data depends largely on the flying altitude and velocity of the aircraft. Airborne optical mapping methods can be helpful for large-scale mapping endeavors, but they are particularly limited by depth, poor water clarity, and atmospheric visibility. While some of these optical methods have claimed the ability to perform in maximum water depths up to 70 m (*Finkl and Makowski, 2016*), very few areas globally have water clear enough for effective mapping at these depths. These methods, while helpful in distinguishing one habitat from another, cannot often provide important habitat information such as canopy height of vegetation and are therefore used in tandem with other mapping methods. LiDAR and aerial imagery are also often expensive and thus not cost-effective for small-scale, very shallow water studies (*Guenther, 2007*). Reflectance data from optical instruments depends greatly on the geophysical properties of the seafloor, the water depth, and particles or organisms that may be suspended in the water column (*Bachmann et al., 2010; Finkl and Makowski, 2016*).

### **1.2.3 Acoustic Remote Sensing Methods**

Active sounding instruments have been used on ships since approximately 1913 to detect icebergs at a distance, as a direct response to the sinking of the *HMS Titanic*, and have been used for detecting seafloor properties and depth since the 1920's (*D'amico and Pittenger, 2009; Dierssen and Theberge, 2014*). In contrast to electromagnetic waves, acoustic waves can travel greater distances through water than through air and are not

attenuated or absorbed as quickly. Sound wave energy can be lost through spreading and attenuation (including scattering and absorption). At frequencies equal to and less than 1 kHz, attenuation of sound is negligible, however as frequency increases, attenuation also increases (*Lurton, 2002*). Thus acoustic signals with frequencies from 100 kHz to 1 MHz have range limitations from less than 1 km to 100 m respectively. Active sonar (SOund NAvigation and Ranging) instruments are used most often in seafloor mapping, though other acoustic instruments have been used for a few studies, including Acoustic Doppler Current Profilers, passive sonar, and acoustic telemetry (*Gumusay et al., 2019; Descamp et al., 2005; Siderius et al., 2006*).

Sonar is defined by *Lurton (2002)* as systems used for target detection and location. While passive sonar instruments record acoustic signals directly from a target, acoustic sonar instruments record echoes of acoustic signals which are emitted from a source before interacting with the target. Single beam echo sounder (SBES) instruments are widely used for seafloor mapping due to their simplicity (*Blondel, 2010*). These sonar instruments emit a single, conical beam from a transducer and record the properties of the returning waveform, including the amplitude and sometimes the phase of the return. The distance between the transducer and the target object can be determined using travel time and the measured or estimated sound speed in the water column. In the case of seafloor sounding, other properties such as impedance, presence of biology, and canopy height of seagrass or macroalgae can be determined using the amplitude structure of the returned energy (*Lurton, 2002; Sabol et al., 2002; Norton, 2019; Monpert et al., 2012*).

Multibeam echo sounders are another common active sonar used in mapping the seafloor (*Mayer, 2006*). These sonar systems often have two arrays of transducers mounted in a Mill's Cross position, orthogonal to each other, and emit pings in a wide, fan-like projection perpendicular to the ship's heading (*Blondel, 2010; Lurton, 2002*). Returns from each element of the array are then combined using a beamforming algorithm to determine a line segment of bathymetry parallel to the ship's heading. Received returns can be used for

seafloor imaging, and the point of intersection between the transmitted ping and received return is used for range and amplitude measurements.

Side-scan sonar instruments are also commonly used for seafloor mapping purposes (Gumusay *et al.*, 2019). Side-scan sonar transducers are typically mounted parallel to a vehicle's direction of motion and emit a narrow beam perpendicular to the vehicle heading (Cervenka and De Moustier, 1993). The slant range, a line from the sonar transducer to a point on the seafloor, is proportional to the time between the initial sound emitted and the received signal (Lurton, 2002; Blondel, 2010). Changes in the backscatter amplitude of the received signal could be due to the geometry of the seafloor, targets within sediment such as bubbles or shells, or properties of the seafloor such as roughness, density, or sound speed. The heights of features on the seafloor can be estimated using the length of the shadow behind the features, the distance between the transducer and the seafloor, and the slant range between the transducer and features. While interferometric side-scan sonars can collect bathymetry data using the exact angle of arrival of the returned ping, traditional side-scan sonar works under the assumption of a flat seabed for the angle of arrival (Blondel, 2010; Bjørnø *et al.*, 2017). Thus, if this assumption is false, the exact position of the seabed cannot be determined via traditional side-scan sonar. Many studies combine traditional side-scan sonar with single-beam echo sounders to achieve both bathymetry and seafloor imaging (Brown *et al.*, 2011; Gumusay *et al.*, 2019).

### **1.3 Acoustic Seabed Classification**

Seabed classification using sonar returns typically contains two main steps: segmenting the seafloor (i.e. sorting like with like, defining boundaries between different classes of the substrate) and predicting or assigning a class to each category, which can occur in either order. Algorithms for this classification can be unsupervised or supervised which defines the order of operation. Unsupervised algorithms make no assumptions about the nature of clusters but classify data points with similar characteristics together. Once the data is

categorized into separate clusters, *in situ* data and ground truth information are used to assign the clusters meaning (Brown *et al.*, 2011). Alternatively, supervised algorithms assign data points meaning first using *in situ* and ground truth data and separate the data into clusters after.

In categorizing the data, these algorithms tend to use either an image-based approach, a signal-based approach, or a combination of the two (Foster-Smith *et al.*, 2004; Brown *et al.*, 2011; Alexandrou and Pantzartzis, 1993; Gumusay *et al.*, 2019). A signal-based method is typically used when categorizing SBES data (Hamilton, 2001; Brown *et al.*, 2005; Barrell and Grant, 2013; Barrell *et al.*, 2015; Sabol *et al.*, 2002), using the full or partial reflected echo sounder profile. Typically the first echo from a target is used as an indicator of seafloor roughness and the second echo is more sensitive to hardness (i.e. a measure of how much acoustic energy is scattered from the seafloor) (Foster-Smith *et al.*, 2004). In geological and ecological Signal-based classification algorithms use features of the echo sounder return profile such as peak backscatter amplitudes and statistics descriptive of the shapes of the analyzed echoes (Preston *et al.*, 2004; Quester Tangent Corp., 2004; Sabol *et al.*, 2002; Hamilton, 2001).

Image-based techniques are used for swath systems such as multibeam and side-scan sonar (Foster-Smith *et al.*, 2004; Brown *et al.*, 2004; Collier and Brown, 2005; Lucieer, 2008; Brown *et al.*, 2011; McLarty *et al.*, 2020). These techniques can include simply visual identification, in which features visible on the sonar imagery are indicated by a researcher, or automatic identification via algorithms that identify seafloor features based on the sonar backscatter data variability (i.e. backscatter intensity, textural features, variability between pixels) (Foster-Smith *et al.*, 2004; Brown *et al.*, 2004; Lucieer, 2008; Brown *et al.*, 2011; McLarty *et al.*, 2020).

Each of these methods has certain strengths and weaknesses to consider. For example, signal-based segmentation using SBES data typically must be interpolated between points since the spatial range of the data is limited by footprint size and can introduce errors in

these maps (Brown *et al.*, 2005, 2011). However, swath sonar systems (especially side-scan sonar) have a large range of grazing angles which can affect backscatter amplitude and the data must be corrected to account for grazing angles and beam patterns (Lyons *et al.*, 2009; Brown *et al.*, 2011). While grazing angle has less of an effect on scattering from some homogeneous surfaces (i.e. rock, bubbles, live vegetation), heterogeneous and/or patchy surfaces can be greatly affected (Lyons *et al.*, 1994, 2009; Brown *et al.*, 2011). Many recent seafloor mapping surveys use either multibeam sonar or a combination of swath systems and SBES to provide signal- and image-based classification and bathymetry concurrently (Blondel and Sichi, 2009; Brown *et al.*, 2011; Gumusay *et al.*, 2019).

In this thesis, novel platforms and data analysis methods are used to work towards the ultimate goal of producing high-resolution maps with seafloor discrimination techniques. Chapter 2 focuses on the design, construction, and testing of an autonomous hovercraft. Differences between planned autonomous paths and the hovercraft's observed motion are examined to determine the success of the autonomous navigation programming of the hovercraft. Depths calculated from single-beam echo sounder returns are also compared to merged LiDAR and multi-beam bathymetry in this region to determine the accuracy of the sonar instruments and the depth calculation and motion correction methods. Chapter 3 uses this hovercraft platform to map an eelgrass bed in Cole Harbour, Nova Scotia. Submerged vegetation is classified by using the K-means clustering algorithm on SSS and SBES data, and the resulting segments are compared to visual identifications of vegetation in the sonar imagery and ground truth images and underwater video. Finally, Chapter 4 examines seafloor returns from a glider-mounted single-beam sonar for the purpose of ground discrimination. A density-based clustering algorithm is applied to seafloor returns to segment the seafloor based on differences in the backscatter which indicates changes in the geoacoustic properties of the seafloor sediment.

## 1.4 Objectives

This thesis deals with the design, creation, and evaluation of novel uncrewed vehicles as mapping platforms as well as with the utilization of sonar backscatter data to identify geoacoustic properties of targets on the seafloor. The objectives for this project are:

1. To design and construct a hovercraft platform capable of completing autonomous missions in regions where water depth is less than 5m (Chapter 2).
2. To test the effectiveness of the hovercraft platform based on how closely the vehicle followed planned autonomous paths (Chapter 2) and whether the deployed sonar instruments could produce high-resolution and accurate maps of bathymetry (Chapter 2) and *Zostera marina* habitat distribution (Chapter 3).
3. To map the distribution of eelgrass at a shallow-water site (0-3.5m) at a high spatial resolution in Cole Harbour, NS (Chapter 3).
4. To use seafloor backscatter returns from single-beam echo sounders calibrated for short-range zooplankton detection for ground discrimination through density-based clustering of backscatter returns and using effective scattering coefficients as a proxy for sediment type (Chapter 4).

---

## CHAPTER 2

---

# DEVELOPING AN AUTONOMOUS HOVERCRAFT FOR SURVEYING IN SHALLOW WATER

## 2.1 Introduction

In the shallow water region (<5 meters), common mapping methods include LIDAR, hyperspectral imagery, satellite imagery, and acoustic instruments mounted on small crewed vehicles or uncrewed surface vehicles (USVs). Vehicles that use underwater instruments in this region are limited by their maneuverability in the 0-5 meter depth range, as they risk damage by running into obstacles or the seafloor at extremely shallow depths. Even uncrewed surface vehicles (USVs) are depth and bathymetry limited when the steering or propulsion gear is underwater, such as the system evaluated by *Hassan et al.* (2012) whose propulsion mechanism was 0.4 meters below the surface, or the ROAZ II system which has two external motors beneath the water's surface (*Ferreira et al.*, 2009). USVs can decrease their minimum water depth by decreasing size, and therefore maximum weight allotment, such as in a study by *Giordano et al.* (2016) using a small catamaran drone (1.35x0.85 meters), which can be operated in depths of 0-20 meters, but could have difficulty maneuvering as depth approaches zero due to the underwater propulsion mechanisms.

The autonomous hovercraft is a solution to the issues that often arise when surveying in

very shallow and intertidal water (<5 meters). Hovercraft fall into a larger category of air cushion vehicles (ACV) that float on a layer of air emitted by the lift mechanism on the craft. While these vehicles as we know them today were not fabricated or tested until the 1950s, air cushion technology can be traced back to a crewed air cushion platform in 1716 (Amyot, 1989). The Swedish scientist, Emanuel Swedenborg, theorized about a flying machine operated by a human who would force air downwards using two large paddles. Though this technology was never built or tested, it is credited as the first description of air cushion technology used in a flying machine, and is also the first theory to discuss ‘hovering’ rather than simply ‘flying’. Other early air cushion technology includes air lubrication for a torpedo boat built in 1916, a hovertrain designed in 1927, and other air cushion boats developed throughout the late 1920s and 1930s. The hovercraft as it appears today is largely the same design as was developed by Sir Christopher Cockerell in the mid-1950s. This was the first design to include a ring of air for maintaining the air cushion and the first to develop a successful skirt. Each hovercraft has commonalities in fabrication, including a flexible skirt, a lift mechanism (usually fans angled or pointing downward), and the ability to create the air cushion on which they float. A hovercraft’s combination of air cushion and flexible skirt allows these vehicles to be amphibious and all-terrain. For the purposes of the research described in Chapters 2 and 3, these features allow for land-to-water deployment and surveying in water as shallow as the instruments allow.

## **2.2 Objectives**

The objectives for this chapter were to:

- Design and develop a low-cost hovercraft surveying platform with autonomous capabilities.
- Evaluate the accuracy of the platform to navigate a pre-set survey plan autonomously.
- Evaluate the capability of the autonomous platform to map the ocean floor.

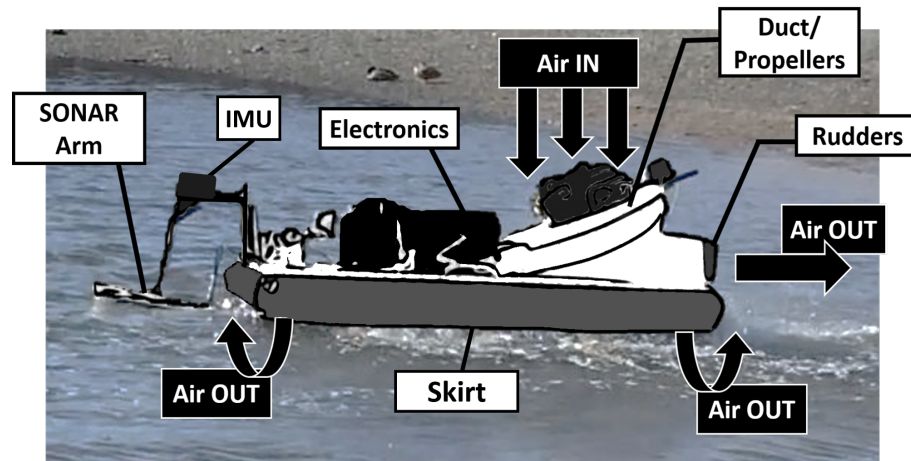


Figure 2.1: Hovercraft diagram showing sensors, electronics, steering, and propulsion as well as airflow through the vehicle.

## 2.3 Development

### 2.3.1 Hovercraft Design

A diagram of the SWASH system’s attributes is shown in Figure 2.1. The hovercraft prototype was constructed using plans from Universal Hovercraft (*Universal Hovercraft*, 2016) and has dimensions of approximately 92 by 183 centimeters. The craft was constructed in 2016, closely following the blueprints provided, however, features were added and adapted between 2016 and 2019 to enhance the platform’s performance during scientific surveys. The craft’s frame is made of plywood and high-density foam coated in resin and fiberglass. It is powered by a single four-stroke gas engine attached to a fan, mounted at an angle to produce both lift and thrust. The hovercraft has a simple vinyl bag skirt with two drainage holes in the aft. A vented box contains a 12-volt boat battery that powers all electronics on the craft. Two waterproof boxes contain the electrical systems and navigation equipment. The steering, which consists of twin rudders placed in the fan’s exhaust, the throttle, and an engine kill switch are controlled by servo motors. A linear actuator controls an aluminum outrigger arm capable of raising and lowering an instrumented outrigger hull, which is boat-shaped and made from high-density polyethylene. The twin rudders used for steering are protected by a curved metal bar, and an aluminum shield around the engine protects

the air intake from water. An exhaust pipe was added to the engine to direct the exhaust away from the hovercraft.

### **2.3.2 Electronics and Navigation**

Electrical systems are split up into two boxes: computing boards, power conversion connections, and onboard computers and navigation equipment. The first (Figure 2.2) is for the onboard computer, side-scan sonar wiring board, and a DC-DC converter which converts 12 volts from the battery to either 5 volts for the onboard computer or 24 volts for the sonar systems. The other waterproof box contains navigation sensors including autopilot, radio telemetry antenna, GPS, and servo motor connections (Figure 2.3). One antenna interfaces with a transmitter, allowing for remote-controlled flight, while the other provides a connection between the base station and the autopilot. A buzzer in the navigation box emits different sounds that indicate the health and connection strength of the autopilot and GPS. A Pixhawk 2.1 autopilot is used to control the servos and linear actuator, and thus control the flight of the hovercraft. The flight path can be pre-determined and programmed into the autopilot, or the hovercraft can be operated remotely via a radio-lined controller.

### **2.3.3 Sensors**

The outrigger hull is mounted with high frequency (800 kHz) Imagenex side-scan sonar transducers with a beam width of 30° wide (perpendicular to transducer heading) by 0.7° long (parallel to transducer heading) and an Imagenex 852 single beam echo sounder (675 kHz) with a conical beam width of 10°. The arm is also outfitted with an XSens inertial measurement unit (IMU) to collect local accelerometer, magnetometer, and gyroscope data to determine the orientation of the outrigger itself. The Pixhawk autopilot contains a set of three orthogonal gyroscopes, three orthogonal accelerometers, and three magnetometers that are used to determine the orientation of the craft. A Global Positioning System (GPS), with Real Time Kinematic (RTK) capabilities, is used to determine the

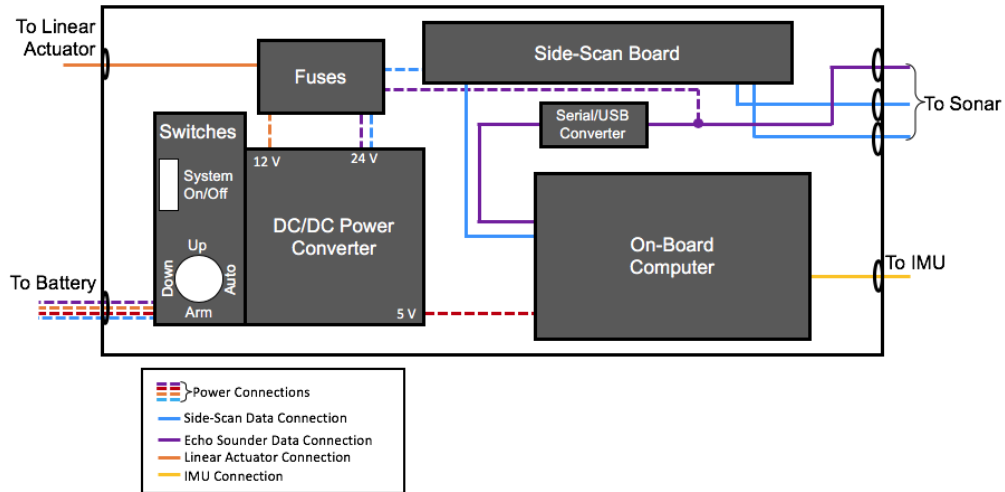


Figure 2.2: Diagram of wired connections between onboard computer, side-scan sonar (SSS), echo sounder (ES), linear actuator (LA), IMU, and battery. Colors indicate the sensor or motor connections and the line style indicates power or data line.

hovercraft’s instantaneous position with a possible maximum resolution of 2.5 centimeters both horizontally and vertically.

### 2.3.4 Software

Data collection for the system occurs on two platforms: the onboard computer logs sonar and motion from the XSens IMU mounted on the outrigger arm and the autopilot logs GPS, IMU, telemetry, and metadata having to do with the autopilot function. Data from both sonar instruments can be collected automatically or manually. Automatically, single-beam echo sounder data is collected from the port using a Python script. Side-scan data is collected automatically using a modified C++ executable provided by the manufacturer. A batch function allows these two codes to be initialized easily before deployment. Data from the XSens IMU is collected using the manufacturer’s software.

Data collected by the autopilot can be assessed in real-time via a telemetry link or analyzed after the deployment using the open-source software, Mission Planner. While a variety of data is collected during deployment to assess the health and connection strength of the autopilot, the user can choose what data is recorded. During the development

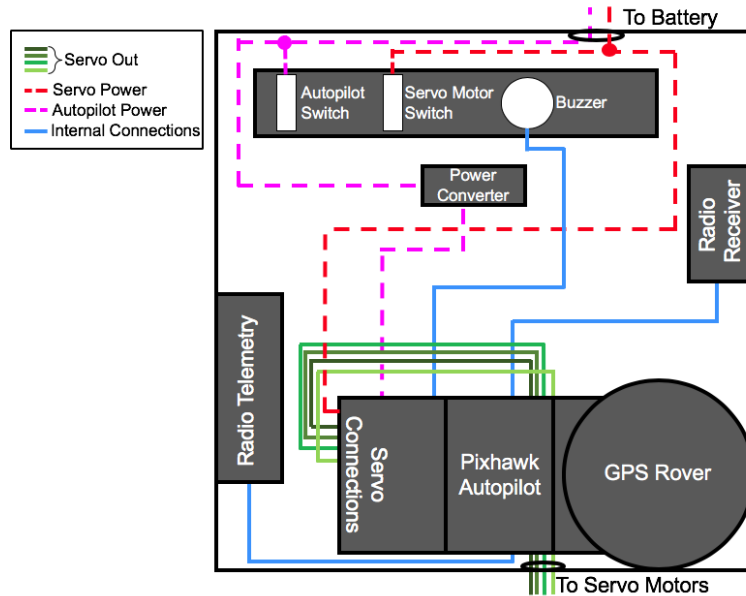


Figure 2.3: Diagram of wired connections for autopilot and associated sensors (including GPS and telemetry).

process, Mission Planner was used to set up sensors and motors on the hovercraft for autonomous and remotely operated use.

## 2.4 Initial Hovercraft Field Testing

During the development process, the hovercraft was tested in different locations and environmental conditions. Land tests were carried out at Wickwire Field at Dalhousie University as well as at Conrose Park, both in Halifax, Nova Scotia. The objective of these land tests was to make sure the SWASH system's controls and programming were working before planning water tests and collecting data. The SWASH system was flown at Williams Lake in Halifax, Nova Scotia in winter to observe how the hovercraft functioned when flying in snowy conditions, and to test how well the vehicle transitioned between surfaces (i.e. land, ice, and water). However, most of the SWASH system field tests in the water were carried out at Horseshoe Island Park in Halifax, Nova Scotia.

## 2.4.1 Study Site

The SWASH system performance was field tested at Horseshoe Island Park beach in Halifax, Nova Scotia (-63.61 W, 44.64 N) as shown in Figure 2.4. Horseshoe Island Park is a small beach along the Northwest Arm that has gently sloped topography and is sheltered from waves. A seawall lines the beach and the water reaches this seawall at high tide. The maximum depth in this area of the Northwest Arm is approximately 6 meters. Tides in this area are semi-diurnal.

The field test analyzed in this study was performed on 28 April 2019, from approximately 9:30 to 11:30 a.m. Low tide, according to measurements collected at a buoy in Bedford Basin (-63.616 W, 44.683 N), occurred between 10:21-10:27 am. According to hourly data from the two closest weather stations: one at Windsor Park (-63.61 W, 44.66 N) and one at the Halifax Dockyards (-63.58 W, 44.66 N), the wind speed increased throughout the morning, and wind direction fluctuated a small amount. A base station, including a laptop computer attached to a telemetry antenna and RTK base station antenna, was set up on top of the seawall. The autopilot was turned on and initialized along with the RTK GPS, which must localize using a number of satellites. The RTK GPS had an accuracy of 1.0 meters for the duration of data collection during this field test. Once the RTK GPS was functional, field tests began, focusing on programming, calibrating, and tuning the hovercraft for autonomous flight. Flight plans were created using the software, Mission Planner, and waypoints were chosen after considering the approximate wind direction and whether there was any wave action in the area. All sensors were turned on and data recording was initialized. The hovercraft was then driven to a spot on the beach and switched into autonomous mode. During the autonomous flight, observations about the hovercraft flight were made, and once the flight was completed and the hovercraft returned to land, these observations were used for tuning parameters.



Figure 2.4: Satellite imagery of Horseshoe Island Park. The base station location on April 28, 2019, is marked with a green pin. The location of Horseshoe Island Park relative to the Halifax Peninsula is shown in the upper right-hand corner and marked with a red pin. The hovercraft was deployed for missions from the beach close to the base station.

## 2.4.2 Tuning Parameters

Tuning refers to changing certain variables within the autopilot that alter the vehicle’s speed, throttle, steering, and navigation. The variables changed during tuning affect the steering and throttle servo motor’s maximum, minimum, and cruising default position. These variables can also affect the vehicle’s motion and speed as it moves toward a programmed waypoint. The website Ardupilot was used as a reference for using Mission Planner for autopilot setup and is especially useful for tuning parameters (*ArduPilot Dev*, 2020).

The SWASH system has one propulsion motor, and therefore one mechanism controlling

both speed and throttle. In addition to managing maximum, minimum, and cruising speeds, this tuning process can also be used to change Feed Forward (FF), Proportional (P), Integral (I), and Derivative (D) gains (Ardupilot Dev. Team 2020). The P gain controls the short-term consistency of vehicle speed. If the P gain is too high for a specific vehicle, the speed will change sporadically. If this variable is set too low, the vehicle will take too long to reach cruising speed. The I gain controls long-term consistency of vehicle speed. The I gain is too large if the vehicle speed is constantly either too low or too high. It is too low if the vehicle does not reach cruising speed. The D gain stabilizes the vehicle speed.

The steering is tuned using the gain parameters as well. The minimum and maximum turn rates for the vehicle can be set. The FF gain affects the turn rate of the steering (or motor-controlling steering). The larger the FF, the faster the turn rate. The P gain again controls the steering on short-term time scales. If FF is set correctly, the P gain for steering is not important. I gain again controls the turning in the long-term turn rates, and the D gain stabilizes. The lateral acceleration control period can be changed to decrease weaving along straight pathways and increase the sharpness of turns, while the lateral acceleration control damping can be changed to improve vehicle control when paths contain many turns and waypoints are close together.

After tuning these parameters on April 28, 2019, four autonomous flight plans were completed during this field test, three of which were performed with the sonar deployed in the water. These four flight plans were used to analyze the accuracy of hovercraft flights.

### **2.4.3 Data Processing and Analysis**

All data were synced to GPS time from the RTK GPS using the two IMU accelerometer data sets. The autopilot IMU data were collected on GPS time intervals while the XSens IMU were collected using the onboard computer, which can have time differences. The GPS time is calculated from GPS week and elapsed seconds since that week began. The two vertical accelerometer time series were cross-correlated and the lag at the maximum peak was used to alter the onboard computer time to match the GPS time.

The hovercraft path accuracy was evaluated using both the observed heading computed by the GPS and the direction of motion. The direction of motion was computed by finding the direction traveled from one GPS coordinate to the next. The accuracy of the hovercraft was determined by wrapping all angles between the range of  $[-180,180]$  before using Equation 2.1 to compute a difference between desired heading ( $\theta_d$ ) and observed heading ( $\theta_o$ ). The desired heading was computed by taking the direction in a straight line from the hovercraft's instantaneous position to the following waypoint. The metric,  $\Delta_H$ , given by:

$$\Delta_H = |\theta_d - \theta_o| \quad (2.1)$$

provides a measure of the performance of the hovercraft's steering controller tuning and directly evaluates the ability of the craft to point its bow at the next waypoint.

Path accuracy between the desired heading and observed direction of motion ( $\theta_m$ ) is computed in Equation 2.2. The metric,  $\Delta_M$ , given by:

$$\Delta_M = |\theta_d - \theta_m| \quad (2.2)$$

is an evaluation of the craft's ability to navigate toward the next waypoint and correct for errors. The first accuracy metric,  $\Delta_H$ , is calculated for every observed heading, and the second accuracy metric,  $\Delta_M$ , is calculated each time the instantaneous hovercraft position changes.

#### **2.4.4 Depth Calculation and Rotations**

To calculate the relative depth of the seafloor, the constant noise signal was first modeled using a single profile from before the sonar was lowered into the water. This 'noise' profile was then subtracted from the entire single-beam data set. A spatial filter was then applied to the single-beam echo sounder profiles such that the bottom return and a second return were still visible. The first return was then isolated and the final maximum backscatter value from this return was determined to be the depth of the seafloor. After the bottom

return was isolated and depth picked from this return, outliers were removed from the depth time series if they were over 2 median absolute deviations (MAD) from a moving median with a window size of 20 points. This bottom return was then corrected for hovercraft movement (pitch, roll, yaw, and heave). As the sonar arm is rigid (i.e. components in motion are at a fixed position to one another) with regards to the geometric center of the hovercraft when the arm is in the downward position, these corrections were calculated with a rigid body rotation.

Perhaps the most common and least complex method of rigid body rotation is using Euler angles (through a rotation matrix or broken up into individual equations). Euler angles (roll, pitch, and yaw) represent three-dimensional changes in orientation about the x, y, and z axes respectively (*Murray et al., 1994; Diebel, 2006*). Rotations using the Euler angles are extremely common because these rotations are easy to visualize, and thus fairly easy to calculate. These angles represent the actual path of rotation and not simply the shortest distance from starting to ending orientation, and therefore each step of the rotation is important. However, these rotations must be performed in a specific order to reach the desired final orientation. For example, depending on the movement of the rigid body, a pitch, roll, and yaw movement may end up pointing in a different direction than a roll, yaw, pitch rotation. Using Euler angles for rotation can also cause a Gimbal lock problem to arise. The Gimbal lock occurs when two axes of the Euler angles line up, decreasing the degrees of freedom by one, and thus decreasing the accuracy of the entire rotation.

Quaternions rotate the rigid body along the shortest path from one orientation to another, thus eliminating the need to know which order the parts of rotation should be completed. Rather than representing angles, quaternions represent a complex algebraic structure (defined in *Diebel 2006*):

$$Q = q_0 + q_1i + q_2j + q_3k \quad (2.3)$$

Where  $Q$  is the quaternion,  $q_0$  is a real scalar and  $q_1, q_2$  and  $q_3$  are real vectors with imaginary components  $(i, j, k)$ . It should be noted that quaternions cannot be split into vectors for rotation like the rotation matrix can, as each vector (or scalar) does not represent a rotation about a single axis. In fact, for a quaternion rotation to yield a correct result, the quaternion must fulfill the unity normalization (or quadratic normalization) constraint:

$$q_0^2 + q_1^2 + q_2^2 + q_3^2 = 1 = \|Q\| \quad (2.4)$$

Where  $\|Q\|$  is called a unit quaternion because it is normalized (equal to ‘unity’). This normalization means that a single quaternion will accumulate errors less quickly than Euler angles. Another advantage of quaternions is the ability to interpolate spherically, allowing for consistent rotation through 3D space when interpolating. While Euler angles are often the preferred method of rotation over quaternions because they are easily visualized and broken up to isolate rotations over one axis, quaternions can offer a more accurate rotation of a rigid body.

After corrections for pitch and yaw were made, the depth data were corrected for changes in water level over the sampling time. Water level data sampled at one-minute intervals from the Bedford Institute of Oceanography station at 44.68°N and 63.62°W were used for this correction. Corrections were performed by locating the shallowest water level datum during the hovercraft sampling period and the echo sounder depth datum that corresponded during that time. The change in water level between the minimum and each previous or subsequent water level were subtracted from the echo sounder depths at each matching time stamp.

The approximate range of single-beam echo sounder footprint radius on the seafloor is between 1.75 cm and 35 cm depending on water depth. The slope of this beach was assumed to be negligible with respect to footprint size because of the shallow depth of water. Water depth was manually collected at one point while the hovercraft engine was

not running to test the accuracy of the correction algorithm. The hovercraft was manually agitated in the water to reach pitch, roll, and heave values similar to those during flight. After processing the depth data, depths were mapped using MATLAB. Land and low-tide line were collected using georeferenced satellite imagery. Depth data provided by the Canadian Hydrographic Service (CHS) were compared to single beam data in Figure 2.11. The CHS depth data were collected using a combination of multibeam sonar collected from 1995 to 2005 and LiDAR collected in 2014. At overlapping coordinates, the shallowest depth was used. The depth data from CHS were subtracted from the data collected with the SWASH system and differences were plotted in Figure 2.11b.

## 2.5 Results and Discussion

### 2.5.1 Autonomy

Four autonomous hovercraft missions were performed on 28 April 2019. Each mission took between approximately 3-6 minutes to complete and all were carried out from 10:10:42 am. Table 2.1 shows the duration of each mission and the number of waypoints planned.

Mission	Duration (minutes)	Waypoints
1	3:02	9
2	5:50	10
3	4:20	7
4	4:13	9

Table 2.1: Autonomous test missions carried out on 28 April 2019, duration of the missions in minutes, and the number of waypoints planned as the missions.

The hovercraft’s autonomous path was tested for accuracy by comparing the hovercraft’s desired heading (straight line to waypoint) to the observed heading and by comparing desired heading with the direction of motion, due to the propensity of the hovercraft to drift (i.e. small  $\Delta_M$ , large  $\Delta_H$ ). Longer hovercraft tracks (A-B, B-C, D-E, F-G, H-I, I-J, flight path 2) are used for evaluating the accuracy of hovercraft autonomy. The results

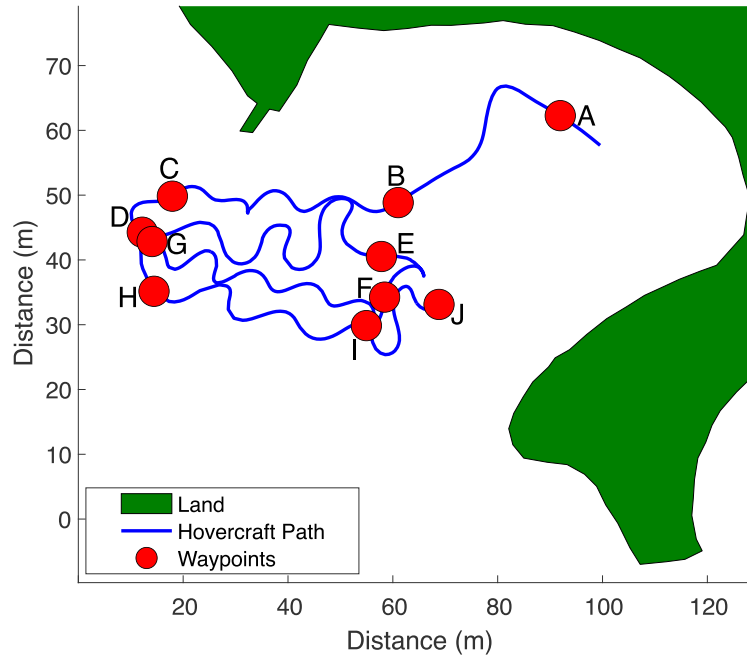


Figure 2.5: Map of hovercraft Flight Path 2. The hovercraft path is shown in blue. Waypoints are labeled by letter and shown by a red dot. Land is shaded in green.

from flight path 2 are fully presented in this manuscript because it was the first full flight path completed with the sonar instruments deployed. Similar analyses were carried out on all flight paths in the process of control system tuning. The hovercraft path and waypoints for the other autonomous missions completed on 28 April 2019 are shown in Appendix A.

The completed flight path 2 track is shown in Figure 2.5. Waypoints were assigned letters in order to identify flight path segments. Polar histogram plots comparing the desired heading (pointing directly to the next waypoint) versus the observed heading are shown in Figure 2.6. Bars show the direction of the observed heading, and the inner dashed circles represent the frequency of headings. The bin width for each bar is 10 degrees. Darker reds indicate that the observed heading for each track was closer to the desired heading. Some plots show a wider range of low differences because the desired heading changes as the position of the hovercraft changes.

The selected flight plan had a total of 10 tracks, six of which will be discussed in this manuscript. Headings for tracks A-B (Figure 2.6a) are uniform as well as accurate, with

most observed headings pointing in the south/southwest direction and falling within 20 degrees of the desired heading. Other tracks for this mission, including B-C, D-E, F-G, H-I, and I-J (Figure 2.6b-2.6f) exhibit higher variability in observed headings. Tracks D-E and I-J (Figure 2.6c, 2.6f) in particular have a higher percentage of large  $\Delta_H$  values.

The  $\Delta_M$  values were evaluated for the six tracks from flight path 2 in Figure 2.7. While higher variability in direction of motion is shown in tracks B-C, D-E, F-G, and I-J (Figure 2.7b, c, d, and f) similar to Figure 2.6, the variability in the direction of motion is less than the variability of observed headings. While differences of 120 to 140 degrees are shown in Figure 2.6c, e, and f, the maximum differences in Figure 2.7 are approximately 100 degrees. The increases in  $\Delta_M$  and  $\Delta_H$  do not consistently occur at similar points between flight paths. The direction of motion shows a more accurate path than the observed headings for this flight path.

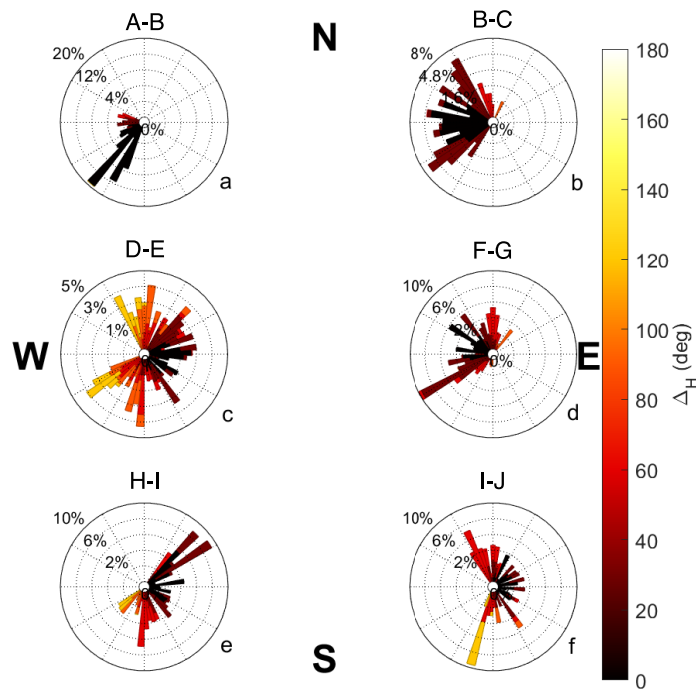


Figure 2.6: Differences in headings for each long track in Flight Path 2. Directions indicate the observed headings and vector length is a factor of heading frequency. The color indicates the difference between the observed ( $\theta_o$ ) and the desired heading ( $\theta_d$ ).

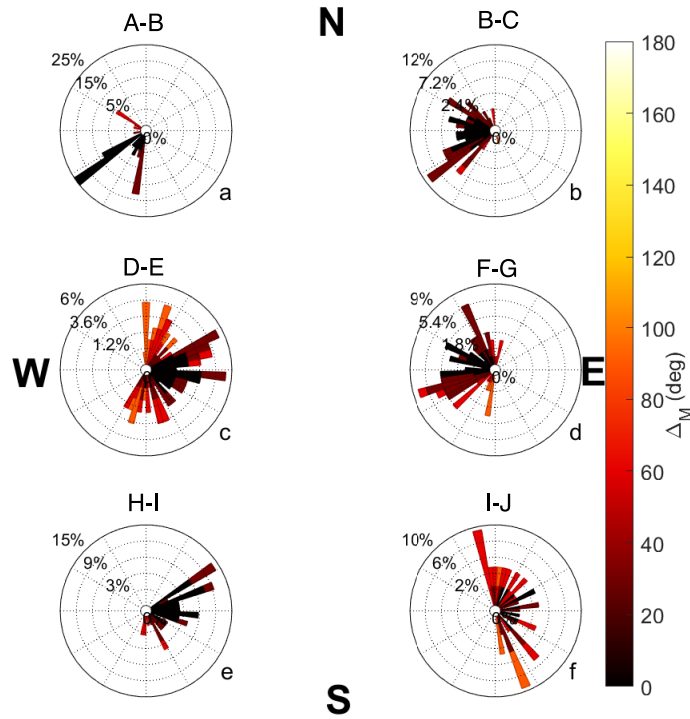


Figure 2.7: Differences in direction of motion and the desired heading for each long track in Flight Path 2. Directions indicate the observed headings and vector length is a factor of heading frequency. The color indicates the difference between the direction of motion ( $\theta_m$ ) and the desired heading ( $\theta_d$ ).

The delta values are compiled for all four flight paths completed on 28 April 2019, in Figures 2.8 and 2.9. Differences are binned in 30-degree groups and the percent of headings per track are computed. Figure 2.8 shows  $\Delta_H$  values. Mission 1 is the most accurate with all differences less than 90 degrees. Flight paths 2 and 3 both have  $\Delta_H$  values exceeding 120 degrees, and Flight path 3 has the largest  $\Delta_H$  values of 150 degrees. When  $\Delta_M$  is evaluated in Figure 2.9, the  $\Delta_M$  and  $\Delta_H$  values differ for each mission, but the trends are similar between these two methods. Flight paths 1 and 4 both show a higher percentage of differences close to zero. Tracks in flight path 3 also show a higher percentage of small differences both centered around 0 and 30 degrees.

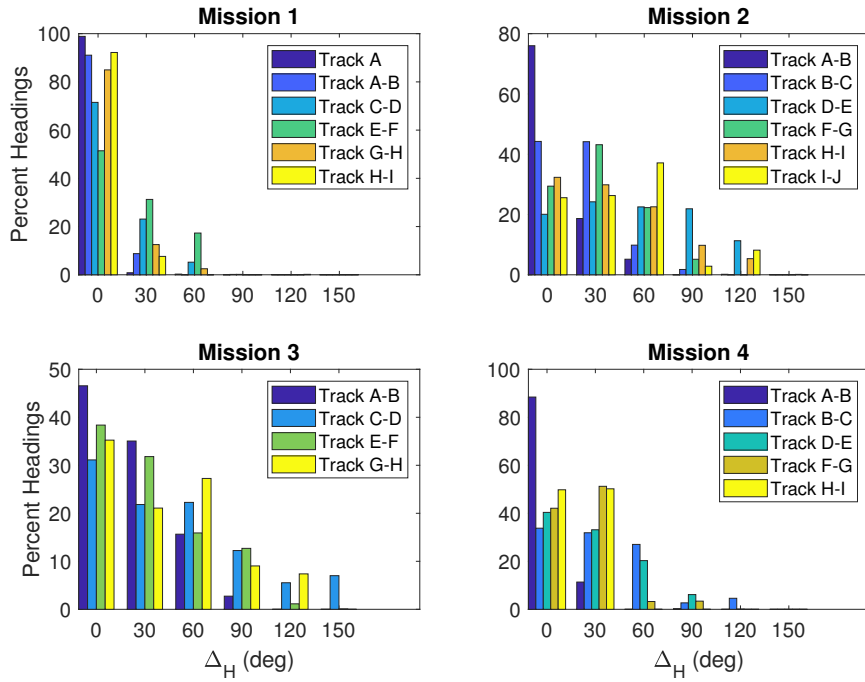


Figure 2.8: Histograms showing differences in desired heading ( $\theta_d$ ) and observed heading ( $\theta_o$ ) for non-turning tracks for each mission completed on 28 April 2019.

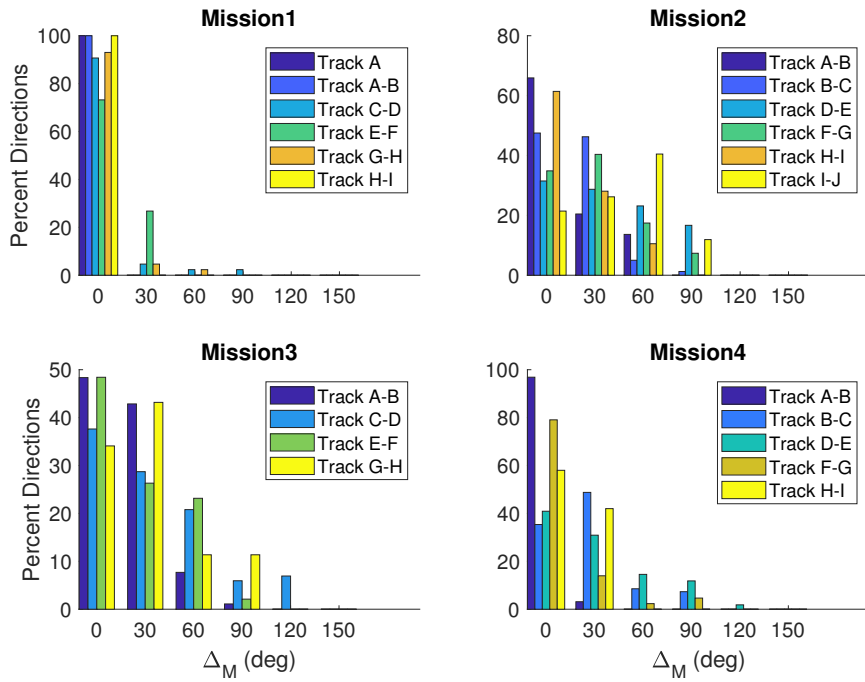


Figure 2.9: Histograms showing differences in desired heading ( $\theta_d$ ) and direction of motion ( $\theta_m$ ) for non-turning tracks for each mission completed on 28 April 2019.

The hovercraft is able to reach the planned waypoints for every flight path. In every case, when  $\Delta_H$  values are compared with  $\Delta_M$  values, the latter is less variable and more accurate, creating a more accurate metric for analyzing hovercraft performance. Figures 2.8 and 2.9 both indicate that flight paths 1 and 4 are more accurate than flight paths 2 and 3, due to a higher proportion of delta values between 0 and 60 (and thus lower proportion of delta values between 60 and 180). The sonar arm was deployed for flight paths 2-4, suggesting that the accuracy of flight path 1 is due to the lack of drag generated by instruments in the water. Hovercraft flight can be affected by factors external to the system such as wind speed and direction, wave action, current speed, and surface slope, or internal factors such as skirt inflation, parameter tuning, and engine performance. Any combination of these factors could cause hovercraft flight accuracy to decline.

Wind data from April 28, 2019, collected from the Halifax peninsula shows the wind speed increasing throughout the field test, indicating that some of these external factors were present and could have affected the accuracy of the hovercraft. Wind direction from the Halifax Dockyards and Windsor Park changed by 10 degrees over the hour during which data was collected, although, based on observations during surveying, the wind direction changed much more frequently. If the hovercraft path was parallel to the direction of the wind, the accuracy of the direction of motion was likely to be higher, however, if the wind direction was perpendicular to the hovercraft path, the accuracy decreases as the hovercraft can be blown off track easily due to the near-friction-less motion against the water or ground surface. During the missions in which the sonar arm was in the water, water speed may have also had an effect on the accuracy of the hovercraft, as the tide switched between ebb and flood during these autonomous surveys. Regardless of the differences in accuracy between flight paths, they were all deemed successful because they managed to reach programmed waypoints without going too far off track.

## 2.5.2 Bathymetry of Horseshoe Island Park

During an average hovercraft flight, the pitch and roll (two rotations that affect perceived echo-sounder depth the most) rarely reach above half the conical beam width of the echo-sounder (5 degrees) and thus, corrections on ping-by-ping measurements are very small. The majority of these corrections come from adding the measured depth of the echo-sounder below the water's surface onto raw echo-sounder depth, unlike a typical survey boat or towed vehicle which will have significant heave, pitch, roll, and other motion corrections.

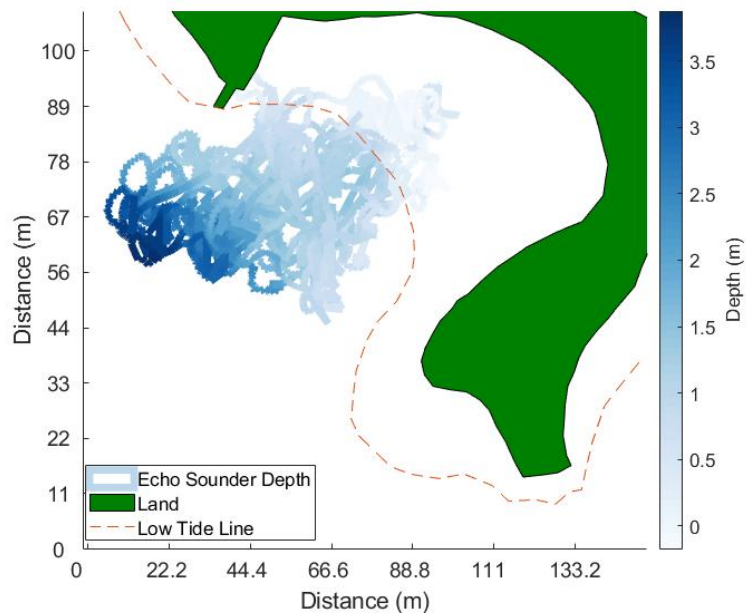


Figure 2.10: Map of Horseshoe Island Park with bathymetry collected with the hovercraft's single-beam echo sounder. The land is filled in with green, the low tide line is indicated by the red, dashed line.

Echo-sounder depths over the hovercraft's flight path are shown in Figure 2.10. The land is green and the low-tide line is shown by a red, dashed line. At high tide, the water can reach the seawall (land boundary). Single-beam echo sounder data from the entire surveying period is shown, regardless of manual or automatic mode. The bathymetry in this area is shallow and the echo sounder was able to map the gently sloping beach.

In Figure 2.11b, the bathymetry from the single-beam sonar is compared to existing multibeam sonar and LiDAR depth data provided by the Canadian Hydrographic Society (CHS). These data show a gently sloping beach, which supports visual observations made at the study site. When the CHS data is subtracted from the single-beam depth data, the differences are more apparent. Positive values indicate that either our data were greater (i.e. more positive) or that the CHS data were much more negative (i.e. LiDAR measurements on land), while negative differences suggest that CHS data were greater than ours. Larger differences can be seen around the edges of the single-beam sonar data path and especially along the low-tide line. The largest difference can be seen in the top left-hand corner of the data, where differences were greater than 2 m. These differences are larger than what is acceptable in terms of the International Hydrographic Organization’s (IHO) standards (IHO, 2020). Some differences in depth could be due to sediment transport changing the local geomorphology and the water level data used for tidal corrections being inaccurate for this area.

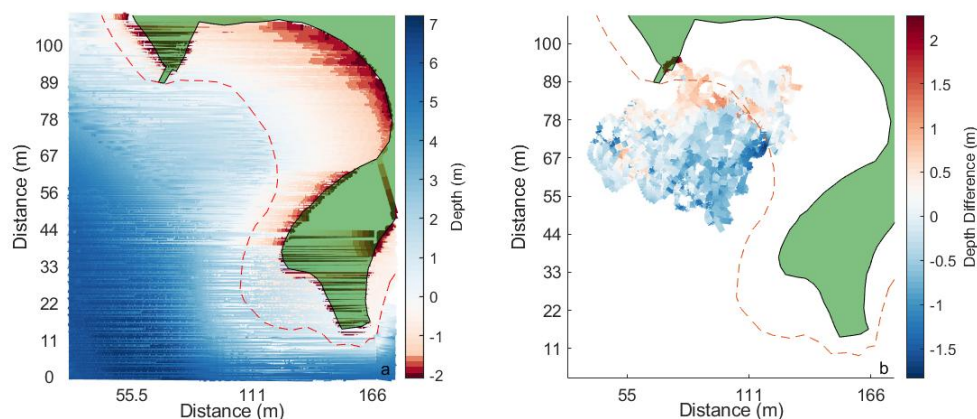


Figure 2.11: Bathymetry from multibeam and LiDAR data (a) from the Canadian Hydrographic Society in the Northwest Arm, Halifax. CHS bathymetry is subtracted from Hovercraft bathymetry in (b). The low-tide line is indicated with the red, dashed line. Land is shaded in green.

### 2.5.3 Cost-Benefit Analysis

A main benefit of the SWASH system is cost efficiency when compared to other shallow water mapping methods (i.e. LiDAR, airborne photography). Table 2.2 outlines the

approximate cost of development for this system, including the Sonar instruments. The sonar instruments comprise the majority of the cost of this system, with the echo sounder costing almost \$2,100 CAD and the side-scan sonar costing over \$7,000 CAD. The total cost of the SWASH system is approximately \$16,000. With sensors included, this platform is comparable in price to high-end Uncrewed Aerial Vehicles (UAVs) with a high-definition camera and RTK GPS. These systems can run between a few thousand dollars at the low end, to approximately \$20,000 at the high end (*DJI*, 2021). While photogrammetry can be extremely useful for mapping habitats and some sediment distribution, it cannot collect bathymetry data. Bathymetric LiDAR systems can, of course, collect bathymetry but these instruments are much more expensive, typically bringing the cost of these UAVs to \$50,000 up to \$300,000 (*Leica Geosystems AG*, 2021). The risk of using UAVs can also be relatively high if the vehicles (and instruments) are not entirely waterproof. While fully waterproof UAV options do exist, many photogrammetry and even LiDAR systems (including UAVs and instruments) are only water resistant, not fully waterproof (*DJI*, 2021). Thus, for scenarios in which mechanical failure occurs and the vehicle may fall into the water, waterproof or floating options such as the SWASH system can be less of a financial risk.

Uncrewed Surface Vehicles (USVs) are just as varied as UAVs in terms of price and complexity. For example, a low-cost USV for water quality monitoring can cost as little as \$200 (*Jo et al.*, 2019), while autonomous USVs such as the Jetyak can cost up to \$15,000 excluding the cost of scientific instruments (*Kimball et al.*, 2014). Most other USVs, including the Jetyak, have their propulsion mechanisms underwater and thus have difficulty maneuvering in extremely shallow water (<1m) and could cause a significant amount of damage to benthic habitats at these depths (*Tyler-Walters and Arnold*, 2008).

When determining the cost-benefit analysis of a novel platform, it is important to discuss the attributes of the system and compare it to other similar surveying methods. Similar to UAVs, this system can survey the extremely shallow water region and is non-invasive

to the benthic ecosystem. Like other ASVs, the system is at low risk of damage in water and contains instruments that can work well in water with high turbidity. In terms of cost, the hovercraft itself is quite inexpensive to produce ( <\$10,000), and the instruments used are also fairly low-cost in comparison to many other systems. In addition, no extra cost is necessary to deploy the system, unlike other ASVs which sometimes require deployment from a ship. Thus, the SWASH system is a cost-efficient method of filling gaps in shallow water surveys.

<b>Item</b>	<b>Cost</b>
Hovercraft kit	\$625
Echo Sounder	\$2,090
Side-Scan Sonar	\$7,015
Autopilot and GPS	\$1,095
Other Electronics	\$200
Approximate Technician Cost	\$5,000
Total	\$16,025

Table 2.2: Approximate monetary value of SWASH system is outlined.

## 2.6 Conclusion

The autonomous hovercraft represents a low-cost, low-risk surveying platform that can be deployed for high-resolution benthic monitoring and bathymetry mapping projects in relatively small areas. While there are significant challenges that arise when creating an autonomous craft, including the vehicle’s proclivity to drift, and the power being split between lift and thrust as a consequence of a single, tilted gas engine, the autonomy of the platform has been ultimately successful. The hovercraft system development was deemed successful because the vehicle could complete a flight path with both the sonar instruments in and out of the water. Though accuracy can vary from mission to mission and track to track within missions, collecting these statistics can infer important information about what parameters need to be altered to increase the accuracy of these autonomous flight paths. Consideration must be made with respect to the types of sensors deployed in the

water due to hovercraft movement. The observed drifting does not affect the accuracy of downward-pointing instruments such as the single-beam sonar, nor would it affect non-imaging instruments such as those surveying conductivity, temperature, and depth (CTD), current meters, or other instruments of these types. Mapping the bathymetry of the Horseshoe Island Park beach was deemed successful due to the accuracy of the depths corrected for motion compared to the measured depths. The beach slope is very gradual, but a noticeable increase in slope occurs past the low-tide line.

When collecting bathymetry with a single beam echo sounder, the hovercraft's difficulty in following straight tracks is not an issue, and can actually provide data with high spatial resolution and coverage at a study site when data from several autonomous missions are combined. However, when mapping using side-scan imagery, a straight track is necessary to minimize motion artifacts and improve the quality of mosaics. While no quantitative analysis on hovercraft pilot performance was carried out, observations made during field testing show that the hovercraft's variation in the heading is easier to correct manually than autonomously. Thus for subsequent surveys discussed in the following chapter of this thesis, the hovercraft was flown manually which typically allows the hovercraft to have a straighter track.

---

## CHAPTER 3

---

# USING A REMOTELY-OPERATED HOVERCRAFT TO MAP EELGRASS IN COLE HARBOUR, NOVA SCOTIA

### 3.1 Introduction

Seagrasses are flowering plants that grow in both intertidal to subtidal regions of the littoral zone in marine or brackish waters (*Green and Short, 2003*). As of 2019, 76 species of seagrass have been identified worldwide, the dominant species in the North Atlantic is *Zostera marina*, commonly known as eelgrass. *Zostera marina* is a perennial species of seagrass that can be found in the North Atlantic stretching northward from North Carolina and Portugal as far north as 60 degrees latitude (Figure 3.1, (*Short et al., 2007*)). The growing season for this seagrass varies over latitude, occurring approximately between March and October, until the decrease in light and temperature causes the shoots and leaves above ground to die off, leaving much of the root system alive (*Thayer et al., 1984*). Growing seasons in the higher latitudes will have slower flowering and will be more delayed into the fall for the annual winter die-off of above-ground biomass. These plants usually grow in soft sediments such as mud, sand, and occasionally gravel mixed sediment. Eelgrass plants have short roots growing from a horizontal rhizome and thin blade-like leaves with rounded tips that sprout from sheaths, each containing 2 to 5 leaves. Blades typically grow between 20 cm and 2 meters long and 3 to 12 millimeters in width (*Moore*

and Short, 2007). Eelgrass can grow in a wide range of coastal habitats. Thus, it follows that the specific morphology can vary from bed to bed due to environmental factors such as temperature, salinity, light availability, wave action, currents, substrate, and nutrient availability (Thayer *et al.*, 1984).

Seagrasses are considered foundation species that provide habitats for benthic or pelagic species, food resources, and stability for underlying sediment due to their root systems. In the North Atlantic region, eelgrass is a known nursery habitat for cod and other species of fish, a main source of nutrients for waterfowl such as Canada geese, certain species of ducks, and Common and Barrow's Goldeneye (Hanson, 2004). These beds provide habitats for many benthic species including sand shrimp and scallops. They also act as a significant carbon sink and oxygen source during the growing period (Thom *et al.*, 2001; Röhr *et al.*, 2016, 2018; Marbà *et al.*, 2018). *Zostera marina* detritus can also become part of the open ocean food web when it is transported offshore (Neckles *et al.*, 2009).

*Zostera marina* is threatened by various biological, geological, and chemical changes in the environment (Barrell, 2009; Thayer *et al.*, 1984; Murphy *et al.*, 2021). Though eelgrass tolerates a wide range of temperature and salinity, higher temperatures can cause the seagrass to be more susceptible to disease (Barrell, 2009; Thayer *et al.*, 1984; Green and Short, 2003; Moore and Short, 2007). Eelgrass mortality may also be caused by nutrient loading or low oxygen in sediments (Green and Short, 2003; Murphy *et al.*, 2021; Moore and Short, 2007). Eelgrass is also sensitive to light availability and can thus be threatened by algal growth. In Nova Scotia, *Z. marina* populations can also be in danger of depletion by the invasive European green crab, *Carcinus maenas* (Garbary *et al.*, 2014). This species of seagrass is also susceptible to eelgrass wasting disease, a disease caused by pathological slime mold *Labyrinthula zosterae* (Short *et al.*, 1987, 1986; Thayer *et al.*, 1984). While this mold can exist within an eelgrass bed without much die-off, when an outbreak of the disease occurs, mass mortality of the eelgrass bed will inevitably follow (Hanson, 2004). In the north-western Atlantic in the 1930s, eelgrass wasting disease caused the mortality

of approximately 90% of eelgrass beds, much of which recovered by the 1960s. A similar phenomenon occurred in this region in the late 1980s, first recorded in New Hampshire's Great Bay Estuary before spreading both north to Atlantic Canada, and south towards the lower limit of *Zostera marina* in North Carolina (Short *et al.*, 1986, 1987). Eelgrass populations in the North Atlantic have been fluctuating since the end of this most recent bout of eelgrass wasting disease. A technical report by the Canadian government about the status and conservation of *Zostera marina* in 2004 noted an average decline of 79.5% of eelgrass population in four surveyed inlets off the coast of Nova Scotia between 1992 and 2002 (Hanson, 2004; McCullough, 2005). The same report discussed eelgrass population decreases in the estuaries of the Gulf of St. Lawrence between 2001 and 2003. While eelgrass wasting disease has previously been disastrous for *Zostera marina* populations, most recent declines in eelgrass beds have been credited to a decrease in water quality caused by anthropogenic sources (Gumusay *et al.*, 2019; Neckles *et al.*, 2009; Paling *et al.*, 2009).

The decreasing trend in *Zostera marina* population has spurred studies in Europe and North America for monitoring, mitigation, and restoration efforts (Gumusay *et al.*, 2019). The first recorded attempt at restoration occurred in Europe in 1939, after a fisherman tried to transplant eelgrass that had been decimated by wasting disease (Paling *et al.*, 2009). Some common methods of restoration include transplanting eelgrass with sediment cores, with bare roots and rhizomes into existing sediment, or by seeding an area (Eriander *et al.*, 2016). Restoration efforts continued throughout the twentieth century, with varied success (Paling *et al.*, 2009). Most species of seagrass are quick to respond to environmental pressures leading to population loss but are slow to recover (Paling *et al.*, 2009; Murphy *et al.*, 2021; Green and Short, 2003).

Regardless of these successful transplants, there are still challenges posed by seagrass restoration. Each site proposed for restoration should fit a series of criteria that indicate the location can support and sustain an eelgrass bed long-term. These criteria include

having similar depth, water flow, and anthropogenic disturbances as the sites from which the eelgrass is harvested (*Paling et al., 2009; Murphy et al., 2021*). Restoration is often difficult to perform due to site location and available personnel, but it can also be extremely costly. On a large scale, these restorations can cost as much as \$972K per hectare (*Paling et al., 2009; Moore and Short, 2007*). Even on smaller scales, these restorations can still be twice the price of a terrestrial habitat restoration project, and therefore cost-ineffective for small areas. A more reasonable conservation effort is mitigation and preservation through monitoring and taking measures to improve water quality and decrease anthropogenic disturbances (both physical and chemical). Thus, the focus should be on mapping and monitoring these ecosystems in order to prevent losses (*Murphy et al., 2021; Moore and Short, 2007; Paling et al., 2009*).

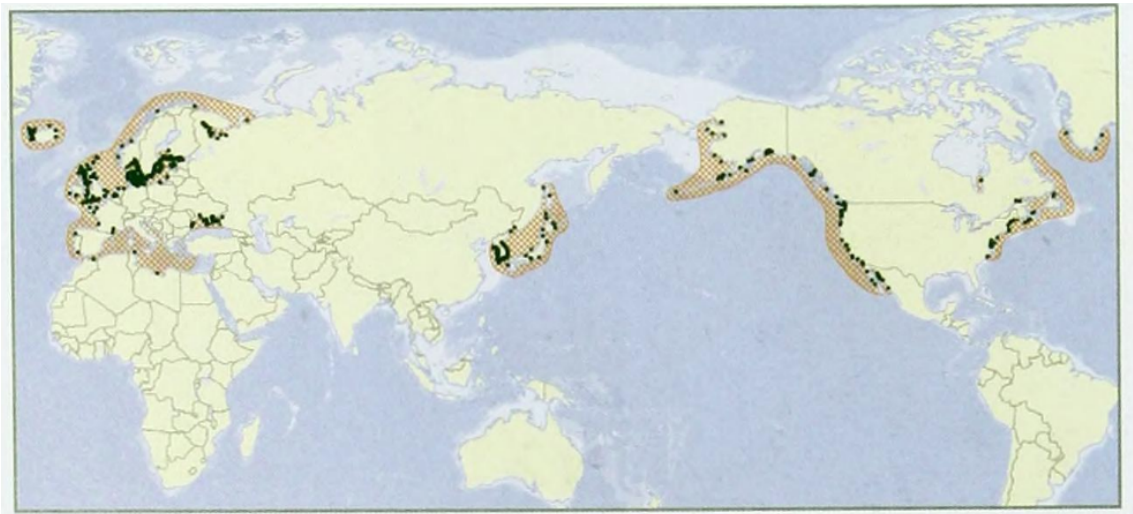


Figure 3.1: Global distribution of *Z. marina* from *Green and Short (2003)* .

Since eelgrass must grow in the photic zone, these mapping endeavors use both optical and acoustic remote sensing techniques. Many surveys use satellite imagery, aerial photography, or a mix of the two (*O'Neill and Costa, 2013; Wilson et al., 2019; Costello and Kenworthy, 2011*). Towed underwater video or drop cameras are also common eelgrass mapping or ground-truthing practices (*Schubert et al., 2015; Hanson, 2004; Möller,*

2017). Acoustic remote sensing techniques are often used for seagrass mapping, using in conjunction with underwater video or other optical methods such as satellite imagery for ground-truthing (*Gumusay et al.*, 2019). Multi-beam echo sounders are used more frequently in seagrass mapping surveys in recent years, however side-scan systems and single beam echo sounders are still commonly used (*Gumusay et al.*, 2019; *Stocks et al.*, 2019; *Ferretti et al.*, 2017; *McLarty et al.*, 2020; *Greene et al.*, 2018).

In Cole Harbour, Nova Scotia, wetland environments including eelgrass were mapped using aerial photography taken in 1992 and again in 2002 (*Hanson*, 2004; *McCullough*, 2005). These studies discovered a 49% decrease in eelgrass within this decade with no discernible reason for the population decline. The maps published by *McCullough* (2005) are low resolution and do not accurately present the eelgrass cover as it is today. Recently, *O'Brien et al.* (2022) used species distribution models to predict eelgrass presence and absence along the Atlantic coast of Nova Scotia at a resolution of approximately 30m. Imagery from Landsat satellites in which turbidity and cloud cover are both low and light is able to penetrate to the vegetation in this region are rare and have spatial resolutions too low to capture the eelgrass distribution in Cole Harbour in detail. Lower flying optical systems, such as uncrewed aerial vehicles (UAVs) could provide increased resolution, though in Cole Harbour, the flying of these vehicles is restricted (*National Defence*, 2021). Acoustic surveys can therefore offer a potentially attractive alternative methodology for monitoring and can provide high-resolution backscatter from the seafloor (*Malthus and Mumby*, 2003). Thus, a platform that can be used to monitor the eelgrass in this region with a regular frequency could provide more information about the local eelgrass population dynamics.

In this study, the SWASH system, described in Chapter 2, was evaluated for field performance while mapping a shallow eelgrass bed in Cole Harbour. Because this system is a USV with no propulsion mechanisms under the surface of the water, this system can provide a useful solution that is non-invasive to the environment and can be operated

regardless of drone restrictions. Side-scan and single beam echo sounder instruments are used in conjunction to provide both depth and sonar imagery to identify submerged vegetation. K-means clustering is used on statistics calculated over the sonar backscatter data to automatically group similar backscatter returns. The success of the SWASH system as a mapping platform for depths 0-3.5 m was evaluated based on results from the sonar backscatter as well as the performance of the hovercraft as a vehicle in this region.

## 3.2 Objectives

The objectives for this chapter were to:

- Map eelgrass distribution at high resolutions in Cole Harbour, NS from single beam and side-scan sonar data using manual (i.e. visual) and automatic classification techniques.
- Evaluate the performance of the SWASH system as a platform for mapping nearshore, shallow water habitats.

## 3.3 Approach

### 3.3.1 Study Site

Field studies for mapping eelgrass were carried out in Cole Harbour, Nova Scotia, near Rainbow Haven Beach. Cole Harbour is an inlet that has an approximate area of 15km<sup>2</sup> and is shielded from the open ocean by Rainbow Haven Beach. This region is comprised of salt marshes and shallow tidal flats that are periodically altered morphologically by fast currents in a deeper tidal creek. Vegetation surrounding these tidal flats includes *Spartina* in the intertidal zone, eelgrass (*Zostera marina*) in the shallow subtidal zone, and algae that grow sub-tidally.

The region of interest within Cole Harbour is bounded by Cow Bay Road to the south and the Salt Marsh Trail to the north. Eelgrass was previously mapped at this site in a

technical report by *Hanson (2004)*. A small eelgrass patch was visually identified close to Deployment Site 2 (Figure 3.2) in late September 2019. The bed was mapped from July-October of 2020 and again in July 2021, when visual investigations showed a much larger ground cover of eelgrass during the growth season.

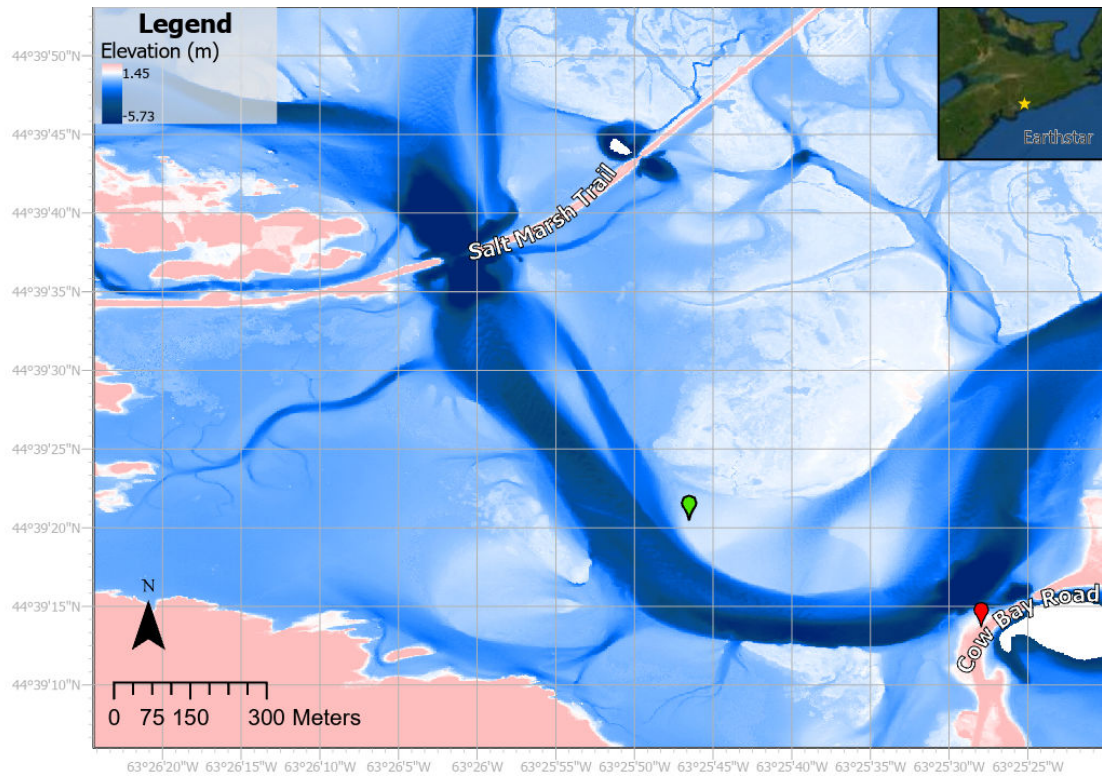


Figure 3.2: A LiDAR-derived digital elevation model of study site is shown (*Halifax Regional Municipality, 2020*). A red marker indicates Deployment Site 1, the closest road access to the study site. A green marker indicates Deployment Site 2, where the base station for the hovercraft was set up. These two deployment sites lie between Cow Bay Road to the southeast and the Salt Marsh Trail to the north. A yellow star indicates on the satellite imagery where Cole Harbour is located along the coast of Nova Scotia.

### 3.3.2 Data Collection

Five field surveys were completed between July-October 2020, and one in July 2021 (Table 3.1). Equipment was unloaded from a rocky beach off Cow Bay road (Figure 3.2, Deployment Site 1). As the tidal flats are mostly intertidal and much of the ground is completely submerged at high tide, data collection took place between ebb and flood tides.

A small craft was used to transport the base station equipment from this area across the deeper channel to Deployment Site 2. The base station, consisting of the RTK GPS base antenna, radio telemetry antenna, computer, and tent for cover, was set up on the tidal flats (see Chapter 2 for specification details). Antennae were secured to a tripod using plastic cable ties and rubber bands to increase the maximum telemetry range between the base station and the hovercraft.

Date	Times	Tidal Phase	Analyzed Transects
29 July 2020	10:30 - 11:30	Low Tide	2
18 August 2020	15:00 - 15:30	Low/Flood Tide	2
01 September 2020	13:30 - 14:30	Low/ Ebb Tide	2
25 September 2020	12:00 - 13:00	Low/Flood Tide	4
15 October 2020	12:50-1:30	Low/Ebb Tide	2
29 July 2021	8:30-9:30	Low/Flood Tide	3

Table 3.1: For each survey, the date and approximate time of the hovercraft survey, and tide phase during the hovercraft flight were recorded. The number of transects from each survey that is analyzed for this study is also stated.

The RTK GPS was set to a spatial resolution of 0.5 meters and allowed to localize while the hovercraft was prepped for flight and ground truth data were collected. Typically, a resolution of 0.5 meters was reached in approximately 45 minutes. During this time, the hovercraft could not be moved, thus the ground truth data were collected while the RTK GPS was localizing.

### 3.3.2.1 Ground Truth Data Collection

Ground truth was performed using photography or video and a 1 m<sup>2</sup> quadrat. The quadrat was built using 3/4 inch PVC pipe and separated into 25 squares by looping waxed twine through the PVC every 10 cm for easier quantification of vegetation cover on the seafloor. Because each survey discussed in this chapter occurred at a different tidal phase, the water depth differed from survey to survey. In order to collect data during a higher tide, a PVC stand was constructed with a GoPro camera mounted approximately one meter above the quadrat so that the whole quadrat would be visible underwater. A hand-held

GPS was used to mark each position where the quadrat was dropped. The quadrat was first dropped at the southeast extent of the seagrass and was allowed to sink to the bottom and settle for a few seconds so the water was as calm as possible. Following the length extent of the seagrass, the quadrat was then dropped every 10-20 meters between these two positions. These methods were used during surveys carried out on 18 August, 01 September, and 15 October 2020. At low tide a similar procedure was followed, however, the stand on top of the quadrat was removed and pictures were taken above water by the researcher. Each drop, regardless of whether the quadrat was deep underwater or not, was thrown out towards the eelgrass bed, but allowed to settle wherever it landed, rather than placed specifically on vegetation. These methods were used for surveys carried out on 29 July and 25 September 2020, and 29 July 2021. In this chapter, ground truth data collected on 29 July 2020, 01 September 2020, and 29 July 2021 are discussed in detail to validate submerged vegetation detected in the sonar data (Figure 3.3). Ground truth data points from 29 July 2020, 18 August 2020, September 25, 2020, and October 15, 2020, were all collected in the shallow water close to the shore of the tidal flat. There was variability in total % cover between consecutive surveys, exemplifying the patchy nature of the eelgrass bed. Ground truth data from July and September 1, 2020, and July 2021 are presented in detail in this chapter.

### **3.3.2.2 Hovercraft Data Collection**

Sonar data were collected in this region over six surveys, spanning from July 2020 to July 2021. The exact dates and tidal phases are recorded in Table 3.1. During each field test performed in 2020 and 2021, the hovercraft was operated manually to ensure that transect lines were as straight as possible. For each of these field tests, the hovercraft was flown from the southeast end of the eelgrass bed towards the northwest end and back to attempt to cover the full length of vegetation. While cross-shore transects were attempted during some of these surveys, the hovercraft path is straightest if flown directly with or against the current, and therefore transects parallel to the tidal flat were those analyzed in

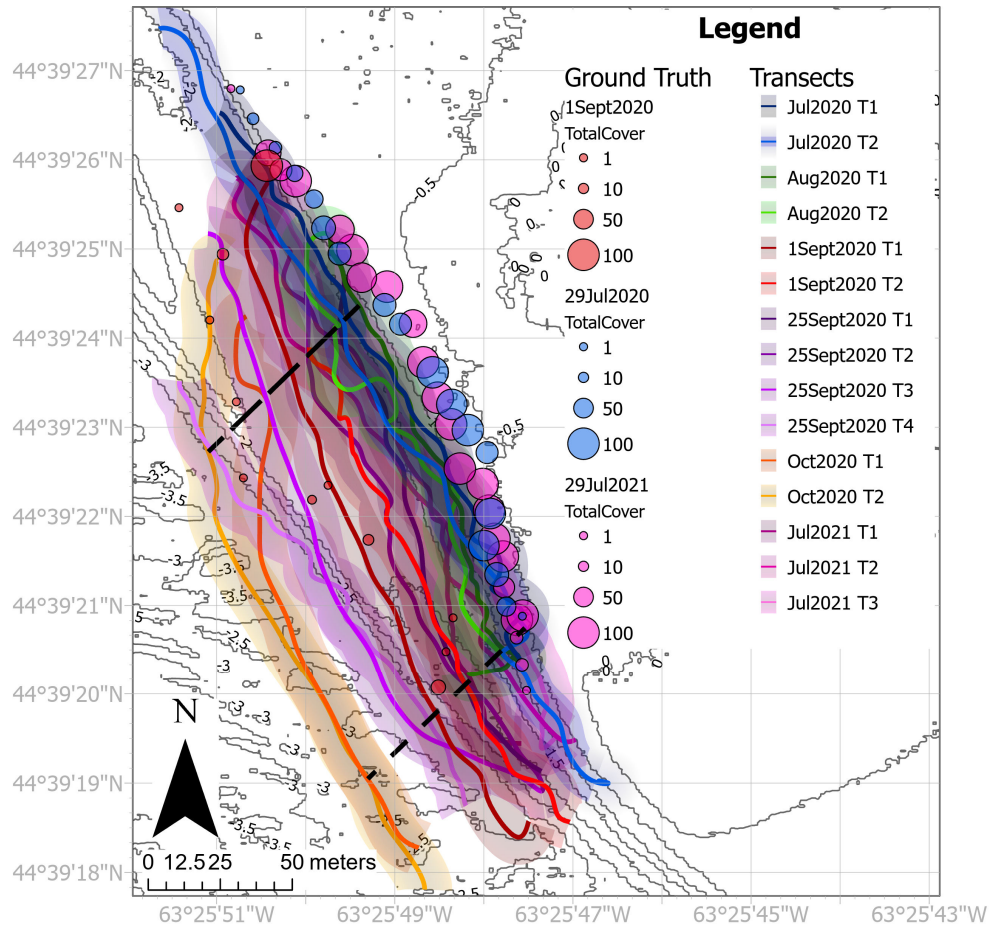


Figure 3.3: A map of the study site showing the spatial distribution of all transects and ground truth surveys analyzed in this chapter. Shaded regions on either side of the transect lines indicate the approximate swath width of the side-scan sonar (across-track direction) and the sizes of the ground truth markers indicate the percentage of total cover of vegetation within quadrats. Black lines indicating depth contours are shown at 0.5 m intervals. The dashed black lines are placed such that all transects fall between them and are used to compare data from overlapping transects.

this study. The number of these along-shore transects varied from survey to survey, but typically four transects were completed.

For each field test, the single beam echo sounder range was set to 5 m, with a pulse length of 100  $\mu$ s, corresponding to a 1 cm resolution in the vertical range. Side-scan sonar horizontal range was set to 10 m for each survey (see Chapter 2 for detailed instrument specifications). Before the hovercraft was flown, data collection was started for both the sonar instruments as well as the IMU instrument on the sonar arm. The spatial resolution of side-scan imagery is dependent on the sample rate (i.e. ping interval), speed of the hovercraft, position along the horizontal range, the horizontal beam width, and the height of the sonar above the seafloor. The ping interval for the side-scan sonar at this range was 53 ms. Based on the ping rate and average speed of the hovercraft during these surveys (approximately 1 m/s), the maximum spatial resolution of each pixel in the side-scan sonar imagery is approximately  $5.3 \times 10^{-4}$  m<sup>2</sup>, with a resolution of 0.01 m across-track and 0.053 m along-track. Since these data are collected in very shallow water (<5 m), the footprint size of the single beam echo sounder is very small. The single beam echo sounder has a conical beam width of 10°. At a distance of 0.3 m between the transducer and the seafloor (approximately the minimum distance at which depth can be calculated), this yields a footprint size of 0.0022 m<sup>2</sup>. At a distance of 3 m from the seafloor (typically above the maximum distance in the survey area), this footprint size goes up by two orders of magnitude (0.216 m<sup>2</sup>) and is still a higher resolution than any available LiDAR or satellite imagery data available in this region (ranging between 1-25 m<sup>2</sup>).

For this study, transects from each survey were selected for detailed analyses based on how straight the hovercraft path was. Between 2 and 4 transects from each survey were chosen. Many of these surveys occurred during different tide phases, thus the backscatter data for both SBES and SSS instruments can be examined when the sonar is at different altitudes from the seafloor. All hovercraft transects analyzed in this chapter are shown in Figure 3.3. The shaded regions on either side of each transect indicate the approximate

side-scan sonar swath coverage.

### 3.3.3 Acoustic Theory: Near-field and Far-field

The sound pressure field emitted by an acoustic source is split into two regions: near-field and far-field. The near-field region is relatively close to the source and the sound field pattern in this region is complicated, whereas in the far-field, the pattern becomes regular and can be approximated as a plane wave (*Jackson and Richardson, 2006*). For high-frequency acoustic instruments, typically measurements are always taken in the far-field region to avoid the effects of the near-field pattern: oscillating sound pressure which varies due to range until the far-field region is reached (*Medwin et al., 1999*). However, when surveying in very shallow water (<1 m height above the seafloor), it is possible that seafloor measurements or features such as vegetation canopy will be collected within the near-field region. In this study, single beam and side-scan sonar instruments are used in very shallow water environments and therefore run the risk of containing measurements within the near-field region. In this section, the near-field distances for both circular and rectangular transducers are explored.

#### 3.3.3.1 Circular Transducer

In the case of a circular transducer, the near-field range calculation is simplified by the symmetry about the axis. The near-field far-field transition range,  $z$ , depends on the shape of the acoustic field (*Zemanek, 1971; Jackson and Richardson, 2006*). This range is approximated using

$$z = a^2/\lambda, \quad (3.1)$$

where  $a$  is the area of the transducer surface ( $a = \pi r^2$ ), and  $\lambda$  is the wavelength of the transducer, calculated by  $c/f$  where  $c$  is the sound speed in water and  $f$  is the sonar frequency. The near-field range can be calculated for the single beam echo sounder

equipped on the SWASH system using Equation 3.1 and a transducer radius of 7.5 mm. This near-field transition range was calculated to be 0.07 m at the maximum point of the beam pattern, and 0.02 m at the smaller side-lobe regions of the beam pattern.

### 3.3.3.2 Rectangular Transducer

The axial symmetry which exists in the circular transducer cannot be exploited for a rectangular transducer. The beams emitted from these transducers have two different dimensions, and thus must both be calculated to determine the size of the near-field (*Ocheltree and Frizzel, 1989*). In the case of the side-scan transducer in this study, the two dimensions in question are the active length of the sonar transducer (i.e. parallel to the hovercraft track) and the height of the transducer. *Ocheltree and Frizzel (1989)* gives the equation for the two dimensions of the near-field range using

$$z = s^2/4\lambda, \quad (3.2)$$

where  $s$  is the length of the transducer side in question. The side-scan transducer equipped on the hovercraft has dimensions of 19 cm in length and 1 cm in height. Using Equation 3.2, the length of the near-field is 4.8 m and the height of the near-field is 0.013 m.

### 3.3.4 Data Processing

All data collected from the hovercraft's sonar arm (including side-scan backscatter, echo sounder backscatter, and XSens IMU time series) were synchronized to the GPS clock using the methods in Section 2.4.3. All sonar data (including single beam and side-scan backscatter) were separated first into individual hovercraft transects for pre-processing and noise removal, and then transects were grouped into deeper or shallower regions based on the minimum depth in which the data were collected. In shallow water transects (sonar height above bottom <1 m), a high proportion of the backscatter data were collected in regions where the eelgrass canopy height was equal to water depth, and therefore there

was a high likelihood that vegetation was either very close to or actually in contact with the sonar transducers. While this does mean that in these instances acoustic data were collected in the near-field, another consideration was the appearance of these near-field returns in backscatter data. When vegetation was in contact with or very close to the sonar transducers, the acoustic returns from these features would overpower the return backscatter signal, creating a region of low backscatter returns from the range beyond this vegetation. As this phenomenon was found in the SSS imagery at nadir (the region directly below the sonar transducers), this phenomenon was termed masking at nadir. Thus, data collected with strong backscatter returns <45 cm from the transducer were sorted into the shallow group, while data without strong backscatter returns <45 cm from the transducer were sorted into the deep group. This threshold was chosen based on the interaction between vegetation and SBES and SSS transducers. All transects from July 2020, August 2020, and two transects (1 and 3) from July 2021 were sorted into the shallow group, while all transects from 01 September 2020, 25 September 2020, October 2020, and transect 2 from July 2021 were sorted into the deep group.

Although some of these data were collected in the near-field of the transducers, it was noted that side-scan data did not exhibit banding associated with the near-field range amplitude variability in the near-nadir region, therefore these data were still used for backscatter data analysis. Although SBES returns from heights above the seafloor less than 20 cm were not used, some SBES backscatter data contained vegetation returns in the near-field and were still included in the clustering algorithm in the hopes that a strong backscatter return would be apparent regardless of variability in the near-field collected amplitudes.

#### **3.3.4.1 Side-scan Processing**

The side-scan data were transformed from a manufacturer-created file type (.872) to a type accepted by sonar processing software (.xtf). SonarWiz 7.3 software by Chesapeake Tech, Inc. was used to process the side-scan data. The seafloor was first tracked using a

backscatter threshold detection algorithm, and any mistakes in nadir distance (range from nadir to seafloor) made by the software were corrected manually. Using this software, the data were then corrected for slant range, and time-varying gain, and filters were applied to decrease the difference in backscatter between the near-field and far-field returns. Navigation data from the Here+ GPS were also integrated into the side-scan sonar files. Corrected side-scan sonar images were plotted in waterfall form for qualitative visual analysis. A number of features are visible in the sonar imagery, though features tend to look different based on how far they occur from nadir due to the masking phenomenon.

#### **3.3.4.2 Single Beam Processing**

In regions where features on the seafloor (such as vegetation) are located at or close to nadir of the side-scan sonar data, single beam echo sounder data can be used to support the evidence of seafloor features. In the raw single-beam data (Figure 3.4), a region of low backscatter returns are followed by a region of higher backscatter returns near the transducer. The region of low backscatter returns is the blanking distance (approximately 0 m- 0.2 m), a region where the transducer ignores most incoming backscatter so that the emitted sonar pulse does not interfere with received data. The region of higher backscatter data which follows is likely the continued ping emitted by the sonar which the blanking distance could not entirely account for. The high backscatter returns after the blanking distance were removed by first isolating backscatter data in this region (0.28-0.45 m) using a feature isolation tool in the image processing MATLAB toolbox. These backscatter returns were likely due to the transducer still emitting from transmit. This data was then modeled using a single beam profile from when the echo sounder was not in the water, and this profile was subtracted from all data. The isolated returns were then added back into the affected area. Although these methods preserved strong backscatter returns, some weaker returns, or some leading edges of returns are not preserved perfectly. Figure 3.5a,b shows an example of an echogram of a vegetated seabed in shallow water after this noise removal. In this figure, returns closest to the transducer with high backscatter amplitudes

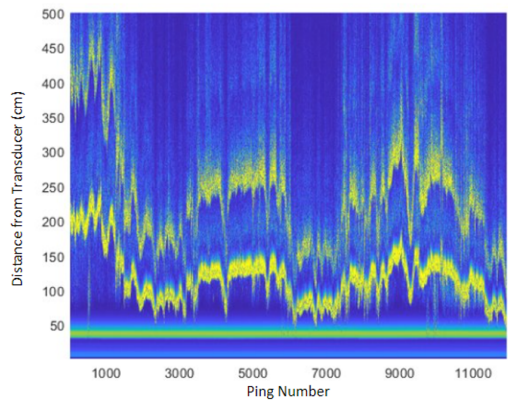


Figure 3.4: Segment of Raw ES data before removal of continuous high backscatter returns.

occur at distances of approximately  $>25$  cm.

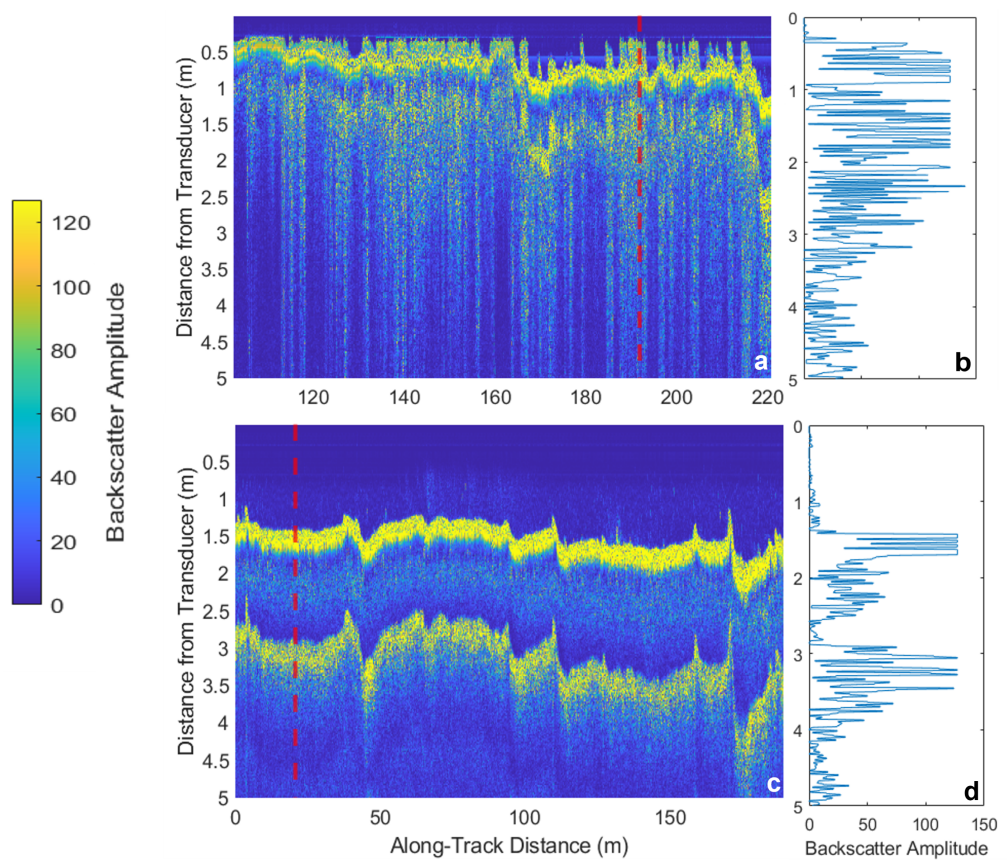


Figure 3.5: Single beam echo sounder echograms and individual backscatter profiles for (a,b) shallow water and (c,d) deeper water. A red, dashed line indicates the location in the along-track direction of the backscatter profiles presented in c and d.

Single beam echograms were compiled for each transect analyzed in this study. In

regions of very shallow water (<0.5 m), backscatter returns from the seafloor and features above the seafloor may interact with the constant noise. This decreases the signal-to-noise ratio (SNR) in the regions surrounding these strong backscatter returns and can make processing sonar data difficult (*Quester Tangent Corp.*, 2004).

### **3.3.4.3 Side-Scan Image Segmentation**

Segmentation of the side-scan data was performed on a feature matrix created through the calculation of statistics on rectangular patches of SSS backscatter. This method is similar to that used by software such as QTC Impact, QTC Multiview (*Quester Tangent Corp.*, 2004), BioSonics Visual Bottom Typer (VBT), and EcoSAV (*Sabol et al.*, 2002). A variety of statistics were chosen to characterize the pixels within rectangular patches on the seafloor based on these existing algorithms and other image-based classification studies (*Quester Tangent Corp.*, 2004; *Sabol et al.*, 2002; *Brown et al.*, 2011; *Foster-Smith et al.*, 2004; *Brown et al.*, 2004; *Collier and Brown*, 2005; *Lucieer*, 2008; *McLarty et al.*, 2020). Statistics were calculated on side-scan backscatter amplitudes at two different spatial resolutions within rectangle patches sized 50-by-20 (along-track by across-track) pixels for the higher resolution and 100-by-50 pixels for the lower resolution. These resolutions are exemplified by Figure 3.6, which shows the standard deviation at both resolutions over Transect 2 collected on 25 September 2020. The rectangle sizes were chosen so that the boundaries between bare sediment and features on the seafloor would stand out, but the overall resolution of the SSS backscatter would not decrease to the point that the smaller features were smoothed out. Assuming an average hovercraft speed of 1 m/s and a height above the seafloor of 1 m, the maximum spatial resolution of these statistics are 0.1 m-by-0.02 m and 0.5 m-by-0.05 m respectively. The spatial resolution of these rectangles varies with range due to beam width. Statistics calculated for each rectangular patch included: mean, standard deviation, skewness, and kurtosis, as well as statistics related to the gray-level co-occurrence matrices (GLCM), which included contrast, correlation, homogeneity, and energy (i.e. the sum of squared elements) between

rectangles (Table 3.2). These statistics were then combined in an  $M \times N$  sized matrix, where  $M$  indicates the number of observations (i.e. number of rectangular patches) and  $N$  is the number of variables, or statistics, calculated.

Statistic	Type
mean	signal
standard deviation	signal
skewness	signal
kurtosis	signal
contrast	GLCM texture
correlation	GLCM texture
homogeneity	GLCM texture
energy	GLCM texture

Table 3.2: Statistics calculated on each rectangle patch for shallow and deep side-scan backscatter transects.

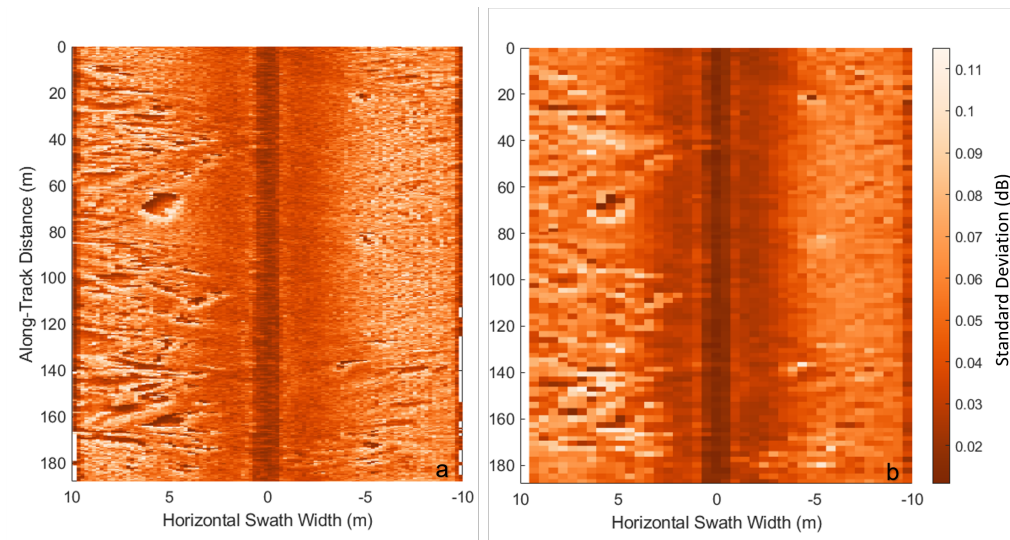


Figure 3.6: Side-scan backscatter standard deviation calculated over (a) high-resolution rectangular patch (50x20 pixels) and (b) low-resolution rectangular patch (100x50 pixels).

This matrix of statistics was used in the clustering algorithm, K-means, which groups similar observations together based on the squared Euclidean distance from a cluster centroid position. The K-means clustering algorithm groups observations into a set number of clusters. The ideal number of clusters was found to be 7 based on trial and error using a sample transect to determine which cluster number yielded the maximum amount of

clusters with distinct statistics. Initial centroid positions were chosen using the K-means++ algorithm in MATLAB. Clustered pixels were then georeferenced for comparison between transects.

#### **3.3.4.4 Single Beam Profile Segmentation**

After near-transducer noise was removed from the SBES backscatter, the first and second seafloor backscatter returns, where they existed, were isolated for deep and shallow transects. The second seafloor returns are indicated as the first echo after the seafloor return, which is differentiated from backscatter in the water column based on the height of the transducer above the seafloor in adjacent echo sounder profiles and higher mean backscatter amplitude. After the returns were isolated, a moving mean with a window size of 3 profiles was performed to decrease noise. For shallow transects, a matrix of these isolated returns was created by aligning the first maximum peak in the first isolated return in each SBES profile and including the second isolated return in each profile in the matrix behind the first. For deep transects, only the first seafloor return was used, as some regions of the deeper regions do not have two seafloor returns.

Statistics were then calculated on each matrix of seafloor return backscatter amplitudes and included maximum, mean, standard deviation, skewness, and kurtosis. These statistics were chosen due to their use in commercial ground discrimination algorithms such as QTC and Roxann (*Quester Tangent Corp.*, 2004; *Hamilton*, 2001) as well as use in other profile-based ground discrimination studies (*Hamilton*, 2001; *Brown et al.*, 2005; *Barrell and Grant*, 2013; *Barrell et al.*, 2015; *Sabol et al.*, 2002). For shallow transects, maximum peak width, mean peak prominence, the integral of return, and the total number of peaks were calculated for the first and second returns separately and then averaged. For deep transects, these statistics were only calculated on the first return since the deepest regions did not have a second return within 5 meters from the transducer. The statistics were re-scaled such that the range for each variable was between 0 and 1. The K-means clustering algorithm was used to segment the echo sounder data based on these calculated statistics.

Initial centroid positions were chosen using the K-means++ algorithm in MATLAB. Shallow water transects were segmented into 4 clusters, while deeper water transects were segmented into 2 clusters based on trial and error to determine which cluster number yielded the maximum amount of clusters with distinct statistics for each group.

#### **3.3.4.5 Ground Truth**

The GPS waypoints logged with the hand-held GPS and photos or videos were first collected and time-stamped using notes taken in the field and meta-data from the electronics. The total percent vegetation per square meter was logged for each photo taken. Each of the 25 squares laid out by twine for each quadrat was worth 4% of the total meter. The total percent cover per  $m^2$  was calculated by adding up all squares with vegetation.

### **3.4 Results**

A total of 15 transects from 6 surveys were analyzed for this study. All transects analyzed are shown in Figure 3.3 as well as ground truth data from July and September 2020 and July 2021. The data were collected in different tidal phases and along different isobaths, from close to the tidal shore at the 0 m isobath to nearing the center of the deep channel at the 3.5m isobath. Six of these transects were sorted into a shallow water group due to vegetation interaction with the sonar transducers, while nine transects were sorted into the deeper group. Figure 3.5 presents examples of single beam echograms in shallower and deeper water with individual profile examples from a vegetated (Figure 3.5b) and non-vegetated (Figure 3.5d) seabed. Both SBES profiles exhibit clipping (i.e. backscatter reaches the maximum possible values for the instrument). Both profiles contain many individual peaks, though the first seafloor return from the non-vegetated seabed profile is narrower and less variable than that of the vegetated seafloor.

In this section, backscatter imagery and classification results from shallow water transects and deep water transects are analyzed, and overlapping transects from both depth categories are compared to each other. The effects of hovercraft motion (i.e. instability

and variability in hovercraft heading and lateral drift) on the side-scan data imagery are also shown.

### **3.4.1 Shallow Water: Seagrass-Transducer Interactions**

#### **3.4.1.1 Sonar Imagery and Ground Truth**

Figure 3.7 shows an example of masking at nadir from Transect 1 on July 29, 2020. This transect exhibits similar patterns in both the single beam and side-scan imagery to all other shallow water transects, as masking at nadir was observed in all shallow water transects. This transect, shown in Figure 3.7, was collected very close to the shore of the tidal flat around 0-1.5 m isobaths. In the side-scan imagery (Figure 3.7b), high backscatter amplitudes were recorded at nadir. Between 150 and 50 meters along-track distance, backscatter maxima at nadir decrease to minima within  $\pm 0.5 - \pm 1.5$  m horizontal width.

In the single beam echogram (Figure 3.7c), high backscatter amplitudes are found at close range to the transducer and are cut off abruptly at approximately 0.3 m due to the methods of near-transducer noise removal. At these shallow depths, there is a lot of ping-to-ping variation in returns. These first returns tend to have narrow regions with backscatter maxima and are variable in total width and mean backscatter. As depth begins to increase, at approximately 0-40 m in along-track distance, these near-transducer returns widen to encompass backscatter from the seafloor and features above it.

Three ground truth photographs along this transect are shown in Figure 3.7d-f. The ground truth data collected in July 2020 shows that the total percent cover varied between each data point, indicating the patchy nature of this eelgrass bed. This is exemplified by the example photographs, which show a total percent cover of 48% near the southeastern end of the transect, 100% around the middle, and 68% closer to the northwest end of the transect. Based on the example images and ground truth points shown in Figure 3.7a, total % cover tended to be greater in the very shallow region in the middle section of the study area.

Due to the masking at nadir in the side-scan imagery, along the majority of the transect,

the information that can be interpreted is only at nadir and not along the swath width, effectively creating a region of acoustic shadow caused by dense eelgrass under the transducer. Therefore, the ground truth images collected at other points across the horizontal sonar swath cannot be directly used to validate identified vegetation but the consistent masking suggests continuous eelgrass for points e and f. Some amount of bare sediment is visible in each ground truth image, which indicates that the region shown in this transect exhibits both thick, continuous eelgrass and regions that are thick but patchy. Figure 3.7d occurs in a very shallow region of the transect. While it is unclear if the single beam or side-scan backscatter in this region indicates submerged vegetation features, the ground truth image shows patchy, sparse eelgrass.

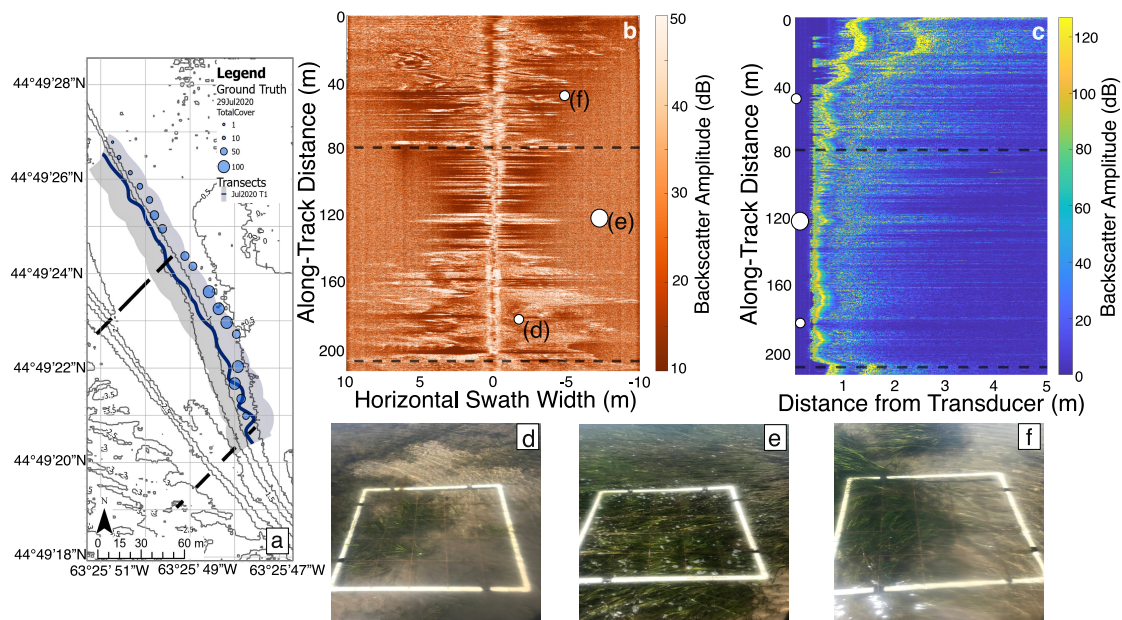


Figure 3.7: An example of masking at nadir is shown via Transect 1 from the hovercraft survey on July 29, 2020. The (a) hovercraft transect and ground truth values, (b) side-scan imagery, (c) single beam echogram, and (d-f) select ground truth photos are shown. Sonar images (a,b) are oriented such that the origin indicates the southernmost point on the transect. White dots on the sonar images (b,c) show the along-track and horizontal positions of the ground truth photos (d-f), and their sizes indicate the total percent cover of 48%, 100%, 68%. Black dashed lines indicate northern and southern extents limits between which all transects exist and are used to georeference between overlapping transects and ground truth points (d-f).

### 3.4.1.2 Side-Scan Segmentation

The side-scan segmentation results for Transect 1 on 29 July 2020 are shown in Figure 3.8. Table 3.3 indicates the feature classification of each cluster. Cluster 1 indicates highlights (i.e. regions where backscatter, standard deviation, GLCM energy and heterogeneity are higher), while cluster 6 indicates shadows (i.e. regions where backscatter, standard deviation, GLCM energy and heterogeneity are lower). Combined, these two clusters create regions of highlights and shadows that indicate features on the seafloor. In this transect, most of these features occur near nadir due to the proximity of vegetation to the sonar transducers. Between approximately 170-50 m in along-track distance, these combined clusters form an irregular semi-circle shape that curves to where the masking at nadir is continuous. As depth increases at along-track distances lower than 50 m in the along-track direction, some features are still found at nadir, and others occur further across the horizontal range. Side-scan segmentation for all shallow water transects was successful in identifying features both at nadir and along the swath width in the across-track direction in regions where there was no masking. In regions with masking on both sides of SSS imagery, however, these clusters only contain information that can be applied to nadir and not at other ranges in the across-track direction.

Cluster Number	Classification
1	Eelgrass boundary (i.e. backscatter maxima)
2	Bare sediment
3	Bare sediment
4	Bare sediment
5	Acoustic Shadow (i.e. backscatter minima)
6	Acoustic Shadow (i.e. backscatter minima)
7	Nadir, water column backscatter

Table 3.3: Cluster number and classification of feature type for shallow water clusters. Regions that have cluster 5 and 6 bordered by cluster 1 are classified as eelgrass. Cluster 7 only exists at nadir and was omitted from the figures presented in this study.

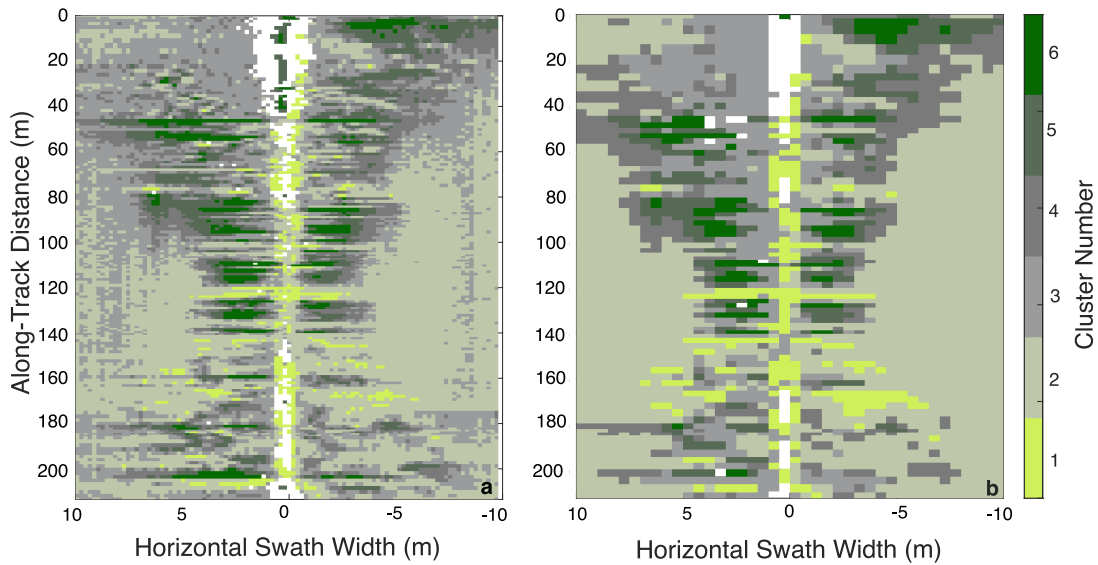
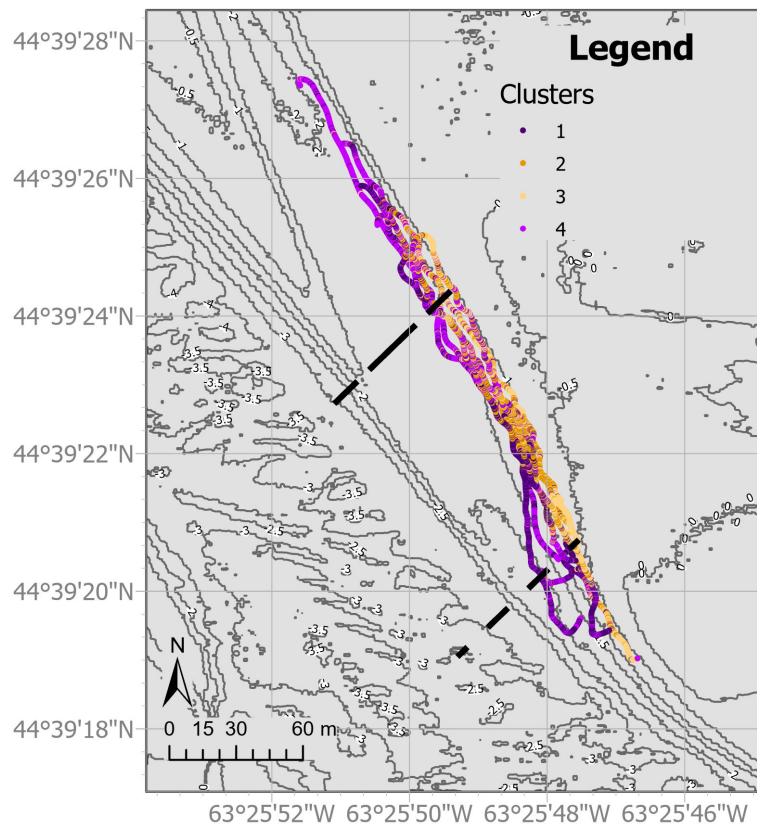


Figure 3.8: Side-scan segmentation at a resolution of (a) 50x20 pixels and (b) 100x50 pixels for Scenario A: Transect 1, 29 July 2020. Cluster numbers and their classification assignments are shown in Table 3.3. Cluster 1 indicates backscatter maxima from eelgrass, clusters 2-4 indicate bare sediment and clusters 5-6 indicate regions of acoustic shadows. Cluster 7 only exists at nadir and was omitted from these figures.

### 3.4.1.3 Single Beam Classification

The single beam classification results for all transects considered to be in shallow water are shown in Figure 3.9. Profiles sorted into each cluster are shown in Figure 3.10. Clusters 1 and 4 occur in every transect (Figure 3.10a,d) but are most concentrated in regions not associated with transducer-vegetation interaction, while clusters 2 and 3 (Figure 3.10b,c) occur in regions where vegetation was more likely to brush against the transducers. Cluster 1 includes SBES profiles with lower water column backscatter returns and higher seafloor return backscatter amplitudes (Figure 3.10a), cluster 2 includes profiles that have interaction between the transducer and vegetation and a concentrated seafloor return (Figure 3.10b), cluster 3 shows profiles that have seafloor returns which are more dispersed and interactions between the transducer and vegetation, and finally cluster 4 includes profiles with larger seafloor and water column backscatter amplitudes. These clusters defined by the automatic classification of echo sounder profiles are not related to

the absence or presence of submerged vegetation in the water column and cannot be used to map the eelgrass in this region.



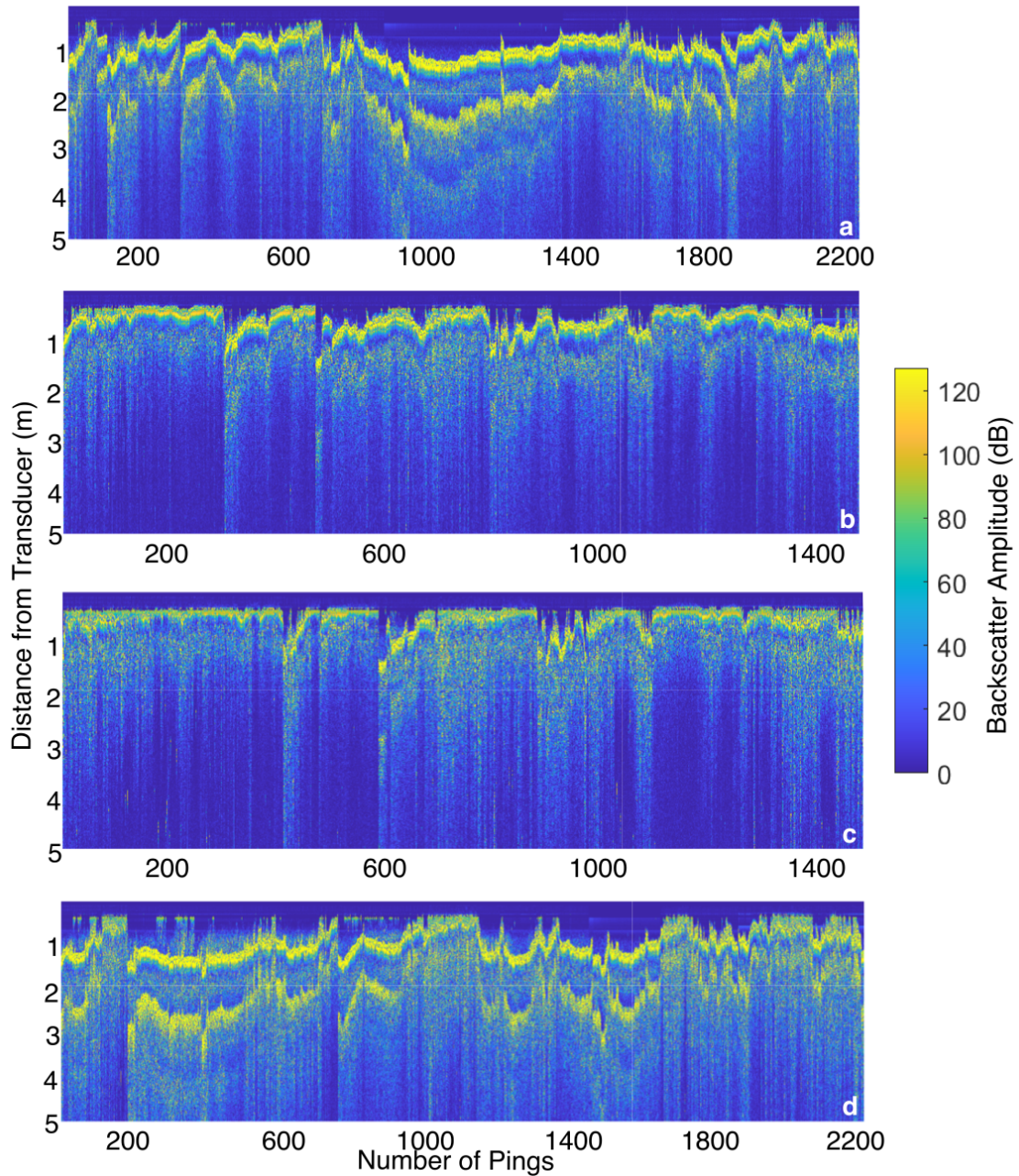


Figure 3.10: All backscatter profiles assigned to clusters (a-d) 1-4, as designated by the k-means clustering algorithm used on shallow SBES data, are stacked beside each other. Backscatter profiles are not necessarily consecutive in time or distance.

### 3.4.2 Vegetation in Deeper Water

#### 3.4.2.1 Sonar Imagery and Ground Truth

Transect 2 from the survey completed on 25 September 2020 is used as an example for Scenario B, in which vegetation can be identified in deeper water (Figure 3.11). This

transect (shown in Figure 3.11a) covers the region between the tidal flat to the east and sandbar to the west, northwest, and the deeper channel to the west, and occurs around the 1.5-2.5 m isobaths. The side-scan imagery for this transect (Figure 3.11b) shows high backscatter amplitudes followed by regions of acoustic shadow to the left side of the plot (i.e. 10-0 m across-track) and a few of these regions to the right side of this plot. Features that likely indicate submerged vegetation are typically irregular in shape and individual eelgrass features tend to be small in the along-track direction as sparse vegetation is expected at these depths. Other, physical features on the seafloor (i.e. ripples or depressions on bottom) can be differentiated from submerged vegetation visually based on the pattern of high backscatter and low backscatter when compared to seagrass features. For example, a larger feature found between 80-60 m along the track and around 7-5 m in the across-track direction can seem like submerged vegetation at first due to the irregular shape, however this is more likely to be a depression on the seafloor based on the position of acoustic shadow which would appear first in the along-track direction as the hovercraft moved, with very little higher backscatter returns before the acoustic shadow. While higher acoustic backscatter returns have been enhanced due to corrections made in SonarWiz, this feature can be in the raw SSS data (Figure 3.12. In this data, the lack of slant or beam angle correction enhances the differences between the large feature discussed and seagrass features (smaller, irregular features found throughout the left side of this transect.

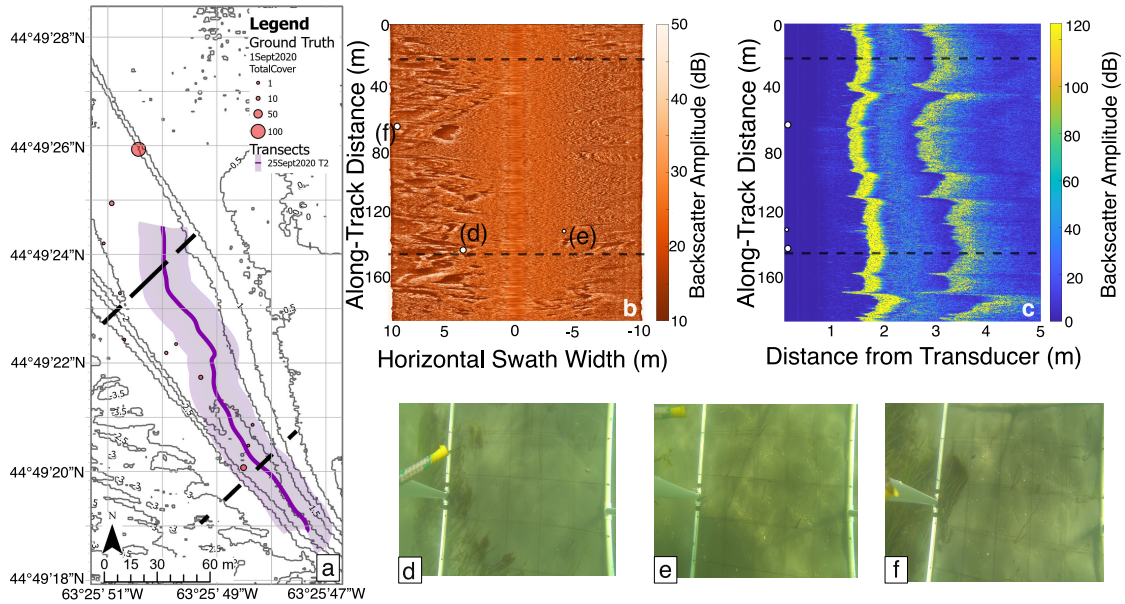


Figure 3.11: An example of a transect with submerged vegetation in deeper water is shown via Transect 2 from the hovercraft survey on September 25, 2020. The (a) hovercraft transect and ground truth values, (b) side-scan imagery, (c) single beam echogram, and (d-f) select ground truth images are shown. Sonar images (a,b) are oriented such that the origin indicates the southernmost point on the transect. White dots on the sonar images (b,c) show the along-track and horizontal positions of the ground truth photos (d-f), and their sizes indicate the total percent cover of 28%, 0%, and 12%. Black dashed lines indicate northern and southern extents limits between which all transects exist and are used to georeference between overlapping transects and ground truth points (d-f).

The SBES echogram (Figure 3.11c) shows a strong seafloor return between approximately 1 and 2.5 meters from the transducer with few returns from the water column. This transect does not show continuous or patchy vegetation, though the region between 140-100 m in the along-track direction may contain sparse vegetation based on weak returns close to the seafloor.

Three ground truth images from 01 September 2020 are shown in Figure 3.11d-f. The ground truth data points for this survey were not collected in a straight line, and patterns that exist in the ground truth close to the shore of the tidal flat are not seen in these data. The northernmost ground truth point is also closest to the tidal flat and has the highest percent cover (100%). The ground truth, shown in Figure 3.11d-f, shows 28%, 0%, and

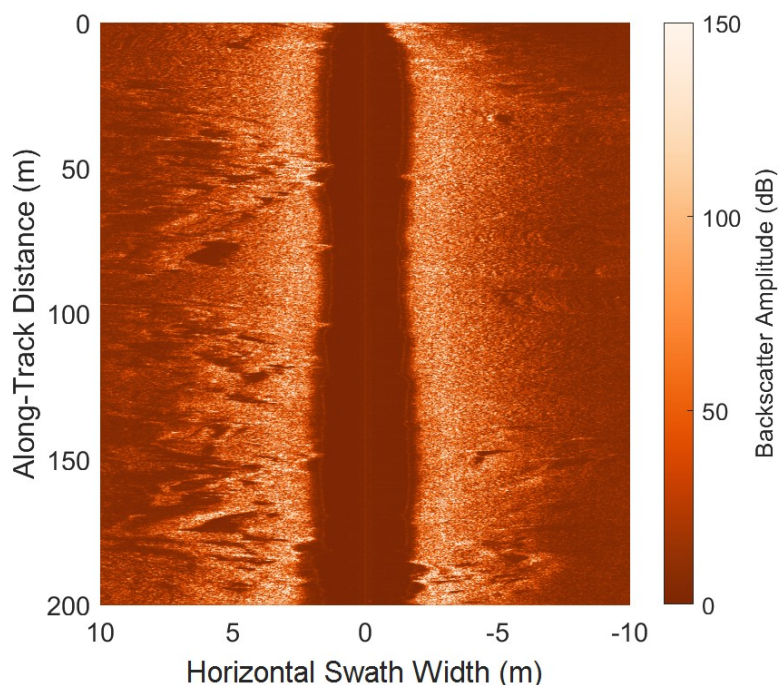


Figure 3.12: Raw side-scan backscatter data for Track 2 on 25 September 2020.

12% cover respectively. Based on the location of these ground truth points on the swath of this transect, points d and f are close to regions identified in the side-scan backscatter data as features or vegetation. Both ground truth images for points d and f show patchy, sparse eelgrass within the quadrat. In the side-scan imagery, point e is close to an area with a shadow and highlighted region which could be a feature on the seafloor, though it cannot be validated as submerged vegetation as the ground truth imagery shows bare sediment within the quadrat.

### 3.4.2.2 Side-Scan Segmentation

The side-scan segmentation results for Transect 2 on 25 September 2020 are shown in Figure 3.13. Table 3.4 shows the feature classification of each cluster. Cluster 1 indicates highlights like in Section 3.4.1.2 , while cluster 5 indicates shadows. Combined, these two clusters create regions of highlights and shadows that indicate features on the seafloor. A few features with combined highlights and shadows exist in the 50x20 rectangular patch segmentation results in Figure 3.13a, while the 100x50 rectangular patch clusters in

Figure 3.13b show only two areas where highlights and shadows are combined. On the left side of the segmentation results (10-0 m across track), combined features are found consistently along-track in the higher spatial resolution (Figure 3.13a) and many of these features are still preserved at lower resolutions (Figure 3.13).

Cluster Number	Classification
1	Highlights (i.e. backscatter maxima)
2	Bare sediment
3	Bare sediment
4	Bare sediment
5	Acoustic Shadow (i.e. backscatter minima)
6	Near-nadir, bare sediment
7	Nadir, water column backscatter

Table 3.4: Cluster number and classification of feature type for shallow water clusters. Regions which have cluster 5 bordered by cluster 1 are classified as eelgrass. Clusters 6 and 7 only exist at and near nadir and were omitted from the figures presented in this study.

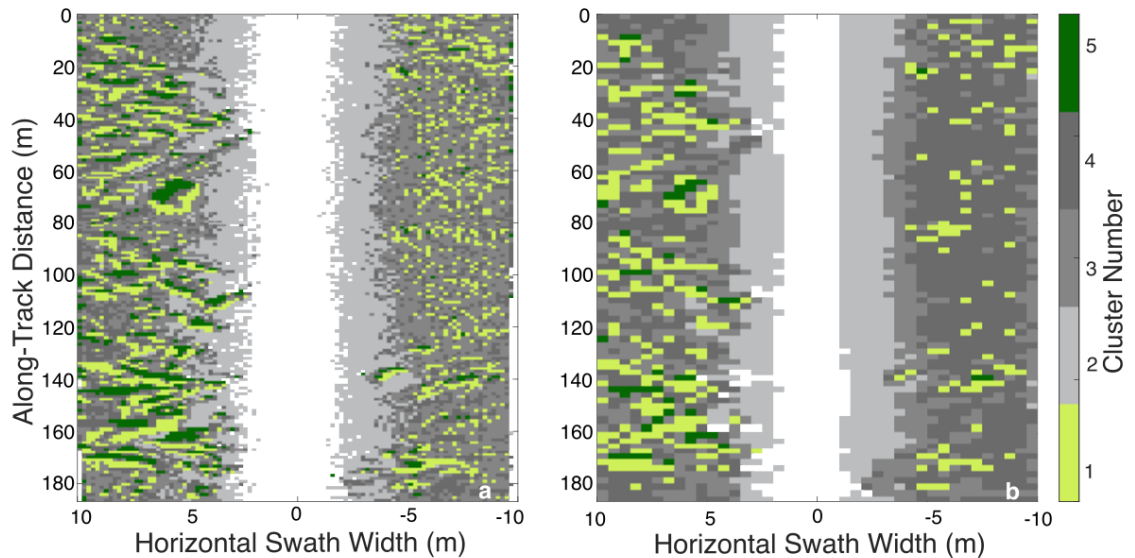


Figure 3.13: Side-scan segmentation at analysis resolutions of (a) 50x20 pixels and (b) 100x50 pixels for a deeper water transect: Transect 2, 25 September 2020. Cluster numbers and associated classification assignments are shown in Table 3.4. Cluster 1 indicates highlights, clusters 2-4 indicate bare sediment and cluster 5 indicates shadows. Clusters 6-7 only exist at nadir and were omitted from these figures.

A number of seafloor features are identified through the segmentation of this transect.

Vegetation is identified on the left side of the transect (10-0 m across-track) as groups of irregular, features which are individually small in the along-track direction. Non-vegetation features on the seafloor are also automatically grouped via classification (i.e. the large feature between 80-60 m along the track and around 7-5 m across). Larger features, such as the physical feature mentioned in Section 3.4.2.1, benefit from clustering at higher and lower resolutions, as features such as small bedforms and many of the submerged vegetation features will be averaged out and therefore not indicated as a feature at a resolution of 100x50 pixels.

### **3.4.2.3 Single Beam Classification**

The single beam classification results for all transects considered to be in deeper water are shown in Figure 3.14. Two clusters were identified in these transects: cluster 1 indicates regions without high-backscatter returns in the water column (Figure 3.15a), while cluster 2 indicates areas with high-backscatter returns in the water column (Figure 3.15b). These results did not segment profiles with returns from vegetation into discrete clusters and cannot be used to map the eelgrass in Cole Harbour.

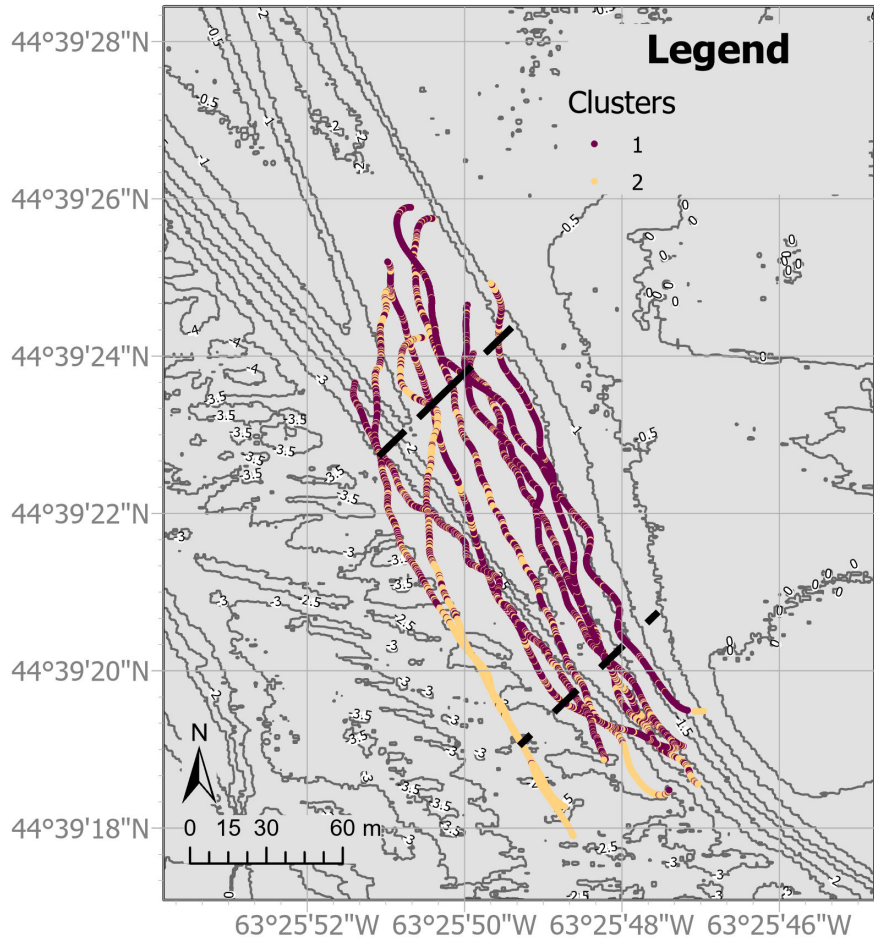


Figure 3.14: Single beam echo sounder segmentation for all deep water transects. Two clusters were identified for these transects. Black dashed lines indicate northern and southern extent limits between which all transects exist and are used to georeference between overlapping transects.

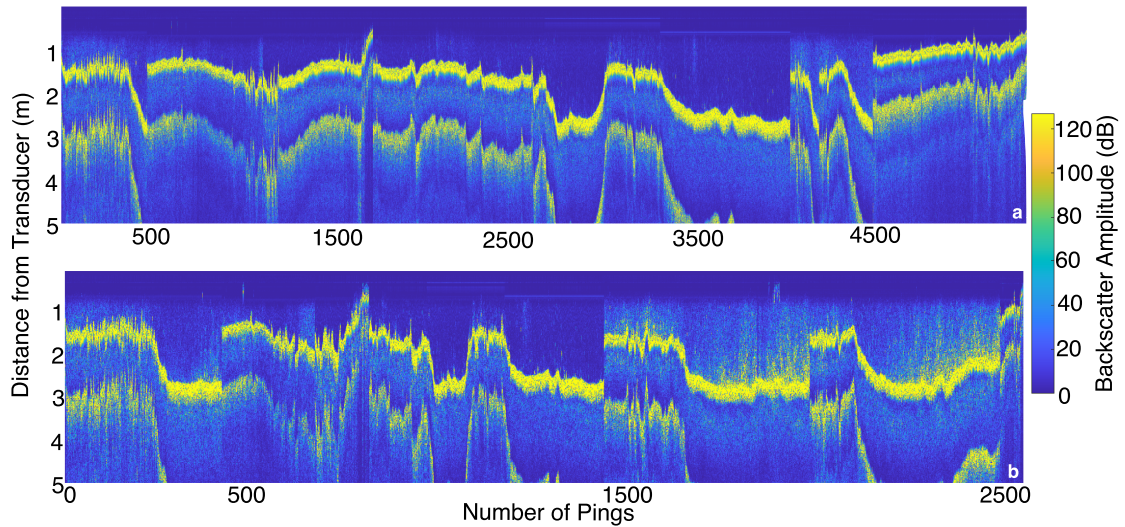


Figure 3.15: Backscatter profiles stacked together for clusters (a) 1 and (b) 2 as designated by the k-means clustering algorithm used on deep SBES data. Backscatter profiles are not necessarily consecutive in time or distance.

### 3.4.3 Effects of Hovercraft Motion

The effects of hovercraft motion on side-scan imagery are exemplified by Transect 2 from August 18, 2020 (Figure 3.16) and Transect 2 from 29 July 2020 (Figure 3.18). The transect from August, shown in Figure 3.16a is found fairly close to the shore of the tidal flat between the isobaths of 0.5-2 m and exhibits a number of curves throughout the along-track distance. There is transducer-vegetation interaction at nadir in the side-scan imagery for this transect (Figure 3.16b) around approximately 130-120 m, 110-100 m, 90-70 m, 40 m, and 30-0 m in the along-track direction. These transducer-vegetation interactions can also be seen in the SBES echogram (Figure 3.16c) as the distance between seafloor or canopy height decreases. The resulting side-scan imagery across the horizontal swath forms lobe-like shapes in which highlighted regions approach the transducer-vegetation interactions at nadir and are cut off sharply. Shadows fill the center of these ‘lobes’. Three ground truth images along the track were chosen to validate vegetation identification (Figure 3.16d-f). These images show 48%, 96%, and 68% total cover respectively. Figure 3.16d shows a ground truth point at the very edge of this transect swath width and shows a region between

discrete eelgrass patches where bare sediment is clearly visible. Point f occurs fairly close to nadir in a region with vegetation-transducer interaction, and while the ground truth image in Figure 3.16f shows patchy regions of eelgrass, the vegetation is thick where it exists. Similarly, while point e occurs close to 5 m from nadir, the ground truth image in Figure 3.16e shows thick, continuous growth in and past the quadrat, though at the lower corner of the quadrat, the growth becomes patchy.

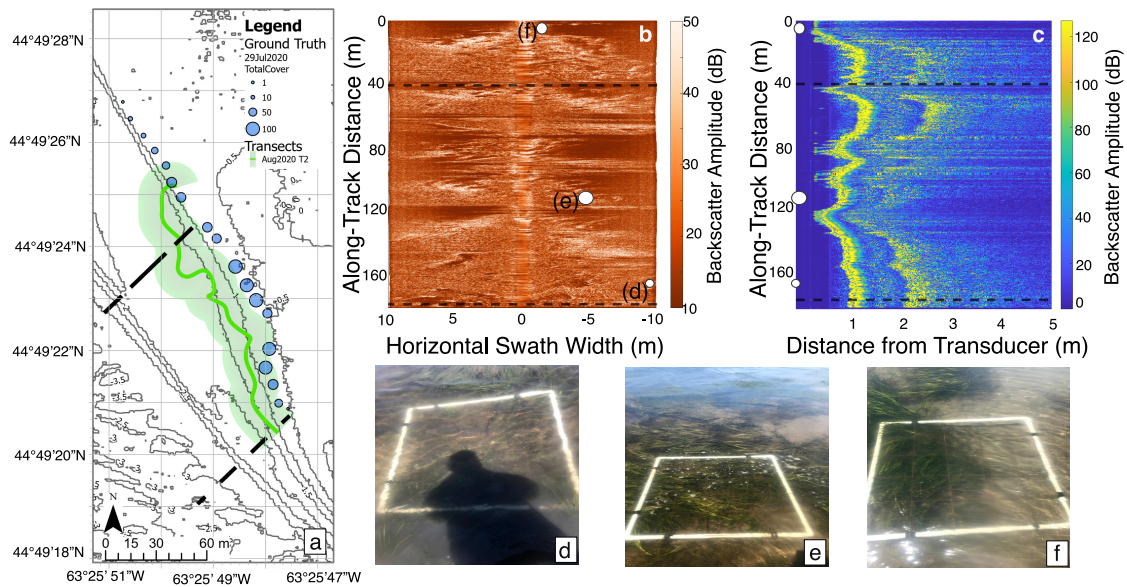


Figure 3.16: An example of hovercraft movement causing effects that can be seen in the sonar backscatter data from data collected on August 18, 2020. The (a) hovercraft transect and ground truth values, (b) side-scan imagery, (c) single beam echogram, and (d-f) select ground truth photos are shown. Sonar images (a,b) are oriented such that the origin indicates the southernmost point on the transect. White dots on the sonar images (b,c) show the along-track and horizontal positions of the ground truth photos (d-f), and their sizes indicate the total percent cover of 48%, 96%, and 68%. Black dashed lines indicate northern and southern extents limits between which all transects exist and are used to georeference between overlapping transects and ground truth points.

The side-scan segmentation results for Transect 2 on 18 August 2020 are shown in Figure 3.17. Clusters 1 and 2 indicate highlights, while cluster 6 indicates shadows. Combined, these two clusters create regions of highlights and shadows that indicate features on the seafloor. With the combination of highlights and shadows, the lobe-like

shapes discussed in Section 3.4.3 are preserved in Figure 3.17 in the 50x20 rectangular patch results and partially preserved in Figure 3.17b for the 100x50 patch results.

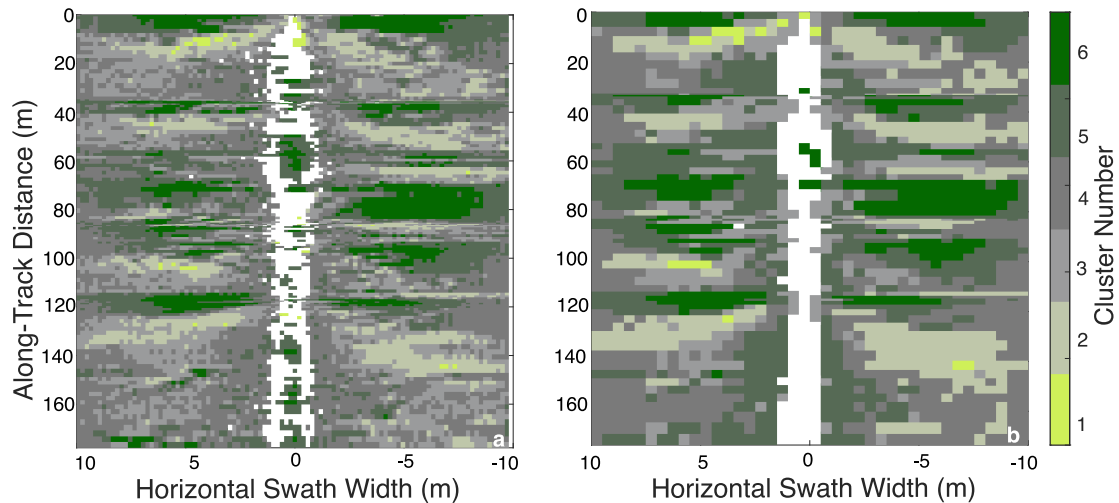


Figure 3.17: Side-scan segmentation at a resolution of (a) 50x20 pixels and (b) 100x50 pixels for a transect exhibiting effects of hovercraft motion: Transect 2, 25 September 2020. Cluster 1 indicates highlights, clusters 2-4 indicate bare sediment, and clusters 5-6 indicate shadows. Cluster 7 only exists at nadir and was omitted from these figures.

Transect 2 from 29 July 2020, shown in Figure 3.18a, is found close to shore between the 0-2 m isobaths. The effects created from the movement of the hovercraft can be seen on the left side of the side-scan imagery from -3 to -10 m between 300-250 m along the track (Figure 3.18b). Visually, this region has scalloped, highlighted edges infilled by shadows. The scalloped shapes are positioned diagonally toward nadir and each shape is repeated closer along the sonar swath towards nadir. The motion artifacts have been fully segmented in the 50x20 clustering results and are automatically classified as vegetation. Another transect that shows artifacts of hovercraft motion included in this survey is Transect 3 from July 2021. The backscatter data and classification for this full transect are shown in Figure B.7.

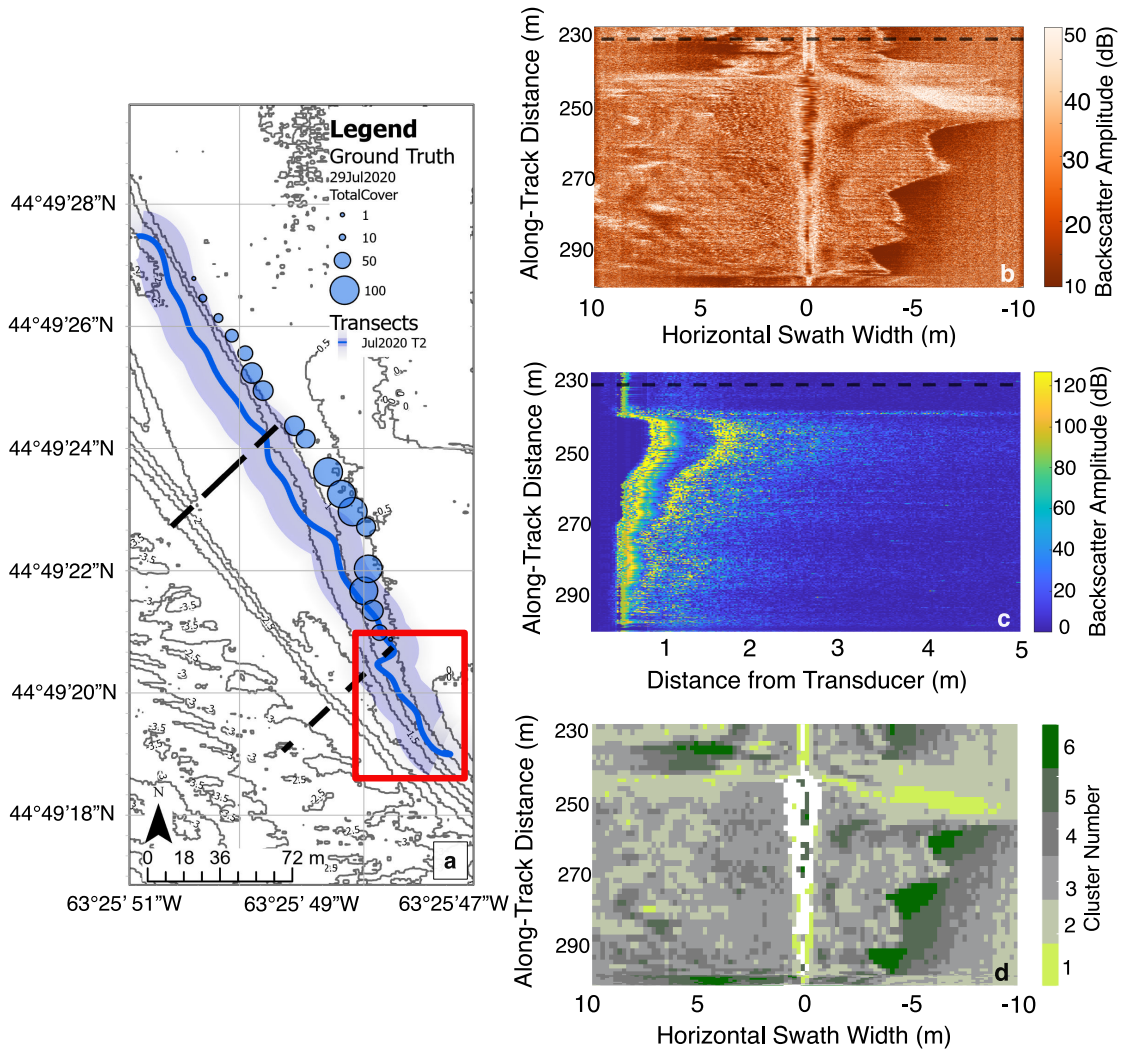


Figure 3.18: An example of hovercraft movement causing effects that can be seen in the sonar backscatter data from data collected on July 29, 2020. A map of the hovercraft transect (a) is shown with a red box indicating the region of interest due to hovercraft motion. This area of interest is shown using (b) side-scan and (c) single beam echogram as well as (d) high-resolution side-scan segmentation.

### 3.4.4 Transect Comparisons

Transects 1 and 3 from surveys in July 2020 and 2021 respectively are compared in Figure 3.19. Much of the swath width from these transects overlaps between the dashed lines indicated in this figure. While the water is slightly deeper in Transect 3 (Figure 3.19d,e) than in Transect 1 (Figure 3.19b,c), there is significant interaction between the sonar transducers and vegetation in both transects. In Transect 3 (Figure 3.19d,e),

this vegetation-transducer interaction is mostly concentrated on the right side of side-scan sonar imagery in Figure 3.19d (i.e. across-track distance 0-10 m). As mentioned in Section 3.4.1.1, the Transect 1 SBES echogram shows the seafloor very close to the transducer and when compared with the side-scan imagery, between approximately 140-80 m in the along-track direction, submerged vegetation is dense. The SBES echogram for Transect 3 (Figure 3.19d) shows fairly continuous vegetation between approximately 100-170 m in along-track distance, and patchy vegetation from 170 m to the northern dashed line as well as between 0-80 m along the track.

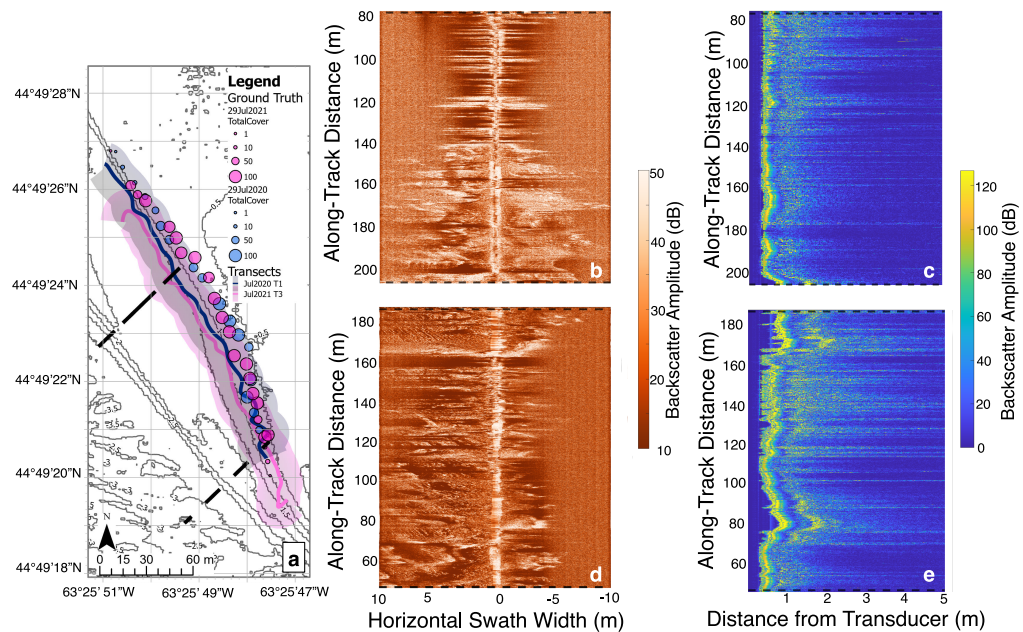


Figure 3.19: Two (a) transects and ground truth collected in July 2020 and July 2021, (b) side-scan imagery and (c) single beam echogram collected for Transect 1 on 29 July 2020, and (d) side-scan imagery, and (e) single beam echogram collected for Transect 3 on 29 July 2021 are shown between dashed lines to the northern and southern regions encompassed by all transects analyzed in this chapter. Black dashed lines indicate northern and southern extents limits between which all transects exist and are used to georeference between overlapping transects and ground truth points.

Transects in the shallow region close to the tidal flat are more densely clustered together than transects in the deeper water, and therefore there is more overlap among the data in this region. Transect 1 from August 2020 overlaps with the two transects mentioned

above across the whole SSS across-track swath width. This transect exhibits masking primarily on the shore-ward side of the side-scan imagery and masking on both sides from 120 m along the track towards the northward end. Transects 2 from July 2020 and August 2020 as well as Transect 1 from July 2021 overlap along the whole swath width with each other and partially with the previously mentioned transects. Each of these transects exhibits signs of eelgrass towards the shore-ward side of side-scan data with the exception of Transect 2 from August 2020, which exhibits masking on both sides of the transect due to the hovercraft's motion.

Two transects in deeper water in which side-scan sonar swaths overlap are compared in Figure 3.20. Side-scan and single beam backscatter data overlap in many regions in Transects 2 from 01 and 25 September 2020 between the dashed lines shown in Figure 3.20a. While the right sides of the side-scan imagery in Figure 3.20b,d is largely bare sediment, the left sides of the plots are comparable in these two figures. This region (10-0 m across-track) of the side-scan imagery in Figure 3.20b does not contain as many regions of highlights and shadows as Figure 3.20d, however, certain features along the tracks are comparable. A feature occurring in both transects found between 60-40 m along-track in Figure 3.20b and 80-60 m along-track in Figure 3.20d is of comparable size and shape and is found at similar points along the swath distance in both transects. Likewise, features found between approximately 100-80 m along the track in Figure 3.20b and 120-100 m along the track in Figure 3.20d could be indicative of the same seafloor feature. The SBES echogram for these transects (Figure 3.20c,e) show more variability in distance from the transducer, stronger seafloor backscatter returns, and second returns on 25 September 2020 than on 01 September, but high-backscatter returns from the water column that may indicate submerged vegetation exist in either transect.

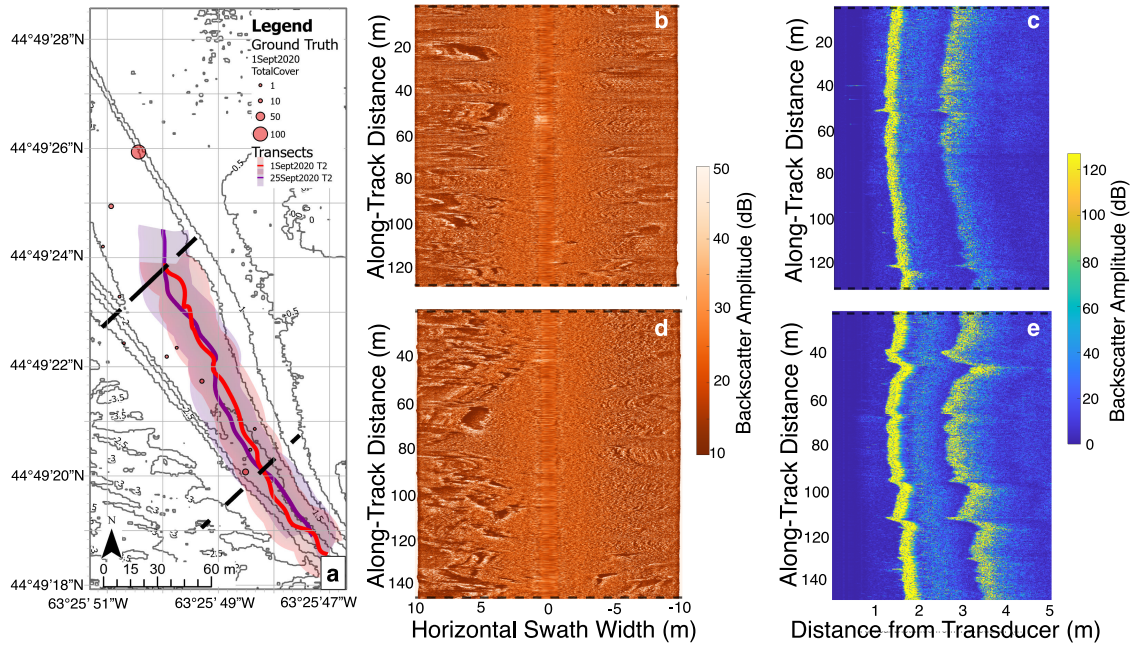


Figure 3.20: Two (a) transects and ground truth collected in September 2020, (b) side-scan imagery and (c) single beam echogram collected on 01 September 2020, and (d) side-scan imagery and (e) single beam echogram collected on 25 September 2020 are shown. Black dashed lines indicate northern and southern extents limits between which all transects exist and are used to georeference between overlapping transects and ground truth points.

While the deep water transects tend to occur further from each other spatially, there are intersections between many of the transects. Features on the seafloor in each of these transects were identified and validated based on the overlap from other transects and ground truth imagery when appropriate. Comparing these transects to one another confirmed whether the identified vegetation was legitimate or an artifact of hovercraft motion.

### 3.4.5 Seafloor Segmentation

The combined deep and shallow results for side-scan segmentation are shown in Figure 3.21 for the 50x20 rectangular patch and Figure 3.22 for the 100x50 patch. These figures show the highlights and shadows which can be combined to indicate eelgrass on the seafloor. Within beds with relatively homogeneous sediment, eelgrass typically does not grow among other vegetation species in estuaries (*Green and Short, 2003; Barrell, 2009*). Thus, the features indicated by the side-scan segmentation are all identified as eelgrass.

Eelgrass is dense in shallow regions near the shore of the tidal flat between 44°39' 19" N and 44°39' 26" N for both 50x20 patch and 100x50 patch results. In the 50x20 rectangle patch segmentation results, eelgrass seems to become more patchy north of 44°39' 26" N and as depth increases west of the shore of the tidal flat. Small patches of sparse eelgrass are identified in the deeper water including near the sandbar, on the slope towards the deep tidal channel, and even in the deepest part of the channel. In the lower-resolution segmentation results, the eelgrass density decreases more rapidly as transects move away from the shore of the tidal flat. In the deepest regions of the channel, very few features with combined highlights and shadows exist, and eelgrass patches end near the slope down to the deeper channel. Although it is possible that features in deeper water are misidentified as eelgrass and could be bedforms or algae, the channel is not deep enough that eelgrass could not grow because of light limitation.

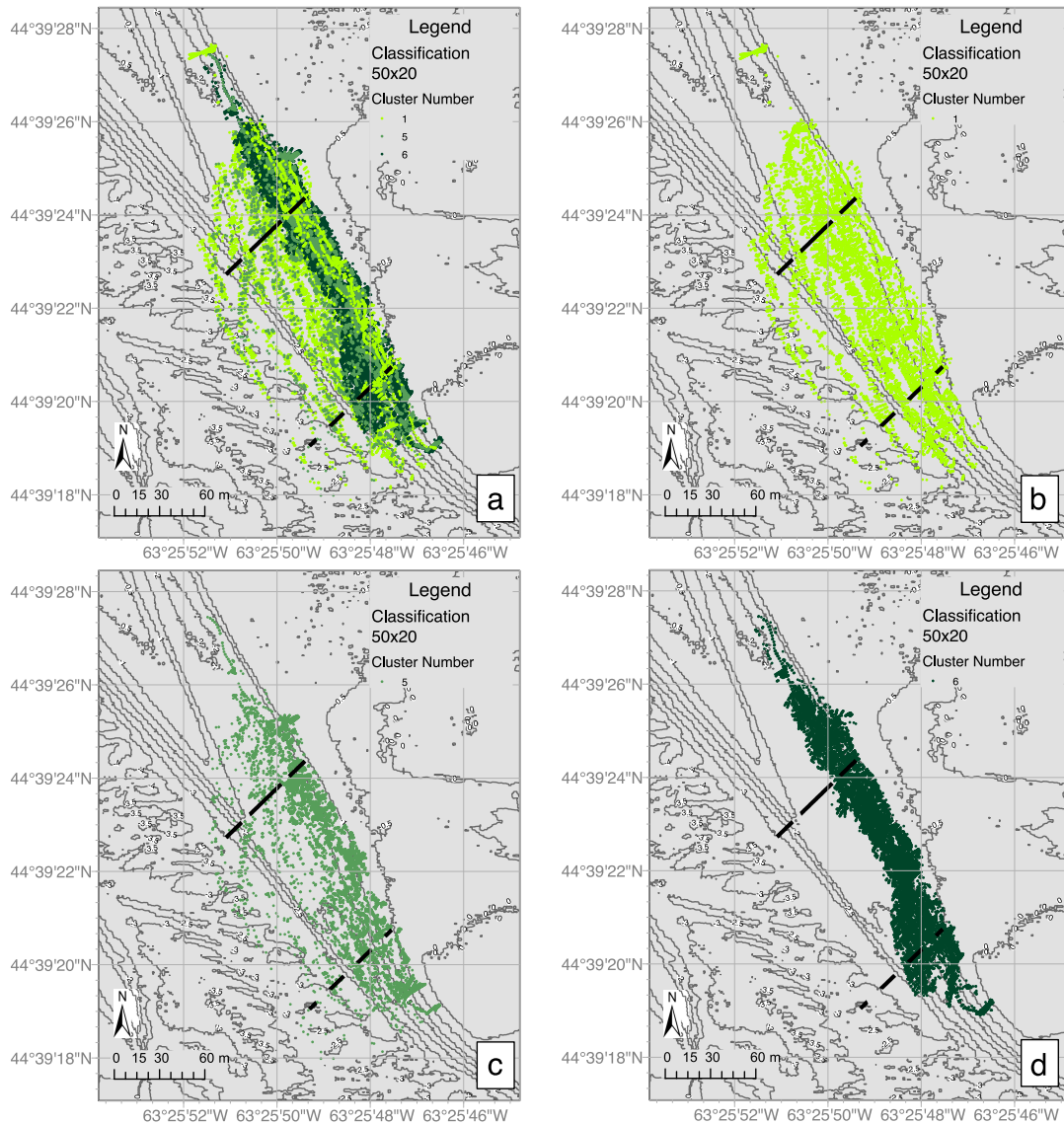


Figure 3.21: Side-scan segmentation for all transects in Cole Harbour with a resolution of 50x20 pixels and plotted to enhance either a) cluster 1, b) cluster 5, c) cluster 6, or d) all clusters. Cluster 1 indicates highlights while clusters 5 and 6 indicate shadows. Combined, these clusters indicate features on the seafloor that correspond with submerged vegetation. Black dashed lines indicate northern and southern extents limits between which all transects exist and are used to georeference between overlapping transects.

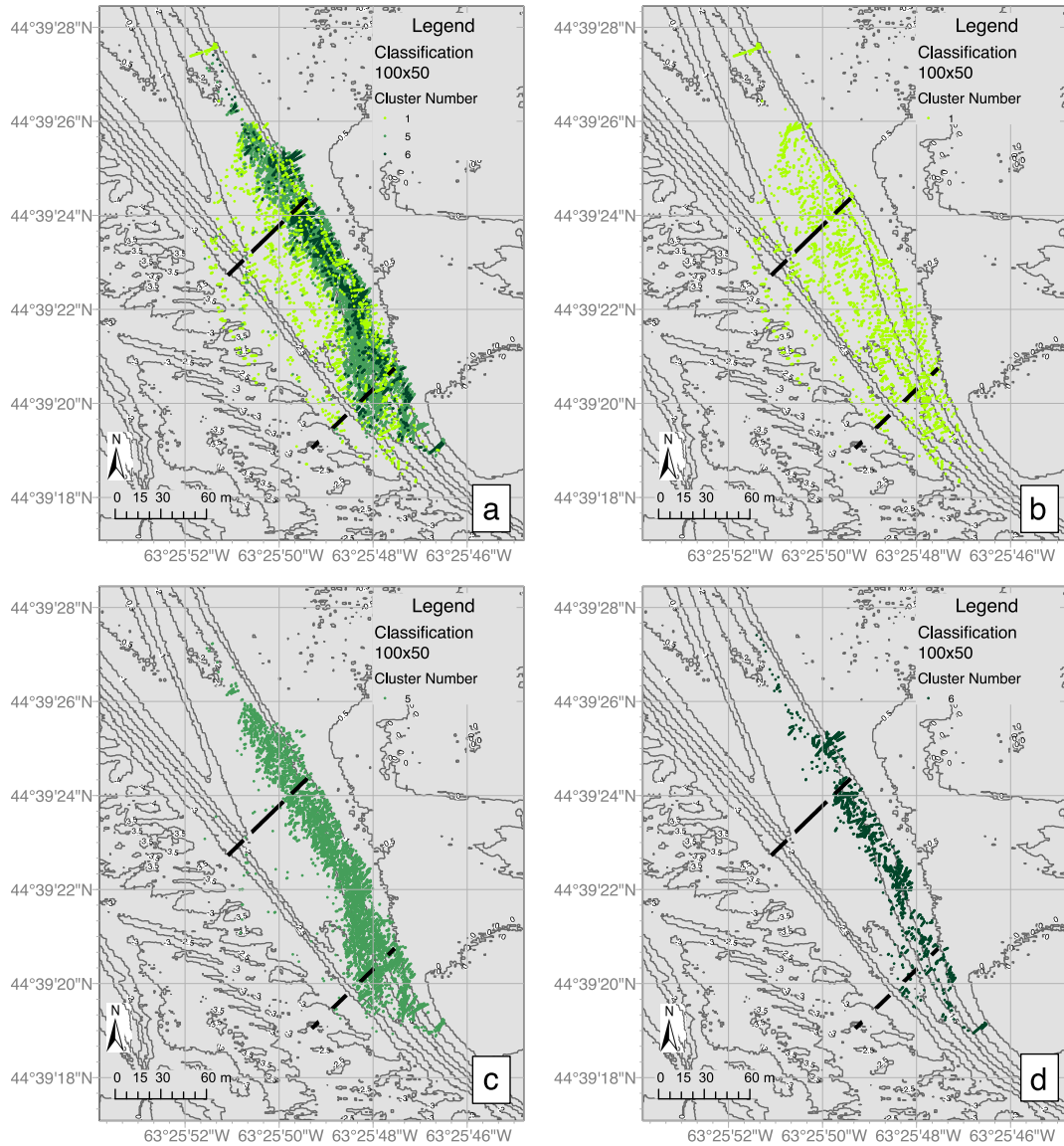


Figure 3.22: Side-scan segmentation for all transects in Cole Harbour with a resolution of 100x50 and plotted to enhance either a) cluster 1, b) cluster 5, c) cluster 6, or d) all clusters. Cluster 1 indicates highlights while clusters 5 and 6 indicate shadows. Combined, these clusters indicate features on the seafloor that correspond with submerged vegetation. Black dashed lines indicate northern and southern extent limits between which all transects exist and are used to georeference between overlapping transects.

### 3.5 Discussion

The results of this chapter were presented for three scenarios: data collected in extremely shallow water, in which eelgrass causes masking in side-scan and single beam sonar backscatter, deeper water where vegetation is rarely identified via SBES or at nadir in SSS imagery, and finally, data in which hovercraft motion affects the shape or size of vegetative features or creates artifacts on the seafloor that are likely to be segmented into seagrass features which may lead to misclassification. Figure 3.23 presents an infographic of the SWASH system’s sonar arm during each of these situations.

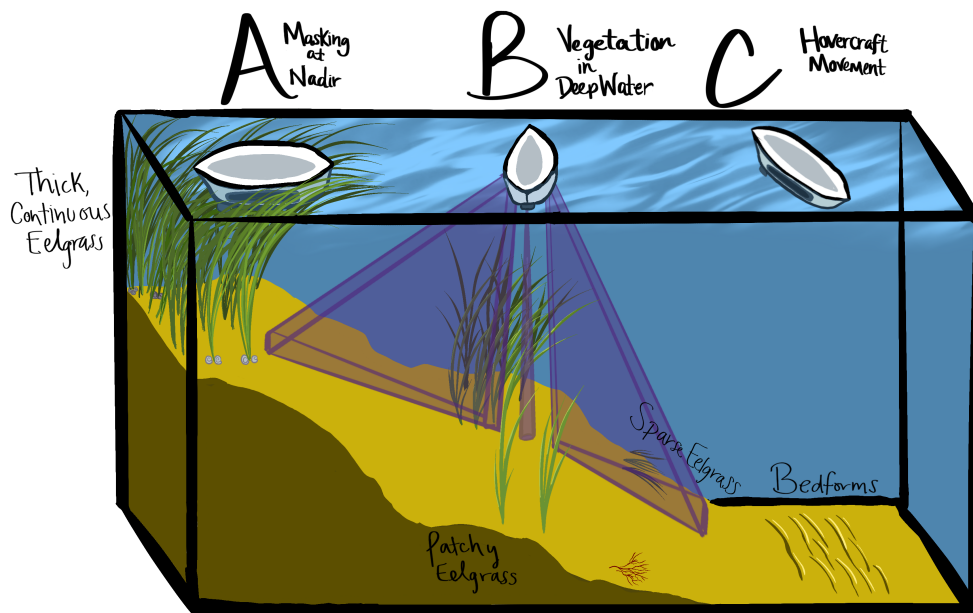


Figure 3.23: An infographic showing different physical scenarios that can be seen in the sonar backscatter data. Scenario A indicates when there are interactions between submerged vegetation and the sonar instruments, causing masking at nadir. Scenario B indicates when water is deeper and there is no interaction between vegetation and the sonar instruments. Scenario C indicates hovercraft movement, which could create effects in side-scan sonar imagery that may be falsely identified as features. The purple beams below Scenario B show an approximation of the footprint size of the single beam sonar and swath coverage of the side-scan sonar.

Vegetation-transducer interaction was seen in 6 of 15 transects analyzed for this study.

This vegetation-transducer interaction was differentiated from bare sediment in the side-scan segmentation data. A similar phenomenon to masking at nadir can be found in side-scan imagery presented by *Jones et al. (2007)*, where blurring occurs past an initial vegetation boundary. While the interaction between vegetation and the sonar transducer is not discussed in this study, a decrease in depth shore-ward of nadir caused what the authors described as blurring across the swath width. This blurring created sonar imagery in which a boundary of eelgrass is visible, but no information past this boundary in the horizontal range was able to be extracted. *Jones et al. (2007)* were able to minimize this effect by completing transects further from shore and increasing the swath width, however, this method would likely decrease the spatial resolution of the side-scan imagery and resulting maps.

*Jones et al. (2007)* also addressed an effect of motion on side-scan sonar imagery which caused a blurring effect across the whole swath width, obscuring the backscatter data. Studies like *Sheffer and Guterman (2018)* and *Li and Zhang (2020)* attempted to correct side-scan imagery for roll, pitch, and yaw changes using geometrical corrections and a heading optimization model. The pitch and roll do not noticeably affect the side-scan imagery in the data collected at Cole Harbour. Rather, the SWASH system experienced frequent changes in heading, which affected the ability to use mosaics to identify seafloor features, as well as lateral drift, in which the heading was consistent and the direction of motion changed. The latter hovercraft motion is what created larger-scale motion artifacts as seen in Figures 3.11 and 3.16.

Nine out of 15 transects examined in this chapter were grouped as deeper water transects. In these transects, eelgrass patches were identified visually and via side-scan segmentation in all of the transects. *Vandermeulen (2014)* presented side-scan imagery which contains both a dense, continuous eelgrass bed and patches of eelgrass that gradually decrease in size and number further from the densest part of the habitat. The eelgrass patches examined by *Vandermeulen (2014)* were irregular in shape and exhibited high backscatter returns

followed by shadows. Both the pattern of a dense bed which breaks off into smaller and smaller patches and the irregularly shaped eelgrass patches are similar to what is seen in transects from the SWASH surveys in Cole Harbour. In deeper water transects, some non-vegetation features were identified in side-scan imagery (i.e. features analyzed in Section 3.4.4). These features are large enough that they appear in both high and low-resolution segmentation results. Due to backscatter corrections carried out in SonarWiz, these contain high backscatter values and regions of acoustic shadow, and can therefore be misclassified as vegetation features in segmentation results. While in this case, only a few features on the seafloor were misclassified as vegetation, these instances support the need for significant validation through visual discernment of features and through validation of these features by ground truth data.

The results presented in this chapter blended visual identification of eelgrass through sonar imagery with automated segmentation based on backscatter data. Studies that have used side-scan imagery to manually map seabed features include *Brown et al. (2005)*; *Whipp and Horne (1976)*; *Cochrane and Lafferty (2002)*; *Collier and Humber (2007)*, and *Montefalcone et al. (2014)*. These studies typically digitized polygons of different seafloor types by hand based on georeferenced side-scan mosaics. Studies that have used side-scan backscatter to assist or automatically categorize different seafloor types include *Lucieer (2008)*; *Reed IV and Hussong (1989)*; *Malthus and Karpouzli (2009)*, and *Rende et al. (2020)*. *Berthold et al. (2017)* and *McLarty et al. (2020)* utilize both manual and automatic feature detection methods. Typically object-based classification algorithms in these studies produced georeferenced class polygons. These manually or automatically produced class polygons were then mapped, usually with side-scan mosaics. Side-scan mosaics were created for each survey in Cole Harbour, but due to the inconsistent speed and shape of the transects for the hovercraft surveys, these maps were deemed unhelpful for identifying vegetation. Likewise, polygons were not created nor were classes for each rectangular patch aggregated together. The classes shown in Figures 3.21 and 3.22 show both eelgrass

distribution in Cole Harbour based on combined highlight and shadow clusters as well as the density of eelgrass based on how many features are clustered close together.

While eelgrass distribution in Cole Harbour has been mapped using optical methods (*McCullough, 2005; Hanson, 2004*) and predicted through species distribution models (*O'Brien et al., 2022*) in the past, these methods have only provided coarse presence/absence results which are not descriptive of the distribution of specific eelgrass beds within the inlet. In regions where drop cameras were used for validation, the eelgrass predictions from *O'Brien et al. (2022)* consistently overestimated eelgrass presence (i.e. more false positives than false negatives). While these mapping efforts can characterize large-scale eelgrass distribution and changes in eelgrass distribution based on environmental shifts (*Wilson and Lotze, 2019*), higher-resolution observations are needed to monitor eelgrass distribution at the scales of individual beds (*Record et al., 2013*). These high-resolution, smaller-scale mapping endeavors like those carried out by the SWASH system could provide information about the health and population dynamics of these habitats before large-scale changes occur (*O'Brien et al., 2022; Wilson and Lotze, 2019*).

### **3.5.1 Single Beam Classification**

The SBES segmentation methods in this study were modeled after those applied by existing seabed classification tools such as Quester Tangent (QTC) View and Impact, BioSonics Visual Bottom Typer (VBT) and EcoSAV, and RoxAnn (*Quester Tangent Corp., 2004; Sabol et al., 2002; Vandermeulen, 2011; Hamilton, 2001*). These tools use the properties of the first (*Quester Tangent Corp., 2004*) and second (*Sabol et al., 2002; Vandermeulen, 2011; Hamilton, 2001*) seafloor returns to identify differences between profiles and groups accordingly. QTC and BioSonics VBT both use Principal Component Analysis (PCA) before clustering to reduce dimensionality in the properties calculated from the seafloor returns. While PCA was used during one attempt at SBES clustering in Cole Harbour, the resulting segmentation results did not show significant differences between clustering methods that did or did not reduce dimensionality.

According to the QTC Impact user manual (*Quester Tangent Corp.*, 2004), some of the most common flaws in echo sounder data include low signal-to-noise ratio (i.e. weak echos or strong baseline noise), clipping, and acoustic or electrical interference. Clipping is more common in water shallower than 5 meters, while background or baseline noise can be increased by cavitation, engine noise, or reverberation. Acoustic or electrical interference can be caused by other sounding instruments or poor electrical connections respectively and will add noise to the SBES profiles. Many studies provide examples of submerged vegetation accurately identified using echograms (*McCarthy*, 1997; *McCarthy and Sabol*, 2000; *Sabol et al.*, 2007; *Stevens et al.*, 2008; *Barrell et al.*, 2015; *Barrell and Grant*, 2013; *Ferretti et al.*, 2017; *Gumusay et al.*, 2019; *Stocks et al.*, 2019). Like the SBES data from this thesis, the backscatter data collected by (*Stocks et al.*, 2019) shows clear interaction between surface noise or transducers and vegetation, however, this study manually distinguished submerged vegetation from bare sediment and thus does not examine the effects of this noise might have on the success of a classification algorithm. Backscatter data from *Ferretti et al.* (2017) show clipping in individual echo sounder profiles from a rocky seabed but these returns were able to be differentiated from vegetated seafloor returns, which did not exhibit clipping.

Many of these flaws were exhibited in the SBES data collected for this chapter, which likely affected the ability of the algorithm to segment the seafloor based on seafloor properties. The shallow water transects collected at Cole Harbour were segmented into four clusters which did not identify vegetated or non-vegetated returns, but rather returns in which backscatter maximums overlapped with the surface noise, returns with higher water column backscatter amplitudes, and returns with neither. Similarly, deep water SBES segmentation yielded two clusters: one with large backscatter returns in the water column, and one without. These SBES clustering methods did segment profiles with similar signals together, but the interaction between the first backscatter return and the transducer and higher water column backscatter amplitudes overpowered the signals with vegetation.

### **3.5.2 Evaluating the SWASH System for Seabed Mapping**

The survey presented in this chapter was used as a case study for whether the SWASH system could effectively map vegetation in Cole Harbour, Nova Scotia. Based on the sonar imagery and side-scan segmentation results in this study, the distribution of an eelgrass bed in Cole Harbour was mapped. Nevertheless, there were a number of complications that arose due to the limitations of the system. It is likely that some of the flaws in the SBES backscatter data could be solved by surveying during high tide when water is a bit deeper around the densest region of the eelgrass bed. This would require the base station to be positioned at the high marsh, or even on the beach at Deployment Location 1 (Figure 3.2). However, the telemetry range of the SWASH system is <500 m and this connection is required for programmed actions such as raising and lowering the sonar arm as well as transmitting navigation and orientation data as a backup. Furthermore, the hovercraft's ability to fly in a straight line is impacted by wind and current velocities.

Though the hovercraft has nearly frictionless movement against a surface, the sonar arm does add some lateral resistance. This center of resistance is located at the very front, or bow, of the craft, while the thrust from the fan is located at the rear or stern. This arrangement of forces can lead to instances where the craft must navigate along an unstable equilibrium to maintain a constant heading. For example, navigating against the current with a wind arriving on the beam made holding a constant heading, particularly challenging, where the fan had to constantly apply some amount of lateral thrust. The physical opposition of wind and fast currents in the region were common, bolstered by a strong tidal flow in and out of the Cole Harbour estuary, and open exposure to southerly ocean winds. These factors combined caused difficulties in maneuvering the hovercraft which were expressed in the data as artifacts of side-scan sonar motion. These artifacts can easily be misclassified as eelgrass.

While there are a number of possible disadvantages present with the use of the SWASH platform as a method of surveying in extremely shallow water, there are benefits as well.

During some surveys, the turbidity at the study site was high, which would limit the effectiveness of satellite and aerial data products. Furthermore, the study site of Cole Harbour is located within a no-drone zone for UAVs due to the proximity of the Shearwater Air Base (*National Defence*, 2021). In order to legally fly a UAV in this region, a valid drone Pilot Certificate – Advanced Operations is required in order to apply for permissions. Thus, an uncrewed surface vehicle can provide higher-resolution data than satellite imagery and is less restrictive than UAVs in terms of where and how it can be operated. Compared to other USVs, the hovercraft is an ideal option because it has no underwater propulsion mechanisms and is non-invasive. As a platform for seabed mapping in extremely shallow water (<1 m), the SWASH system did not perform well enough to be considered a viable option for larger-scale surveys, however, with more research and technical developments, the SWASH system could overcome these limitations and provide a method of creating high-resolution maps in infrequently surveyed regions. For example, mechanical upgrades to the SWASH system to increase the power such as splitting the lift and thrust mechanisms into two different motors and moving the position of the deployed sonar instrument to the craft's center of mass would increase the hovercraft's stability in the water and the consistency of the heading, decreasing the effect of hovercraft motion on sonar data.

### **3.6 Conclusions**

Globally, eelgrass populations are on the decline (*Gumusay et al.*, 2019; *Green and Short*, 2003), and (if trends observed between 1992 and 2002 have not stopped) have likely continued to decline in Cole Harbour as well (*Hanson*, 2004). Eelgrass is a foundation species that provide food and habitat to many marine species, decreases erosion and turbidity due to sediment suspension in the water column, and acts as an important step in the nutrient cycling process. Frequent monitoring is necessary to observe and mitigate the effects of this habitat loss.

The SWASH system provided a way to monitor the spatial distribution of an eelgrass

bed in Cole Harbour, Nova Scotia. Eelgrass was identified visually through the single beam and side-scan sonar imagery and through the segmentation of side-scan backscatter data. Even at peak growing season, this eelgrass bed is relatively patchy, varying from sparse to thick eelgrass with patches of bare sediment between both thick and sparse cover. Thick eelgrass was identified in a long, largely continuous patch approximately 200 m in length along the shore of the tidal flats. Towards deeper water bounded by a sandbar, eelgrass patches become less frequent. This distribution pattern is in agreement with ground truth data collected on July 29, 2020, July 29, 2021, and September 01, 2020. This pattern is also in agreement with literature including *Vandermeulen (2007)*; *Stevens et al. (2008)* and *McCarthy (1997)*. If current limitations with the SWASH system, like such as the inconsistency of hovercraft heading and proclivity to drift, the relatively small telemetry range between the base station and rover, and the single fan mechanism that produces both lift and thrust, can be solved, this region could benefit from more surveys. Further surveys in this region could provide more information about the distribution of this eelgrass, including other important information such as canopy height in different regions of the bed. With further research, seasonal and annual dynamics of the eelgrass population could also be discovered.

The development and testing of novel platforms is key in finding solutions for mapping and monitoring in regions where data is lacking. Over the past few decades, much progress has been made to streamline both instruments and novel platforms for uncrewed surveying endeavors (*Wölfl et al., 2019*; *Mayer et al., 2018*; *Agrafiotis et al., 2018*; *Gavazzi et al., 2016*). This chapter examined whether the SWASH system could complete surveys in extremely shallow water and provide data to create maps in these infrequently surveyed regions, as it was designed to do. While limitations arose during data collection and analysis, the SWASH system did produce data that was able to be analyzed and extracted to eelgrass distribution maps. In the future, with further developments and improvements, the SWASH system may become more successful at providing meaningful data in areas

where they are needed.

---

## CHAPTER 4

---

# MAPPING SURFICIAL SEDIMENT IN ROSEWAY BASIN, NOVA SCOTIA USING BACKSCATTER FROM A SINGLE-BEAM PROFILING SONAR

### 4.1 Introduction

Underwater gliders have been a concept discussed by oceanographers as early as the 1960s, yet were not developed and fabricated until the late '80s and early 1990s (*Oversmith and Leadon*, 1962; *Rains*, 1968; *Webb et al.*, 2001). Gliders are a type of autonomous underwater vehicle (AUV) that use negative or positive buoyancy as a propulsion technique (*Javaid et al.*, 2014). When first deployed, these gliders have negative buoyancy, and thus tilt to move downward. When the glider reaches a predetermined depth, the buoyancy changes, and the glider tilts up and moves upwards through the water column. In 1995, three different underwater gliders were prototyped by Naval Research's Autonomous Oceanographic Sampling Network (*Javaid et al.*, 2014). Each of these had a similar form and size, with torpedo-shaped bodies, and wings for stabilization, and were just small enough to fit on small oceanographic vessels. The "Spray" and "Seaglider" were optimized for deep ocean missions, while the "Slocum" was built for fast turning and vertical velocity, and was best suited for shallow water missions.

Slocum gliders are now used globally for a myriad of surveys, including (but in no way limited to): whale tracking (*Davis et al.*, 2016), iceberg profiling (*Zhou et al.*, 2019), studying turbulence (*Wang et al.*, 2018), chlorophyll concentrations (*Buckingham et al.*, 2020; *Carvalho et al.*, 2020), oceanographic measurements such as dissolved oxygen, temperature, and salinity (*Pattiaratchi et al.*, 2017; *Kerfoot and Aragon*, 2020), and passive acoustics for seabed classification (*Jiang et al.*, 2021). Each type of survey requires different instruments, and for those instruments to be optimized for a specific purpose. These surveys produce large datasets, most of which are only analyzed in the context of the originally proposed application. For example, the Coastal Environmental Observation Technology and Research (CEOTR) group at Dalhousie University carries out glider missions each year on the Scotian shelf in order to track Atlantic Right using both passive and active acoustic sensors (*CEOTR*, 2022). Some of these surveys were carried out using a Slocum glider equipped with a single-beam echo sounder used for profiling the water column to measure zooplankton density, which can be used to predict the presence of predators (including baleen whales). The single-beam seafloor returns, however, are largely unused and could provide information on the geophysical properties of the seafloor sediments.

Single-beam echo sounder returns have been used for ground discrimination for several decades (*Smith and Nichols*, 1953; *Smith and Li*, 1966). While properties such as sediment porosity and density are often inferred from seafloor and sub-bottom returns, changes in backscatter from the seafloor could also be due to surficial sediment roughness or bedforms, which could range in horizontal scale from centimeters to kilometers (*Symons et al.*, 2016). Seafloor sediment distribution maps can be useful tools for spatial planning, resource management, and habitat mapping and conservation (*Galvez et al.*, 2021; *Valentine*, 2019; *Misiuk et al.*, 2018). Increased accuracy of these distribution maps will also increase the understanding of the physical characteristics of seafloor substrate, and how it affects benthic communities on the seafloor. The substrate of an environment can impact how and

where habitats establish and how they may recover if populations are in decline (*Dernie et al.*, 2003). For example, *Collie et al.* (2000) state that benthic habitats that have been disturbed by either anthropogenic or natural causes found in homogeneous sediments (i.e. sand or mud) tend to recover more quickly than heterogeneous sediments (i.e. sandy mud). This information is important when determining how best to extract certain resources which could be harmful to benthic communities (i.e. bottom trawling), and which regions must be protected by restrictions.

In this study, single-beam seafloor backscatter returns from two Slocum glider missions deployed on the Scotian Shelf were examined to determine whether seafloor geophysical properties can be extracted from the single-beam backscatter returns through segmentation of averaged backscatter profiles and calculation of effective backscattering coefficients. Multidimensional scaling and density-based clustering were used to segment the seafloor backscatter returns based on differences in the seafloor returns which could indicate changes in the geophysical properties of the surficial sediment. Based on backscatter statistics, the resulting segments were then interpreted to be different types of surficial sediment, i.e. different combinations of sand, mud, and gravel. The segmented seafloor types were compared to bathymetry, physical grab samples, and a map of the surficial geology in the region, while SBES-derived effective backscattering coefficients were compared to estimated reflection coefficients using physical grab sample grain size and surficial geology descriptions. This study showed that geophysical information about seafloor surficial sediment could be inferred from backscatter returns obtained using a single-beam sonar calibrated to short range. These results can be used to fill gaps in sediment distribution maps as well as increase the accuracy of sediment distribution models, which is important for mapping habitats as well as mitigating negative effects on benthic populations.

## 4.2 Objectives

The objectives for this chapter were to:

- Isolate seafloor backscatter returns from two Slocum glider missions in 2014 and 2015 respectively.
- Utilize a clustering algorithm to segment seafloor echo sounder returns into distinct groups based on their backscatter characteristics.
- Compare segmentation results and effective backscattering coefficients against bathymetry, physical grab samples, and surficial geology maps.

## 4.3 Study Site

Off the south-eastern Nova Scotian coast lie a series of basins and banks formed by glacial erosion (*Vilks and Rashid, 1976; Piper, 1991*). Some of these basins can reach depths of 300 meters, while the banks can be as shallow as 50 meters. The sedimentology of the basins includes glacial till, overlaid by silt and clay, while banks consist of well-sorted sand, gravel, and boulders (*King, 1970; Vilks and Rashid, 1976*). Recessional moraines (i.e. material left behind by the Laurentide Ice Sheet) are found throughout this region and are typically present as buried or exposed ridges around the central shelf (*Todd, 2016*).

The glider missions presented in this study were planned around Roseway Basin, which begins approximately 20 km off the coast of Nova Scotia and consists of two sub-basins bisected by an exposed recessional moraine ridge (Figure 4.1). Roseway Basin occurs between Browns Bank to the southwest and Roseway Bank to the northeast. Baccaro Bank lies to the east and Browns Channel lies to the west/southwest. Bedforms such as ripples and dunes have been found in both the soft sediment of basins and the coarser sediment of banks (*Todd and Kostylev, 2011*). In particular, pockmarks, or conical indentations in

the soft sediment, have been found in Roseway Basin (*King and MacLean, 1970*). These features can vary from 15 to 45 meters in diameter and 5 to 10 meters in depth. The hydrographic structure of water masses on the Scotian shelf changes from 2-layers in the winter to 3-layers in the summer when a warm surface layer is formed (*Loder et al., 1997*). Previous modeling studies have shown that circulation in the region is typically weaker in the summer and fall and stronger in the winter and summer (*Han et al., 1997*).

Roseway Basin is the study area of many oceanographic and biological surveys as well as geological surveys. The endangered North Atlantic Right Whale typically summers in the coastal waters of the United States and Canada (*van der Hoop et al., 2012*). During these times, the probability of vessel strikes is high, leading to voluntary seasonal restrictions on vessel routes. The region surrounding Roseway Basin is one of these restricted areas and has been diligently surveyed using autonomous underwater vehicles since 2013 (*CEOTR, 2022*). The high number of surveys in this region is particularly ideal when working with data sets that are noisy or difficult to interpret because there are a number of ways to verify the results of the analysis.

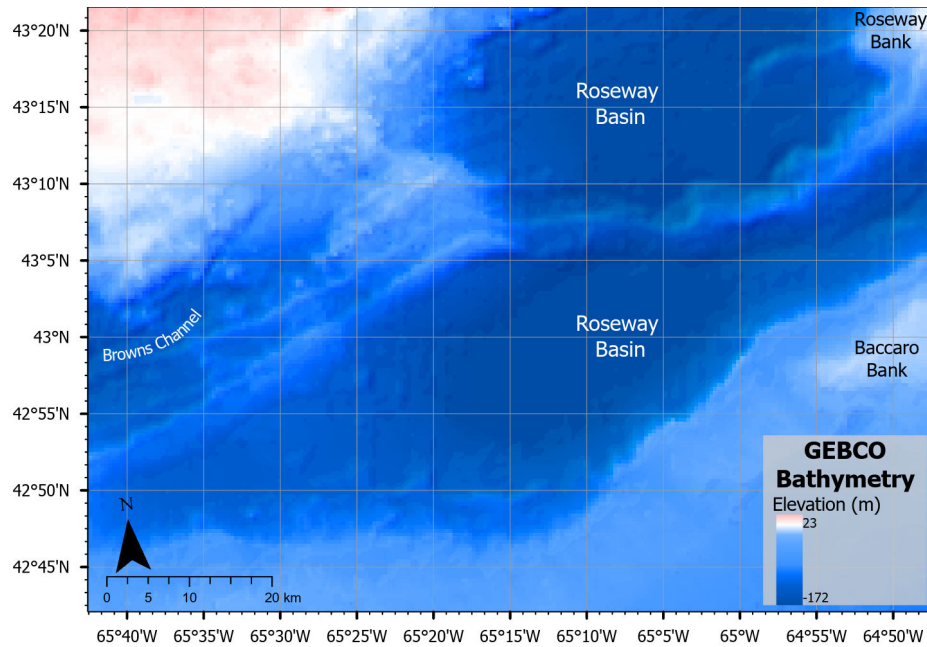


Figure 4.1: GEBCO bathymetric digital elevation model for Roseway Basin and surrounding features (*GEBCO Compilation Group, 2022*). The sections of Roseway Basin and surrounding banks and channels are labeled.

## 4.4 The Data Sets

### 4.4.1 Glider Data Collection

This study analyzes two Slocum glider missions that took place in 2014 and 2015 at Roseway Basin, off the southern shore of Nova Scotia. Table 4.1 contains information about each of the missions examined in this study and the gliders used in each survey. These surveys were carried out by the CEOTR group using Teledyne Webb Slocum gliders equipped with instruments to collect environmental data such as temperature, salinity, oxygen concentration, optical backscatter, and passive acoustics among other properties (*Davis et al., 2016; CEOTR, 2022*). A 300 kHz Imagenex single-beam echo sounder was equipped on the glider used in these missions for the objective of using backscatter to identify plankton in the water column. The echo sounder has a conical beam width of 10°, a ping rate of 0.25 Hz, and a pulse length of 100 $\mu$ s. The echo sounder was calibrated once

per year using titanium spheres with known acoustic reflectivity. This calibration ensures that the echo sounder is sensitive to particles of 1.6 mm, up to 10 m from the transducer. In this study, each glider mission will be referred to by its CEOTR-designated number, mission 38 which occurred in 2014, and mission 51 which occurred in 2015.

The first glider mission (mission 38) examined in this study occurred over 22 days from October 6, 2014, to October 28, 2014, and was carried out for the purpose of collecting water column backscatter data in Roseway Basin (*CEOTR, 2022*). This mission consisted of 7 parallel transects of varying lengths oriented in a northwest/southeast direction. The second glider mission (mission 51) examined in this study occurred over 88 days from 14 September - 11 December 2015. This mission comprised of 15 transects in approximately the NW/SE directions and 2 transects in the NE/SW direction.

The echo sounder was mounted at an angle such that it was downward facing when the glider was descending towards the seafloor (i.e. the downcast). The backscatter amplitude from the seafloor return was consistently the maximum value able to be recorded by the sonar instrument at ranges <60 m between the transducer and the seafloor, and at ranges >90 m from the seafloor, backscatter amplitudes are very low and there do not exhibit variability across glider transects. Thus, the data analyzed in this study were collected on glider downcasts when the glider was between 85-65 meters from the seafloor in order to optimize differences in backscatter.

Mission Number	Mission Dates	Glider Name	Instruments	
			Make/Model	Measurement
38	6-28 October, 2014	otn201	Imagenex 853es	Backscatter (300 kHz)
			SeaBird GPCTD	Conductivity, temperature, pressure
			Anderaa Optode 5013w	Oxygen concentration/saturation
			WetLabs ECO triplet	Chlorophyll a and CDOM fluorescence
			Satlantic OCR 504i	Multispectral irradiance
51	14 September - 11 December, 2015	dal556	Imagenex 853es	Backscatter (300 kHz)
			SeaBird GPCTD	Conductivity, temperature, pressure
			Anderaa Optode 5013w	Oxygen concentration/saturation
			WetLabs ECO triplet	Chlorophyll a and CDOM fluorescence
			Satlantic OCR 504i	Multispectral irradiance
			WHOI DMON	passive acoustics up to 1Hz

Table 4.1: Glider missions examined in this study with glider name, dates, and glider instrumentation (*CEOTR*, 2022).

#### 4.4.2 Seafloor Environmental Data Sets

Cluster outputs were compared against bathymetric data and surficial sediment type from distribution maps by *Philibert et al. (2022)* and grab sample data collected by the *USGS (2014)* and the *GSC (2020)*. Gridded bathymetry data were downloaded from the General Bathymetric Chart of the Oceans (GEBCO) at 15 arc-second grid resolution (*GEBCO Compilation Group, 2022*).

Physical grab sample data were downloaded from the Geological Survey of Canada (GSC) (*GSC, 2020*) and the U.S. Geological Survey (USGS) East Coast Sediment Texture Database (*USGS, 2014*). These data included the date and position (latitude, longitude) of the grab sample, water depth, sample type, top and bottom depth of the sample below the sediment-water interface, mean grain size of the sample, and the composition of the grab samples in the form of percent gravel, sand, silt, clay. The percent mud was calculated by adding the percentages of silt and clay together. These data sets also included the Folk classification based on percentages of grain size, comments about the grab sample, and lithological description. The data were quality controlled to ensure that the sediment components added up to 100% and only surface sediment samples were used. Samples were isolated to those near the glider track (within the bounds of 42°N to 43.45°N and -65.6°W to -64.78°W). Data from the USGS and the GSC data sets within these bounds were merged together and if two or more grab samples were collected at the same latitude and longitude position, these data points were averaged together.

From the merged grab samples analyzed, 92 point samples were within the study area bounds (i.e. close to both glider Mission 38 and 51). The sediment distributions are shown in Figure 4.2. The 2-dimensional Euclidean distances between physical grab samples and observations from both glider missions were analyzed in order to compare the percent grain size to glider data. The mean grain size was also used to estimate density and sound speed for each grab sample using the regression equations comparing both grain size and sediment density with the sound speed ratio presented in *Bachman (1989)*. Reflection

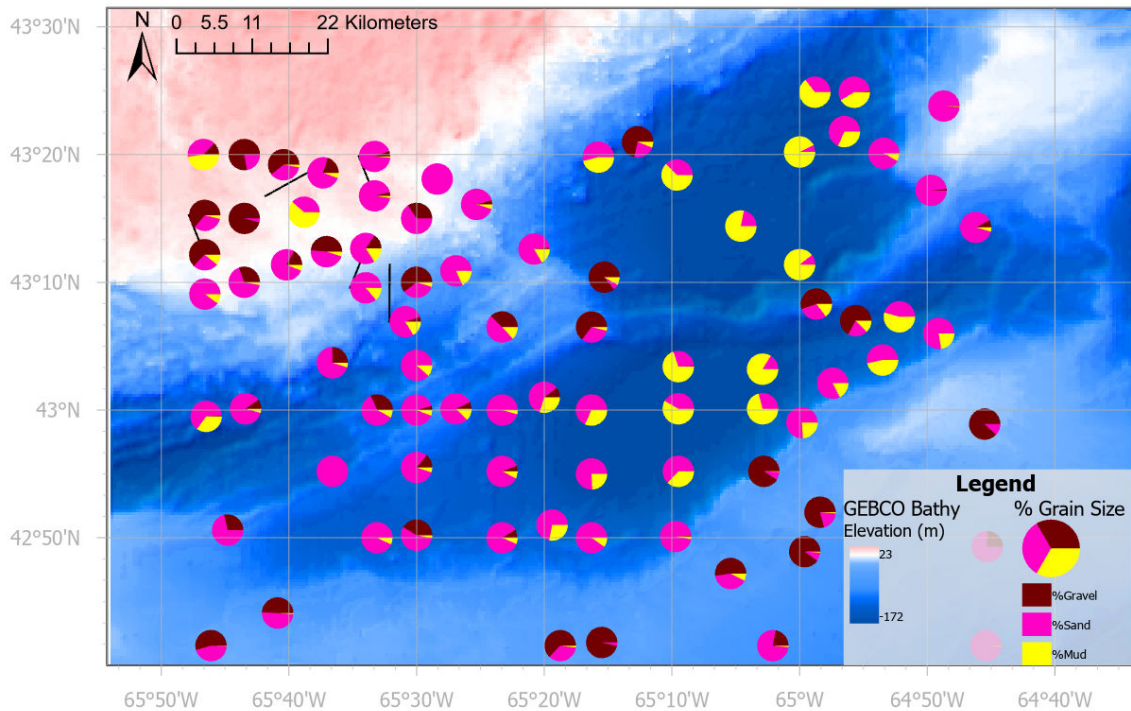


Figure 4.2: Physical grab samples showing percent sediment grain size (Percent gravel, sand, and mud) as pie charts plotted above GEBCO bathymetry. Black lines leading from individual grab-sample pie charts indicate locations of these data points where points were displaced due to space.

coefficients for the grab samples were then estimated using these sound speed and density calculations.

A map of the surficial geology of the Scotian Shelf Bioregion was updated and compiled by the Geological Survey of Canada (*Philibert et al.*, 2022), which is based on earlier interpretations by *Fader et al.* (2004) and *Piper* (1991). The updated surficial geology maps (*Philibert et al.*, 2022) integrated additional sediment distribution maps, high-resolution hydroacoustic data including MBES and SBES, bathymetric LiDAR, and seismic data to update the surficial geology maps in this bioregion. The geological units from each source integrated were named and categorized by *Philibert et al.* (2022) to be the same for every region. At the study site, the surficial geology includes Postglacial Transgressive

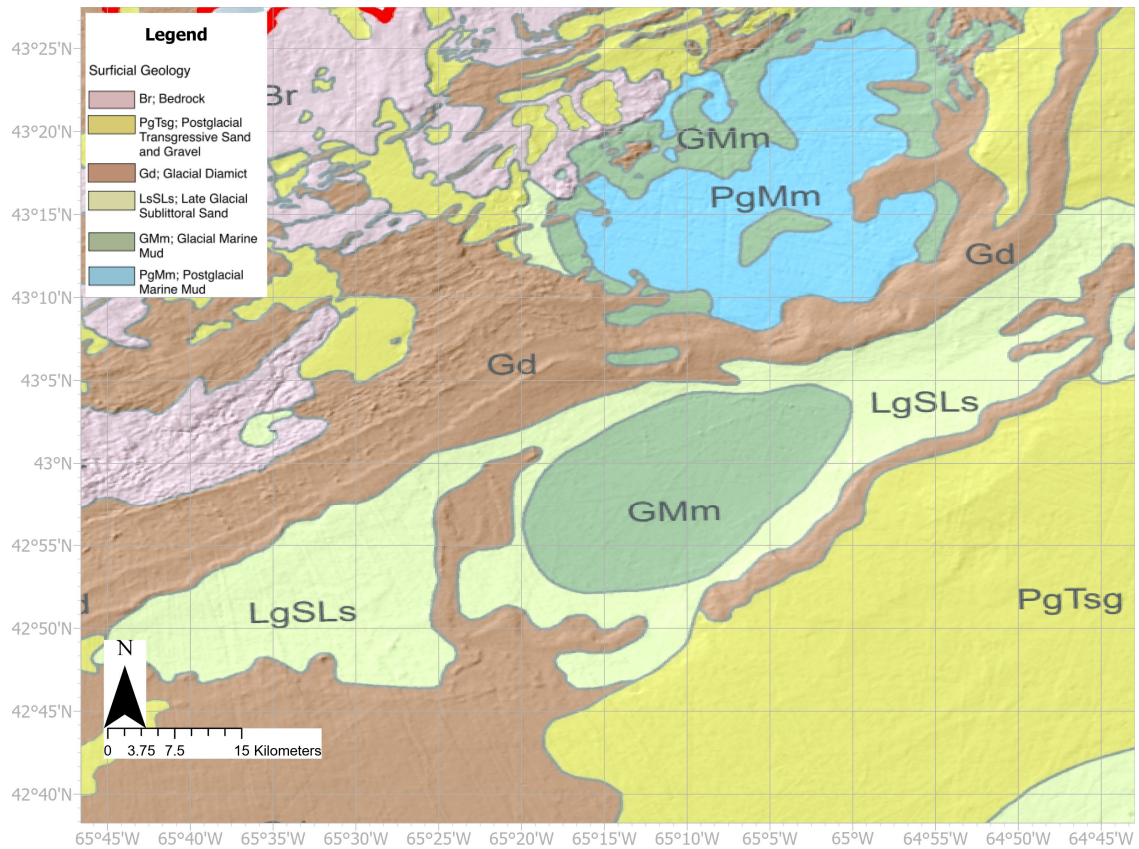


Figure 4.3: Map of updated surficial geology compiled by *Philibert et al.* (2022). Descriptions for each geological unit are shown in Table 4.2.

Sand and Gravel (PgTsg), Late Glacial Sublittoral Sand (LgSLs), Glacial Marine Mud (GMm), Postglacial Marine Mud (PgMm), Glacial Diamict (Gd), and Bedrock (Br). These geological units from *Philibert et al.* (2022) are described in Table 4.2. This map was georeferenced in ArcGIS using 10 points of reference.

Geological Unit	Description
Br Bedrock	Dominated by bedrock of various types and ages. Inner shelf areas dominated by granite or very competent schist, shale, or quartzite of Paleozoic age. Generally more diverse, older and competent rock types off Cape Breton. Mid and outer shelf outcrops are rare, mainly in the canyon walls along the continental slope, and comprise less competent Cenozoic age shales and sandstones. Inner shelf bedrock exposures are generally higher relief than in sediment-covered areas, exhibiting exposed mound or ridge and intervening hole or trough relief, reflecting alternating rock types or differential glacial sculpting. Relief can also be governed by bedrock structure, jointed or faulted; regional patterns can follow broad fold structure. Depressions are commonly partly sediment-filled, washed from the adjacent highs under past coastal conditions. This fill is generally patchy and can be composed of thin mud, sand, gravel and cobble or boulder lags and less commonly pockets of till or moraines.
PgTsg Postglacial Transgressive Sand and Gravel	Predominately composed of sand, gravelly sand or patchy gravel. Generally present on banks and the inner shelf in water depths less than 120 m. Generally less than 1–2 m thick, but much thicker on eastern outer shelf banks. Comprises the coarser remnants of reworked glacial deposits and other bank sediments following glacial retreat when low sea-level exposed them to subaerial weathering and erosion. Reworked and transported by wave and current action in littoral and sublittoral environments during the subsequent transgression (late Pleistocene and early Holocene). The finer grained sublittoral facies equivalents of this unit are LgSLs. Much of the sand was swept off bank areas, contributing to shelf-edge canyon development (erosion) and thalweg deposits. Some was preserved in thick (many metres), prograded sheets in an evolving transport pattern with sea level rise. Some entire banks were swept free of sand, leaving dominant gravel distribution. These sediments (up to small gravel size) can be reworked and redistributed in the upper centimetres or decimetres by bottom currents and storm waves. Patchiness is generally governed by diverse bedforms (dunes) generating sandy crests and gravelly troughs with metres to hundreds of metres spacing, especially in shallow (<30 m) water. Relict bedforms can be locally preserved in deeper areas. Time-transgressive genesis, from time of glacial retreat in deeper water depths to present day in shallow water depths. Locally reworked into periodically active bedforms (sand with gravel troughs), locally deeper in current-influenced channels.
Gd Glacial Diamict	Poorly sorted homogeneous mixtures of mud with matrix-supported sand, gravel and cobble clasts. Generally competent. Dense to very stiff. Diamict can be referred to as glacial diamict or till where recognized as being deposited in direct contact with ice. Diamict has strong glacial origin in the study area, but is not necessarily all till. Commonly occurs on the inner shelf as multiple moraines at various scales. Less commonly occurs as drumlins, grounding zone wedges or variably thick (up to tens of metres) blankets with glacially sculpted surface (fluting or similar glacial lineations), indicating a subglacial and glacial margin origin. Its upper surface is commonly iceberg-turbated along the flanks of banks and shelf edge. Commonly overlain by sand and gravel and boulder lag deposits or by glacial marine mud and postglacial mud. Generally differentiated from map unit Br by geomorphic elements, samples, or homogeneous body character where seismic profiles depict acoustic penetration which is not common in bedrock. Chronology assessments invariably indicate deposition during the last glaciation, but with a complex and time-transgressive glacier flow and margin retreat pattern governed by basin and trough elements yet with a general retreat from west to east and from the shelf edge to the shoreline.
LgSLs Late Glacial Sublittoral Sand	Muddy sand or silt with little gravel. Generally a thin (<1 metre) wedge, thinning significantly in deeper water depth. Generally restricted to a band along bank edges and along submarine terraces in water depths >120 m, but may also be found in small embayments. Deposited in a mostly proglacial environment, along the littoral of the Late Pleistocene shoreline during sea level low stand. Locally reworked into periodically active bedforms. May overlie glacial diamict and may underlie postglacial sand and gravel. Some time equivalency with latest deposits of GMm and earliest PgMm and PgTsg.
GMm Glacial Marine Mud	Clayey to silty mud with variable content of scattered clasts. Distributed principally partially infilling large basins on the shelf in over 110 m water depth, overlying or locally interfingering with the glacial diamict map unit (Gd), near paleo-glacial margins. Up to tens of metres thick, generally >15 m, while thinning to zero at basin margins. Generally covered with postglacial mud (PgMm) in basins, but in shallower water depths commonly occurs as pockets in smaller topographic lows. Locally the uppermost surface has been partly eroded (up to several metres removed), developing a thin (centimetres to decimetres) surficial sandy and/or gravelly lag (PgTsg). Deposited during the last glaciation (~20 to 14 ka) beyond the ice sheet by proglacial meltwater plumes in a proximal to distal marine environment. Proximity of the ice front can be tens of kilometres distant, influencing the texture of the unit. Where present, clasts are generally ice-rafted debris while sand or mud layers were deposited from turbidity currents.
PgMm Postglacial Marine Mud	Mud consisting mostly of silty clay and clayey silt. Corresponds to the winnowing of silt and clay from glacial debris on banks during late Pleistocene and early Holocene sea-level rise, where finer material was deposited in lower lying depressions. This postglacial sediment has a predominantly ponded sedimentary style. Overlies glacial drift and glacial marine mud. It is a lateral equivalent to the postglacial sand and gravel. Mainly confined to basins and local depressions on the shelf.

Table 4.2: Descriptions of the geological units at Roseway Basin from *Philibert et al. (2022)*.

## 4.5 Data Processing

Backscatter profiles from the glider downcasts between 65-85 meters from the seafloor were isolated. Figure 4.4 shows what the entire glider downcast might look like in comparison to the portion of data within each downcast isolated for this study. These profiles were extracted for analysis because the seafloor returns in shallower portions of the downcasts were consistently at the maximum received value for the transducer, while seafloor returns that were further than 85 meters away from the transducer were below the noise floor of the profiles. The seafloor returns were then isolated for each echo profile and the returns.

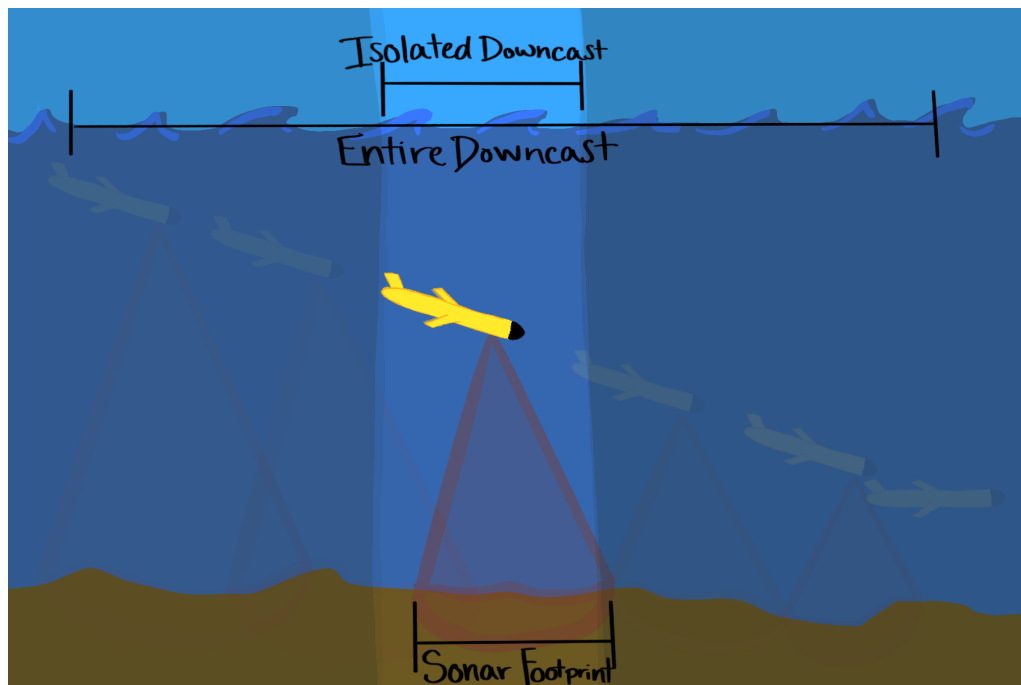


Figure 4.4: An infographic showing a Slocum glider downcast and the portion of the downcast isolated for processing in this study. An example of the sonar footprint on the seafloor for a ping is also indicated (not to scale).

### 4.5.1 Segmentation Methods

#### 4.5.1.1 Pre-processing of Single Beam Echo Sounder Data for Segmentation

Seafloor returns were then corrected for spherical spreading and attenuation by adding the two-way transmission loss to the seafloor return data:

$$2(20 \log_{10} r + \alpha r/1000), \quad (4.1)$$

where  $r$  is the range from the transducer to the seafloor and  $\alpha$  is the simplified absorption in dB/km, calculated using the equations given in *Ainslie and McColm* (1998):

$$\begin{aligned} \alpha = & 0.106 \frac{f_1 f^2}{f^2 + f_1^2} e^{(pH-8)/0.56} \\ & + 0.52 \left(1 + \frac{T}{43}\right) \left(\frac{S}{35}\right) \frac{f_2 + f^2}{f^2 + f_2^2} e^{-z/6} \\ & + 0.00049 f^2 e^{-(T/27+z/17)}, \end{aligned} \quad (4.2)$$

$$f_1 = 0.78 \left(\frac{S}{35}\right)^{1/2} e^{T/26}, \quad (4.3)$$

and

$$f_2 = 42 e^{T/17}, \quad (4.4)$$

where  $z$  is the distance between the transducer and seafloor in km ( $z = r/1000$ ),  $f$  is the sonar frequency in kHz,  $T$  is the temperature in Celsius (assumed to be 4°C in these calculations),  $S$  is salinity (assumed to be 35 ppt), and  $pH$  was assumed to be 8. This attenuation term is then converted into units of dB/m for range correction and effective backscatter coefficient calculations.

#### 4.5.1.2 Stacking Backscatter Profiles Together

Data from the extracted portion of the downcast were stacked together to remove noise in individual backscatter profiles and decrease some variability in consecutive profiles. While some loss within the water column can be estimated using Equations 4.1 and 4.2, the area of the insonified region of the seafloor can affect the scattered acoustic signal

and is a function of the range above the seafloor which cannot be easily removed through calculated parameters. Furthermore, other obstacles such as fish, zooplankton, bubbles, and other heterogeneities can be different from ping to ping and can affect the backscatter amplitude of the seafloor return (*Bjørnø et al., 2017*).

Before stacking profiles together, the data from each transect were then reformatted into a matrix such that the maximum backscatter of the seafloor return was lined up for each stack of profiles (examples of this are shown in Figures 4.14 and 4.15). This process was called range normalization. A range of 50 m was chosen for visualization of these data, however, the averaged distances from the seafloor of these downcasts are approximately 76 m. Examples of isolated seafloor backscatter returns from downcasts at their original depth bins and after range-normalization are shown in Figure 4.5.

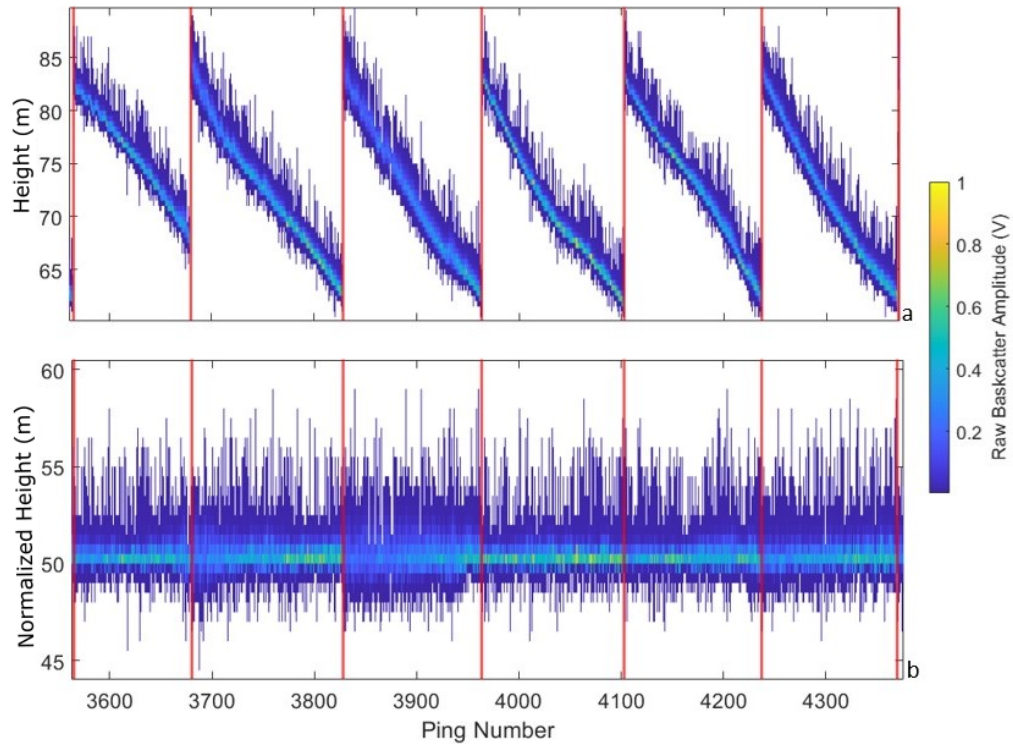


Figure 4.5: Raw seafloor return backscatter voltage amplitudes are shown for the extracted portions of the glider downcasts which show (a) the seafloor returns at their original depth bins and (b) returns after range-normalization. Red vertical lines on each plot indicate the separation between each glider downcast.

In this study, profiles were stacked by averaging backscatter amplitudes from each range-normalized seafloor return feature in each extracted downcast (i.e. in the form of Figure 4.5b). Because of variations in bathymetry, these extracted downcasts vary in the total number of pings, and therefore the mean depth of each downcast is also varied. The average depth of each downcast was calculated as an average of the distance between the transducer and seafloor return peak for each profile in the extracted downcast (approximately 76m). The average spatial resolution of the data after averaging was 2400 m<sup>2</sup> for mission 38 and 2600 m<sup>2</sup> for mission 51.

### **4.5.1.3 Seafloor Segmentation**

After the seafloor return backscatter data were corrected for attenuation and spherical spreading and stacked over the downcast, data were separated into individual transects, ignoring turns where possible. The backscatter data were then re-scaled to be between 0-1. Using the range-normalized backscatter returns, pairwise Euclidean distances between each bottom return were calculated. The data were then scaled using the non-metric multidimensional scaling ordination in MATLAB, *mdscale*, which creates a configuration of points in 3 dimensions whose inter-point distances are similar to those in the input distance (or dissimilarity) matrix, which enables clustering. These scaled data were then used in the density-based clustering algorithm, *dbscan*. This algorithm determines the ideal number of clusters based on a set 2-dimensional Euclidean distance away from a number of core points and will leave observations unassigned to any cluster if they fall too far from these core values. The number of points required for a cluster to be considered separate was set to 5, and the ideal 2D Euclidean distance between clusters differed between transects. After clusters were defined by *dbscan*, statistics including mean, maximum, standard deviation, skewness, kurtosis, return width, peak prominence, and area under the curve of the seafloor return were calculated for each assigned cluster in each transect and plotted to compare against each other. Clusters with similar median values ( $\pm 0.03$  dB) calculated from the maximum backscatter of seafloor returns were reassigned or combined based on their 2D Euclidean distances from other clusters. Maximum backscatter was chosen to determine whether a cluster should be reassigned or combined because this parameter showed the most differentiation between clusters.

## **4.5.2 Impedance and Effective backscattering Coefficient Calculations**

### **4.5.2.1 Acoustic Theory: Scattering from the Seabed**

Active sonar ping frequencies can range from infrasound (on the order of 20Hz) to megahertz, though "high-frequency" generally indicates a range of tens of kHz to MHz

values (*Jackson and Richardson, 2006*). Acoustic absorption in seawater and in seafloor sediments increases with frequency, allowing low frequency (<1 kHz) acoustic waves to propagate with very little energy loss (<0.1 dB/km) over long distances and penetrate up to hundreds of meters into the seafloor sediment. At higher frequencies (kHz to MHz), sound can penetrate into the seabed on the order of meters at the lower-frequency end and centimeters at the higher-frequency end (*Jackson and Richardson, 2006*). These high-frequency sound waves also suffer greater energy loss to chemical processes and viscosity in seawater, limiting its propagation range (*Fisher and Simmons, 1977; Jackson and Richardson, 2006*). Acoustic waves incident upon the seafloor or targets upon the seafloor (including vegetation, organisms, and inorganic objects) are either scattered back to the transducer or away in a different direction (*Jackson and Richardson, 2006; Lurton, 2002; Bjørnø et al., 2017*). Scattering of acoustic energy off of the seafloor is caused by variations in the surface roughness, bulk sediment properties (i.e. density and porosity), or materials that have different acoustic properties from the bulk sediment such as bubbles or organic material. In this thesis, the roughness of a surface is assumed to be enough that all acoustic waves incident on the seafloor are scattered rather than perfectly reflected. If the acoustic energy returns to the transmission source, this is referred to as "monostatic scattering", or backscattering.

Seafloor scattering can be quantified using the metric of scattered strength (sometimes called seafloor or bottom scattering strength as opposed to volume scattering, which indicates scattering within the water column or within the sediment) (*Jackson and Richardson, 2006*). Scattering strength is dependent on the acoustic frequency, the scattering and incident angles, the properties of the water at the sediment-water interface, and the sediment itself such as density, grain size, and porosity. Figure 4.6 from *Jackson and Richardson (2006)* shows the coordinate system, angles, and variables associated with the scattering discussed in this section. Half the source beam width is defined as  $\phi_0$ ,  $\theta$  indicates azimuthal angle,  $\beta_i$  and  $\beta_s$  are the angle of incidence and the scattered angle respectively. In the

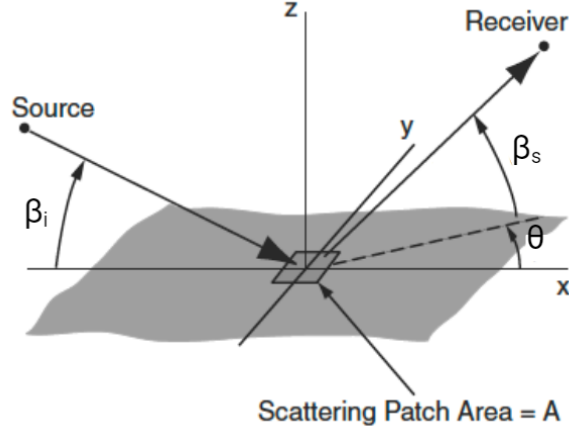


Figure 4.6: Variables and coordinates associated with scattering and reflection, adapted from *Jackson and Richardson (2006)*.

case of backscattering,  $\beta_i = \beta_s$ , and are related to  $\phi$ , and  $\theta = \pi$  (*Jackson and Richardson, 2006*).

Based on the situation outlined in Figure 4.6, an acoustic pressure wave incident on the seafloor can be defined as

$$P_i = p_* \frac{r_*}{r} D(\phi) e^{i(kr - \omega t + k\delta) - \alpha_0 r}, \quad (4.5)$$

where  $r$  is the slant range from the transducer to the seafloor,  $k$  is the wavenumber,  $\omega$  is the frequency,  $t$  is time, and  $\delta$  is a small change in horizontal range based on the angle of incidence. The variable  $p_*$  is the pressure of the acoustic wave at some reference distance ( $r_*$ ) from the transducer, and  $D$  is the transducer directivity with respect to  $\phi$ . The attenuation coefficient,  $\alpha_0$ , here is in the units of nepers per meter (Np/m).

The scattered acoustic pressure is then defined as

$$P_s = P_i \frac{\sqrt{\sigma}}{r} D(\phi) e^{i(kr + \omega t + k\delta) - \alpha_0 r}, \quad (4.6)$$

where  $\sigma$  is the scattering cross-section. Substituting Equation 4.5 in Equation 4.6 gives

$$P_s = p_* \frac{r_* \sqrt{\sigma}}{r^2} D^2(\phi) e^{2i(kr+k\delta)-2\alpha_0 r}. \quad (4.7)$$

For  $N$  scatterers with random  $\delta$  values, the scattered intensity of the acoustic wave is

$$dI_s = |P_s|^2 n dA, \quad (4.8)$$

where  $n$  is the number of scatterers and  $dA$  is the surface area. Substituting Equation 4.7, Equation 4.8 becomes

$$dI_s = I_0 \frac{r_*^2 \Gamma}{r^4} D^4(\phi) e^{-4\alpha_0 r} dA, \quad (4.9)$$

where  $I_0 = |p_*|^2$  is the source level intensity at reference range  $r_*$ . The parameter  $\Gamma = \sigma n$  is the effective backscattering coefficient for the surface and is a measure of the energy scattered.

In this thesis, this effective backscattering coefficient is used to differentiate regions on the shelf seafloor with different properties based on backscattered data from a downward-facing single-beam echo sounder. The geometry for this scenario is shown in Figure 4.7.

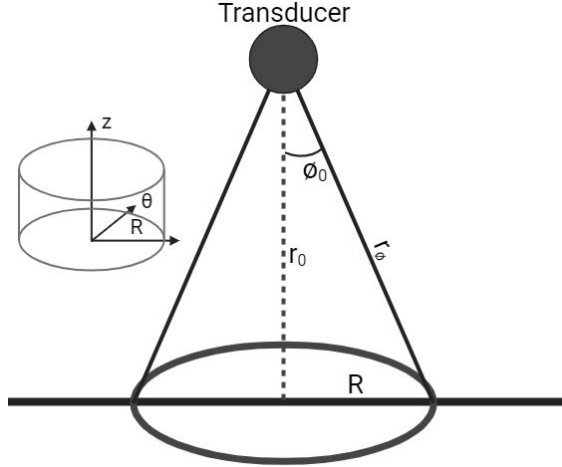


Figure 4.7: Geometry relevant to the derivation of backscattered energy used in this thesis. The transducer is indicated as downward facing and  $r$  is the slant range from the transducer to the seafloor,  $r_0$  is the height of the transducer above the seafloor,  $\phi_0$  is the half beam width.  $R$  is the radius of the surface area insonified by the sonar.

In the geometry indicated in Figure 4.7, the scattered intensity from Equation 4.9 is given by

$$I_s = I_0 r_*^2 \Gamma \int_0^{2\pi} \int_0^{R_0} \frac{D^4(\phi) e^{-4\alpha_0 r}}{r^4} R dR d\theta, \quad (4.10)$$

where  $\Gamma$  (and therefore  $\sigma$ ) is assumed to neither be a function of  $\phi$  nor  $\theta$ .

Using the cylindrical symmetry of the geometry, the integral with respect to  $\theta$  is equal to  $2\pi$ , and Equation 4.10 becomes

$$I_s = 2\pi I_0 r_*^2 \Gamma \int_0^{R_0} \frac{D^4(\phi) e^{-4\alpha_0 r}}{r^4} R dR. \quad (4.11)$$

Based on the geometry of this scenario,  $dR = r_0 d\phi$ , and both  $R$  and  $r$  can be related to  $r_0$  via the equations

$$R = r \sin \phi, \quad (4.12)$$

and

$$r = \frac{r_0}{\cos \phi}. \quad (4.13)$$

Therefore, Equation 4.11 becomes

$$I_s = 2\pi I_0 r_*^2 \Gamma e^{-4\alpha_0 r_0} \int_0^{\phi_0} \frac{D^4(\phi) e^{-4\alpha_0 r_0 (1/\cos \phi - 1)} r_0^2 \sin \phi}{(r_0/\cos \phi)^4 \cos \phi} d\phi. \quad (4.14)$$

For a narrow beam width, which is the case in this thesis,  $1/\cos \phi - 1 \ll 1$ . The reference distance used for all sonar instruments in this thesis is  $r_* = 1$  m. The directivity ( $D$ ) is assumed to be equal to 1, meaning that theinsonified area of the seafloor is in the shape of a circle. Thus, Equation 4.14 becomes

$$I_s = \frac{2\pi I_0 \Gamma e^{-4\alpha_0 r_0}}{r_0^2} \int_0^{\phi_0} \cos^3 \phi \sin \phi d\phi. \quad (4.15)$$

After solving the integral, Equation 4.15 becomes

$$I_s = \frac{\pi I_0 \Gamma e^{-4\alpha_0 r_0} (1 - \cos^4 \phi_0)}{2 r_0^2}. \quad (4.16)$$

An active sonar equation can be derived by taking  $10 \log_{10}$  of Equation 4.16.

$$\begin{aligned} 10 \log_{10}(I_s) = 10 \log_{10}\left(\frac{\pi}{2}(1 - \cos^4 \phi_0)\right) + 10 \log_{10}(I_0) + 10 \log_{10}(\Gamma) \\ - 10 \log_{10}(e^{4\alpha_0 r_0}) - 10 \log_{10}(r_0^2). \end{aligned} \quad (4.17)$$

The attenuation coefficient,  $\alpha_0$  in units of Np/m can be put into the units of dB/m using the relationship,

$$1\text{Np} = 20/\ln(10)\text{dB}, \quad (4.18)$$

which would make the attenuation term in Equation 4.17 equal to

$$2\alpha_0 r_0 \log_{10}(e). \quad (4.19)$$

Equation 4.17 can be put into the terminology frequently used for sonar equations via

$$20 \log_{10}(P_s) = 10 \log_{10}\left(\frac{\pi}{2}(1 - \cos^4 \phi_0)\right) + SL + BS - 20 \log_{10}(r_0) - 2\alpha_0 r_0 \log_{10}(e), \quad (4.20)$$

where  $SL$  is the source level intensity in dB and  $BS$  is the backscattering strength equal to  $10 \log_{10}(\Gamma)$ . The voltage output from the receiver ( $V$ ) can be related to the received pressure amplitude ( $P_s$ ) using the relationship from *Jackson and Richardson (2006)*

$$RS = 20 \log_{10} \frac{|V|}{|P|}, \quad (4.21)$$

where  $RS$  is the receiver sensitivity of the transducer. Equation 4.20 then becomes

$$20 \log_{10} |V| - RS = SL + BS - 20 \log_{10}(r_0) - 2\alpha_0 r_0 \log_{10}(e) + 10 \log_{10}\left(\frac{\pi}{2}\right) + 10 \log_{10}(1 - \cos^4 \phi_0). \quad (4.22)$$

More terms (i.e. gain, calibration value, noise level) can be added or subtracted from Equation 4.22 based on the specifications of the transducer and the demands of the experiment. In this thesis, the effective backscattering coefficient ( $\Gamma$ ) from single-beam sonar data is used as a proxy to differentiate between surficial sediment types at long ranges (i.e. >50 m between seafloor and transducer).

#### 4.5.2.2 Effective backscattering Coefficients

For all the isolated seafloor returns from missions 38 and 51, the effective backscattering coefficients ( $\Gamma$ ) were calculated from raw bottom backscatter voltage amplitudes by

isolating the backscattering strength parameter ( $BS$ ) from Equation 4.22

$$BS = RL - RS + 20 \log_{10}(r_0) + 2\alpha r_0 - SL - 10 \log_{10}\left(\frac{\pi}{2}\right) - 10 \log_{10}(1 - \cos^4 \phi_0) - G + CC, \quad (4.23)$$

where  $RL = 20 \log_{10} |V|$  is the voltage amplitude from the backscatter returns in dB,  $RS$  is the receiver sensitivity defined by the manufacturer as  $-180$  dB re 1 Volt/ $\mu$ Pa,  $SL$  is the source level, given by the sonar manufacturer as 210 dB relative to 1  $\mu$ Pa at 1m range,  $\phi_0$  is half the conical beam width of the sonar,  $G$  is the gain applied at the receiver and has an amplitude of 40 dB,  $CC$  is a calibration coefficient calculated by CEOTR and has a magnitude of  $-4$  dB for mission 38 and  $-2$  dB for mission 51. For the calculations in this thesis, the attenuation coefficient  $\alpha$  is calculated using the equations from *Ainslie and McColm* (1998) (i.e. Equation 4.2) in the unit  $dB/m$  and doesn't need to be converted from  $Np/m$  as in Equations 4.20 and 4.22.

The effective backscattering coefficient,  $\Gamma$ , was then calculated using

$$\Gamma = 10^{BS/10}. \quad (4.24)$$

After calculating the effective backscattering coefficients for all isolated glider data pings, profiles for each glider downcast were stacked together using the methods in Section 4.5.1.2.

#### 4.5.2.3 Reflection Coefficient Estimates from Seafloor Datasets

Before estimates for reflection coefficients were calculated for the surficial geology units described by *Philibert et al.* (2022), density and sound speed were estimated using values found in the literature. Table 4.3 shows estimated grain size, density, sound speed, and reflection coefficients for each geological unit within the study site and which sources were used for each estimate. The properties of finer sediments (clay - coarse sand) were estimated using *Hamilton and Bachman* (1982). Coarser sediment properties were

estimated using a combination of *Hamilton and Bachman* (1982), *Bachman* (1989), and *Krapivner* (2009). For some geological units, especially those with larger grain sizes, only one property (i.e. either sound speed, grain size, or density) was able to be estimated from the literature, in which case equations from *Bachman* (1989) were used to relate these properties.

Geological Unit	$M_z$ ( $\phi$ )	$\rho$ (kg/m <sup>3</sup> )	$c_2$ (m/s)	Reflection Coefficient	Citation
Br				1	Jackson and Richardson 2006
PgTsg	-1-0.5	2100-2300	1771-1946	0.4241-0.4970	Bachman 1989
Gd	Variable	1900-2300	1634-1946	0.3474-0.4970	Krapivner 2009; Bachman 1989
LgSLs	3-5	1750-1900	1620-1730	0.3-0.3722	Hamilton and Bachman 1982; Bachman 1989
GMm	7-9	1480-1489	1517-1546	0.1977-0.2097	Hamilton and Bachman 1982
PgMm	7-9	1480-1489	1517-1546	0.1977-0.2097	Hamilton and Bachman 1982

Table 4.3: Estimated density, sound speed, and reflection coefficients for each geological unit described in *Philibert et al.* (2022) along with the literature used for these estimates.

The physical grab sample data from the *USGS* (2014) and the *GSC* (2020) included mean grain size in their analysis. The density and sound speed for grab sample data and geology unit estimations were calculated using the weighted regression equation relating grain size to sound speed ratio from *Bachman* (1989),

$$\frac{c_2}{c_w} = 1.296 - 6.01 \times 10^{-2} M_z + 2.83 \times 10^{-3} M_z^2, \quad (4.25)$$

where  $M_z$  is the mean grain size in phi units ( $\phi$ ),  $c_2$  is the sound speed in the sediment and  $c_w$  is the sound speed of the water. Given the bulk density ( $\rho$ ), sound speed can be calculated using another equation from *Bachman* (1989),

$$\frac{c_2}{c_w} = 1.513 - 8.24 \times 10^{-4} \rho + 3.2249 \times 10^{-7} \rho^2. \quad (4.26)$$

Reflection coefficient estimates for both physical grab samples and surficial geology units were then calculated using the equation

$$RC = \frac{\rho_2 c_2 - \rho_1 c_w}{\rho_2 c_2 + \rho_1 c_w}, \quad (4.27)$$

where  $\rho_1$  is the water density and  $\rho_2$  is the saturated bulk density of the sediment.

## 4.6 Results

### 4.6.1 Seafloor Segmentation

Mission 38 was split into 7 transects, shown in Figure 4.8. Table 4.4 lists the number of originally assigned clusters for each transect. Based on the 2D Euclidean distances between seafloor return maxima, clusters from transects 5-7 were reassigned. Cluster 3 from transect 3 was combined with cluster 1, and cluster 4 from transect 7 was combined with cluster 2. The final cluster assignments are shown in Figure 4.10. Cluster 1 has the highest maximum backscatter (ranging between normalized values of 0.85 and 0.69), followed by clusters 2 (ranging between normalized values of 0.69-0.57) then 3 (ranging between normalized values of 0.57-0.46).

Transect	Number of Assigned Clusters
1	1
2	2
3	3
4	2
5	3
6	3
7	4

Table 4.4: Number of clusters assigned automatically to Mission 38 using a density-based clustering algorithm.

The transects analyzed in mission 51 are shown in Figure 4.9. Table 4.5 displays the number of clusters originally assigned to each transect. Based on Euclidean distances between seafloor return maximums, clusters from transects 1-3, 6, 11, and 14 were reassigned, and clusters 2 and 1 from transects 1 and 17 were combined. For this glider mission, 2 clusters were determined to be distinct. The final assigned clusters are shown in Figure 4.10. Cluster 1 has higher maximum backscatter (with normalized values between 0.85-0.6) than cluster 2 (ranging between normalized values of 0.6-0.45).

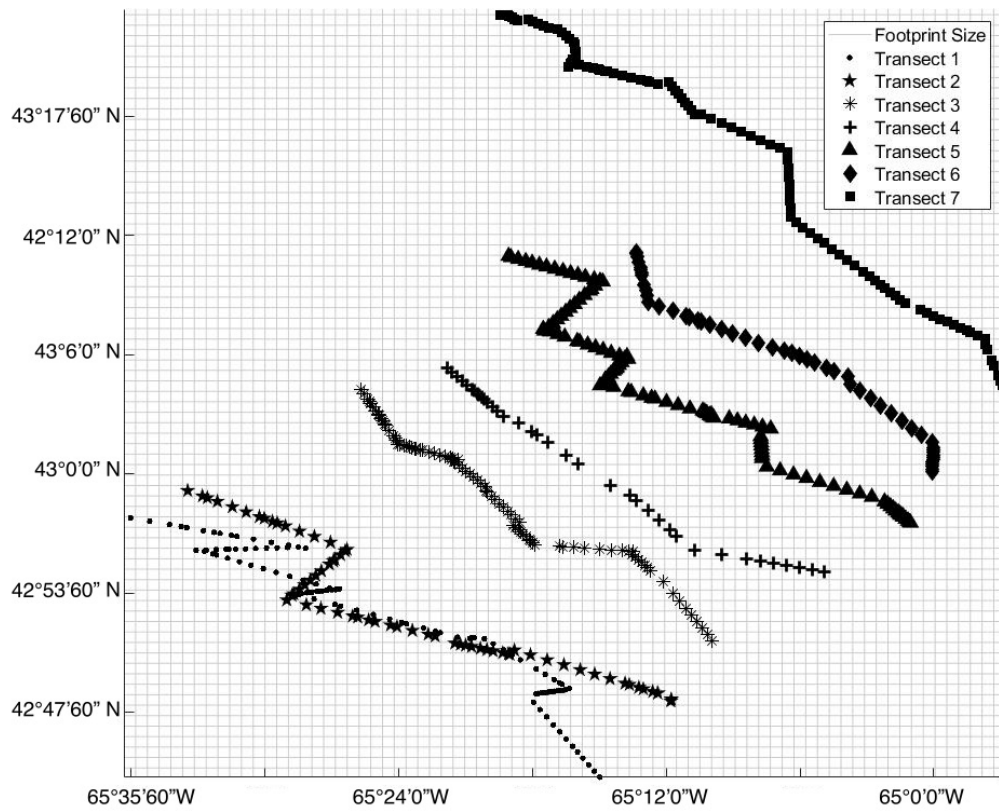


Figure 4.8: Transects 1-7 from Mission 38 plotted on top of a gray grid indicating sonar footprint size (0.0024km<sup>2</sup>).

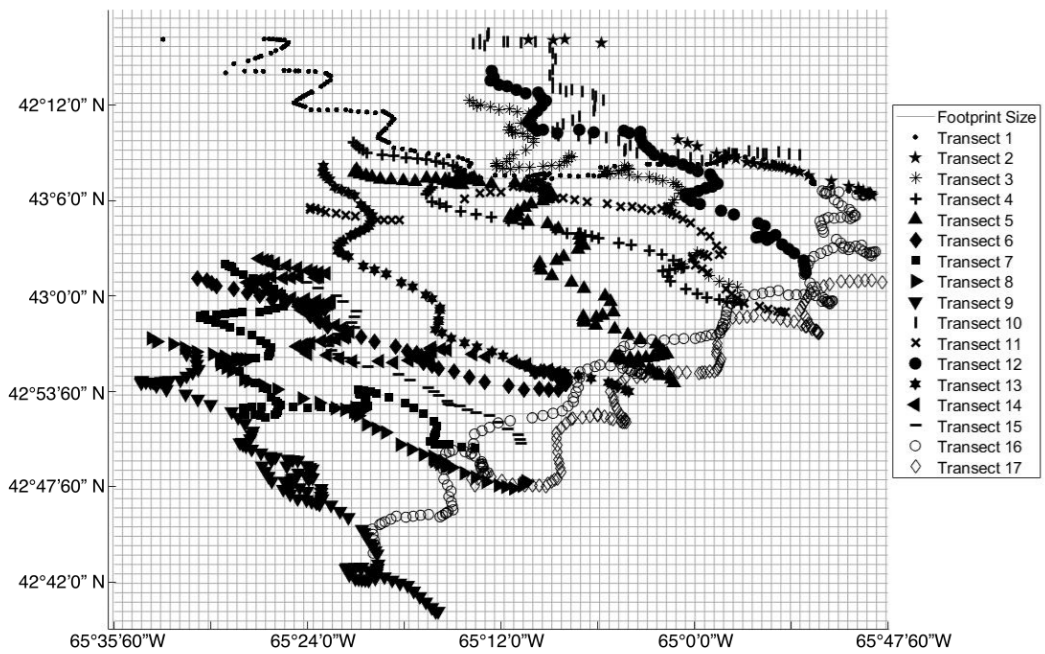


Figure 4.9: Transects 1-17 from Mission 51 plotted on top of a gray grid indicating sonar footprint size (0.0024km<sup>2</sup>). Parallel transects are shown with closed markers, while perpendicular transects are shown with open markers.

Transect	Number of Assigned Clusters
1	3
2	2
3	2
4	2
5	2
6	2
7	2
8	1
9	1
10	2
11	2
12	2
13	2
14	2
15	2
16	2
17	2

Table 4.5: Number of clusters assigned automatically for Mission 51 using a density-based clustering algorithm.

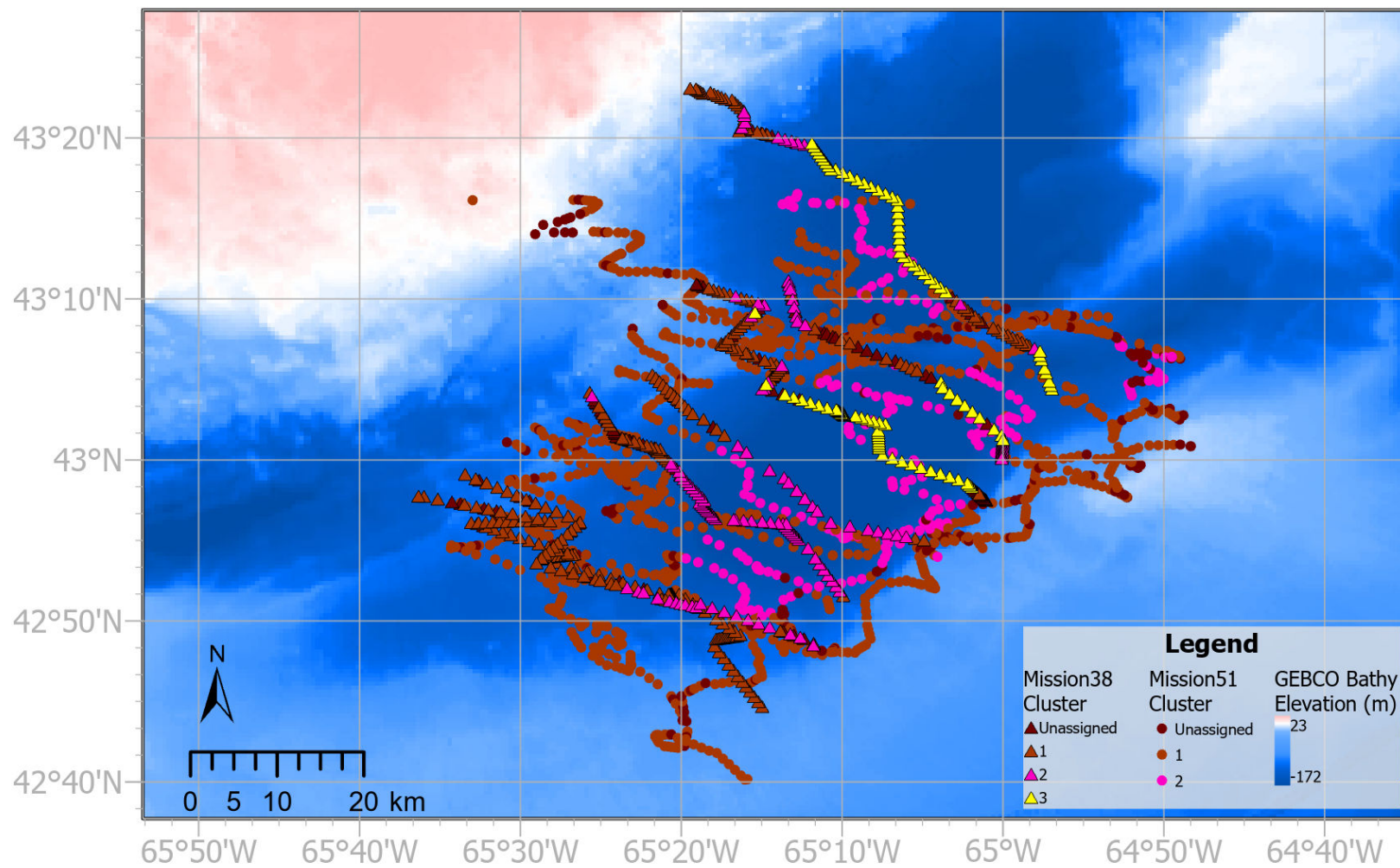


Figure 4.10: Segmentation results of both missions 38 and 51 are plotted together against GEBCO bathymetry. Mission 38 clusters are indicated by triangles, mission 51 clusters are indicated with circles.

Segmentation results from missions 38 and 51 are mapped together in Figure 4.10. Clusters 2 and 3 from mission 38 often overlap with cluster 2 from mission 51. One notable exception is around 43.1-43.2°N and -65.3°W, where clusters 2 and 3 were assigned for mission 38 and cluster 1 for mission 51. Cluster 1 from both glider missions overlap for most transects, except for transects 5, 6, and 12 from mission 51, which were segmented into cluster 1 only and disagree with segmentation results from mission 38.

The final clusters for each mission transect were examined to determine whether they needed to be reassigned or combined based on the 2D Euclidean distances between medians. Figures 4.11 and 4.12 show box and whisker plots as a way to visualize this. These two plots show the final assigned clusters for all transects in missions 38 and 51 respectively. While outliers, and even sometimes whiskers and boxes, cross the line determined to be the range of each cluster, the median value of the cluster ultimately determines where each group will be re-assigned. After the clusters are reassigned, the surficial sediment can be classified based on the distribution of these statistics for each cluster.

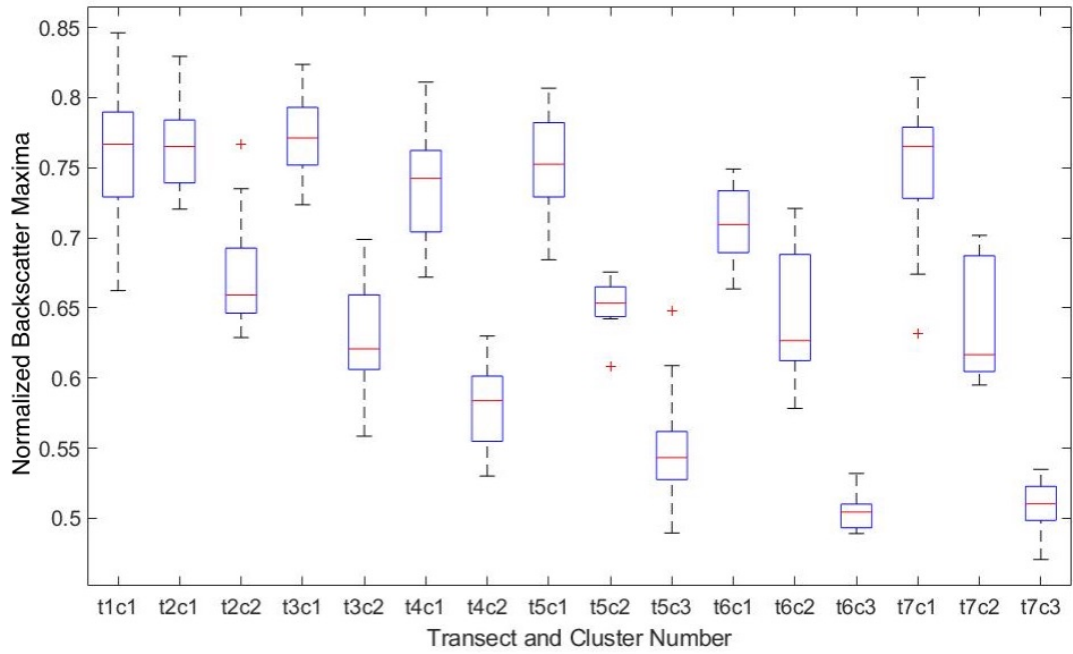


Figure 4.11: Box and whiskers plots for each final cluster assigned for Mission 38. The x-axis indicates the transect (t) and cluster (c) and the y-axis indicates the maximum backscatter, normalized between 0 and 1. The medians of each cluster are indicated with red horizontal lines. Outliers are indicated by a red cross. Based on the distributions of these maxima, the type of surficial sediment can be classified.

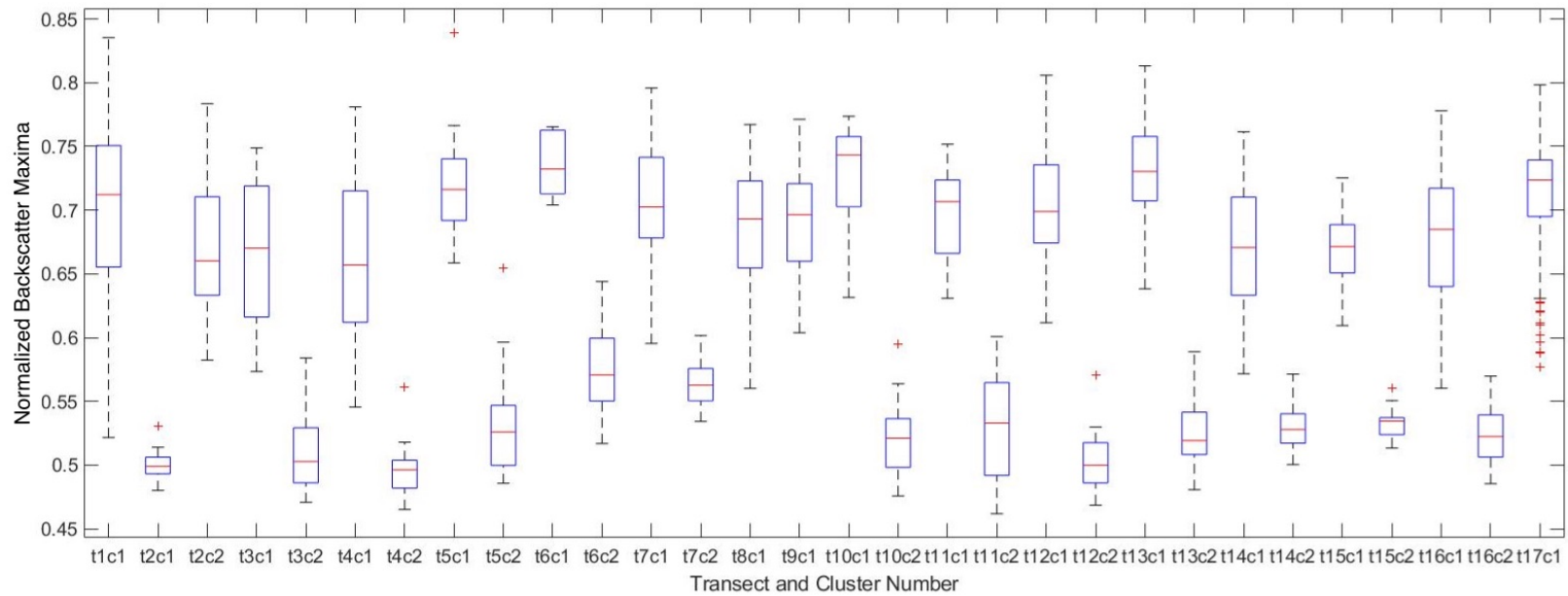


Figure 4.12: Box and whiskers plots for each final cluster assigned for Mission 51. The x-axis indicates the transect (t) and cluster (c) and the y-axis indicates the maximum backscatter, normalized between 0 and 1. The medians of each cluster are indicated with red horizontal lines. Outliers are indicated by a red cross. Based on the distributions of these maxima, the type of surficial sediment can be classified.

#### 4.6.1.1 Environmental Data Comparison to Clusters

Bathymetry can be compared to the segmentation results in Figures 4.10 for missions 38 and 51. With the exceptions of transects on the north/northeastern region of these glider paths (i.e. transects 6 and 7 for mission 38 and transects 2,3,10, and 11 for mission 51), most transects of these missions occur over the southern portion of Roseway Basin, below the ridge feature. Cluster 1 is dominant around most of the study site, however, clusters 2 and 3 for mission 38 and cluster 2 for mission 51 occur in regions where the water is deeper. For mission 38, cluster 3, which has the lowest seafloor backscatter returns, tends to occur in the deepest part of the basins and is surrounded by cluster 2, thus grain size increases sequentially as water depth decreases.

The clusters for missions 38 and 51 are compared to the GSC surficial geology map in Figure 4.13 (*Philibert et al., 2022*). Cluster 3 in mission 38 occurs at sediments PgMm, GMm, and LgSLs. According to the descriptions in *Philibert et al. (2022)*, these substrate classes are the finer-grained sediments, which is in agreement with the cluster with the lowest backscatter amplitude. Cluster 2 is found around this finer-grained sediment as well, specifically GMm and LgSLs, as well as variable or larger-grained sediment such as Gd and PgTsg. Finally, Cluster 1 is found mostly around denser and larger-grained sediments (i.e. Gd, Br, PgTsg), though this cluster is also found around LgSLs, particularly at the edges of the basins and dominates the first two transects of this mission. Cluster 2 from mission 51 is found around the finer-grained sediments of PgMm, GMm, and LgSLs, which is in agreement with the lower backscatter amplitude of this cluster. Cluster 1 from this mission is found mostly around the denser, larger-grained sediments in the region, PgTsg, Gd, and Br.

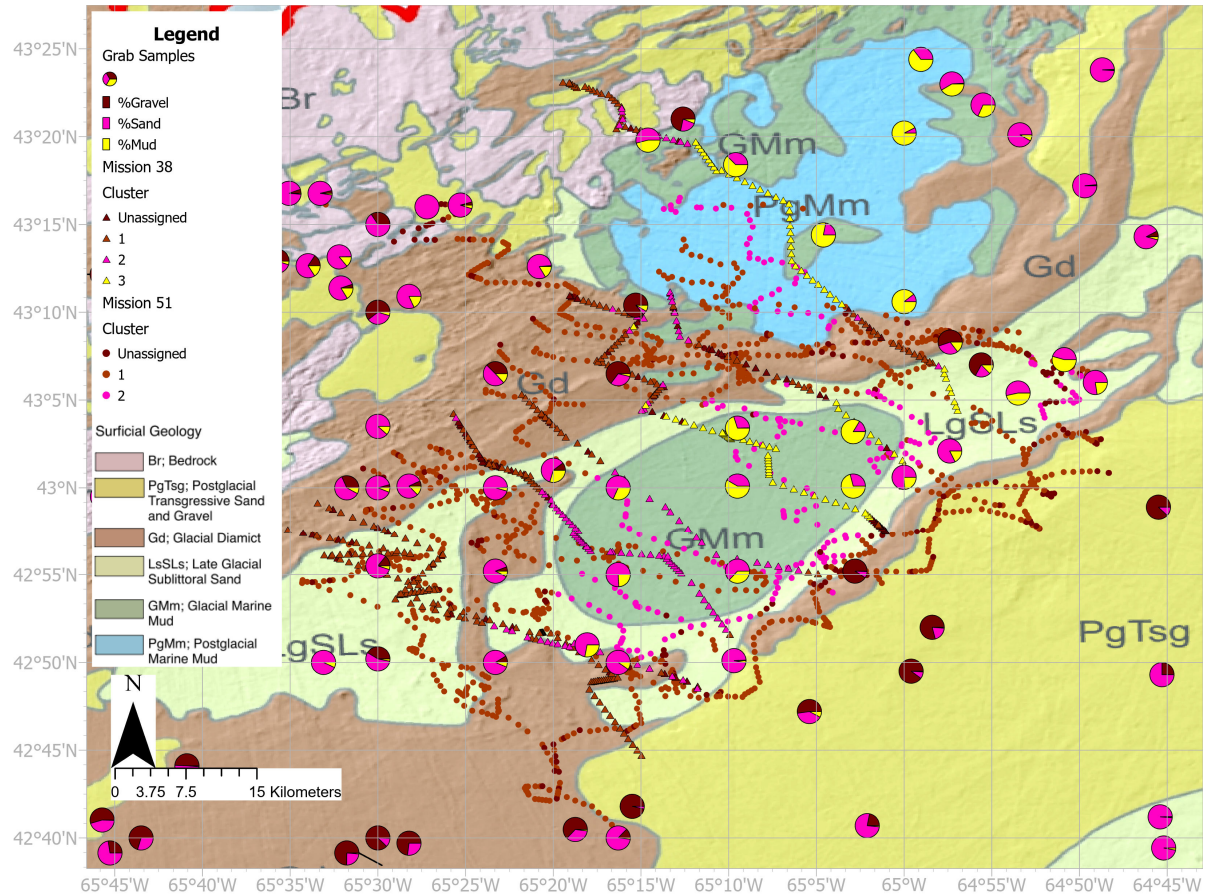


Figure 4.13: Surficial geology map from *Philibert et al. (2022)* and physical grab sample grain sizes (*GSC, 2020; USGS, 2014*) compared to cluster results from missions 38 and 51. Mission 38 clusters are indicated with triangle markers while mission 51 clusters are indicated with circle markers.

Some anomalies occur in the lower part of both the south/southwestern lobe of Roseway Basin in transects 6 and 14 as well as the north/northeastern basin in transects 3 and 12 where the segmentation results yielded entire transects of cluster 1 where cluster 2 should be present. These clusters are at odds with the reflection coefficients derived from the backscatter of this mission, which shows low-to-mid range coefficients at all of these transects. When compared to grab samples, sand is dominant over mud and gravel in most of the lower lobe of Roseway Basin, which does agree with the mission 51 clusters (Figures 4.2, 4.10). Figure 4.15b,d show the normalized backscatter of transects 6 and 14 for the southern basin. The glider was moving in the same direction (in a western direction) for both transects, so the discrepancies would have occurred at the beginning of these transects. The backscatter shows low maximum returns for both transects at low along-track distances, which both increase as the gliders cross the southern lobe of Roseway Basin. Figures 4.15a,c show the normalized backscatter of transects 3 and 12 for the southern basin. The glider was moving in the same direction (in an eastern direction) for both transects, so the discrepancies would have occurred at the beginning of these transects. The backscatter shows low maximum returns for transect 3 and mid-range maximum backscatter returns for transect 12 at low along-track distances, which both fluctuate as the gliders cross the southern lobe of Roseway Basin.

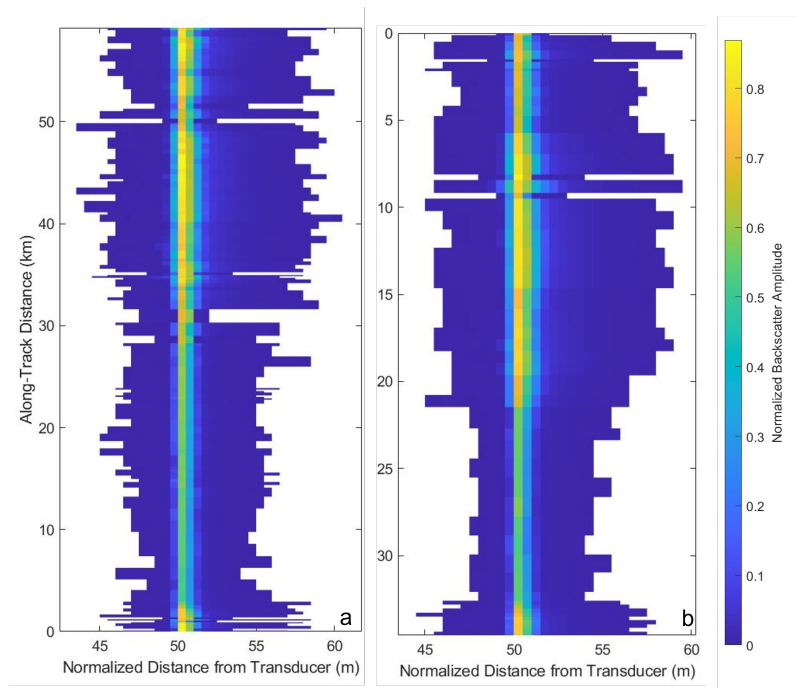


Figure 4.14: Normalized seafloor returns for mission 38 (a) transect 5 and (b) transect 6. The returns are normalized such that the backscatter maximum occurs at the same point along the x-axis.

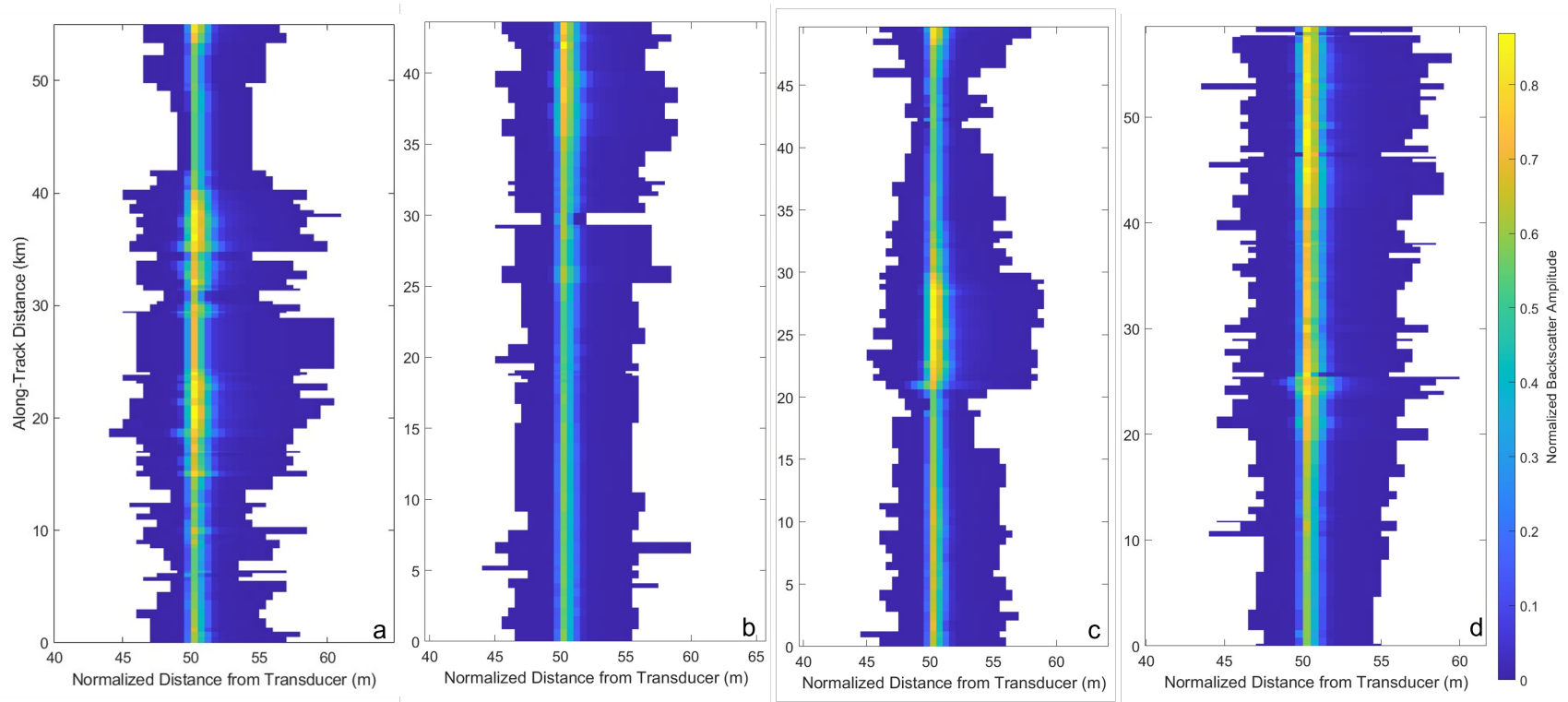


Figure 4.15: Normalized seafloor returns for mission 51 (a) transect 3, (b) transect 6, (c) transect 12, and (d) transect 14. The returns are normalized such that the backscatter maximum occurs at the same point along the x-axis.

## **4.6.2 Effective Backscattering and Reflection Coefficients**

The effective backscattering coefficients were calculated on seafloor return backscatter maximums averaged over glider downcasts (shown for both glider missions in Figures 4.16 and 4.17). For mission 38, the range in calculated effective backscattering coefficients is 0 – 0.2. For mission 51, the range in calculated effective backscattering coefficients is 0 – 0.02. Though the range of coefficients differs between both the averaged and non-averaged data as well as in between missions, the trends are similar. The regions of smaller coefficients correspond with deeper water, while larger coefficients are found on slopes and shallower water in the area.

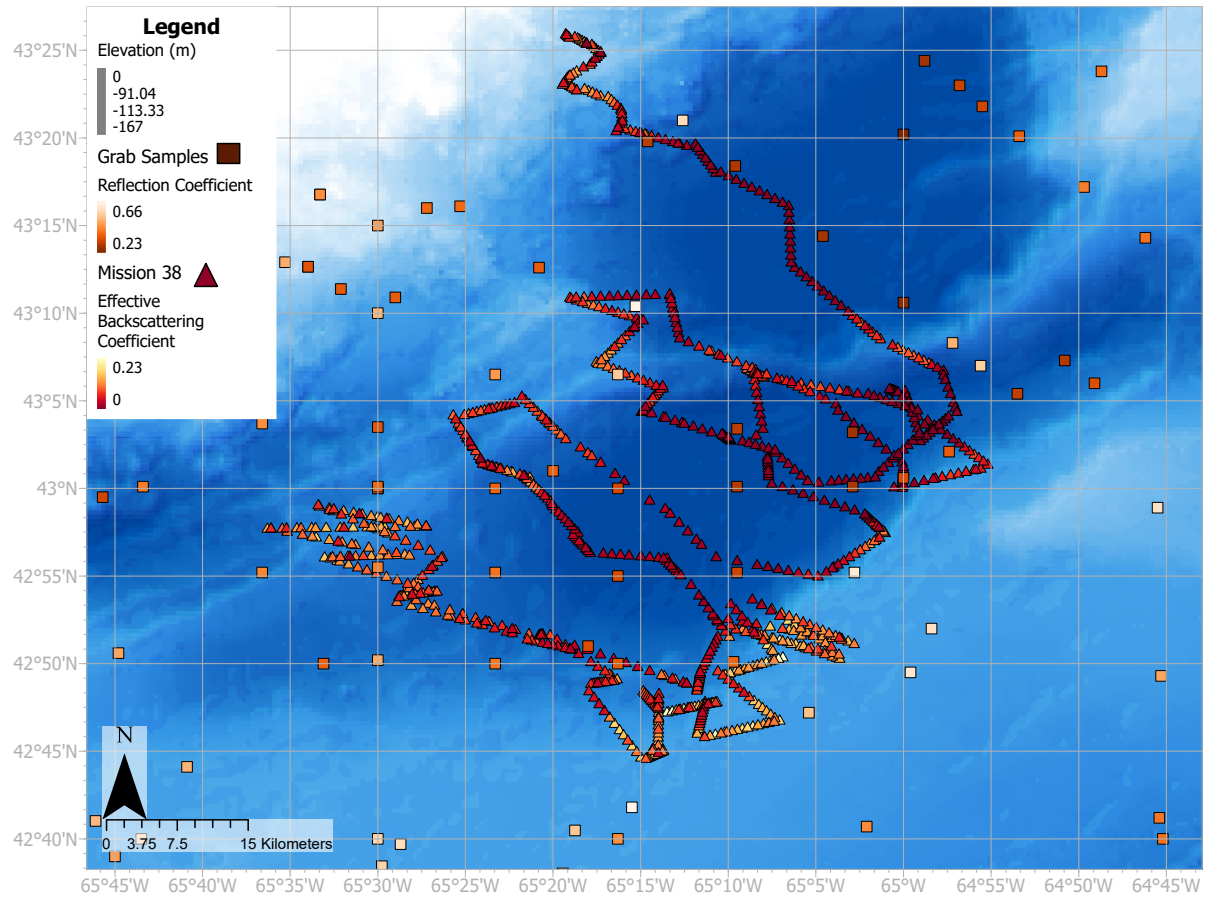


Figure 4.16: effective backscattering coefficients for Mission 38 using seafloor return backscatter averaged over glider downcast. Values are mapped on top of GEBCO bathymetry.

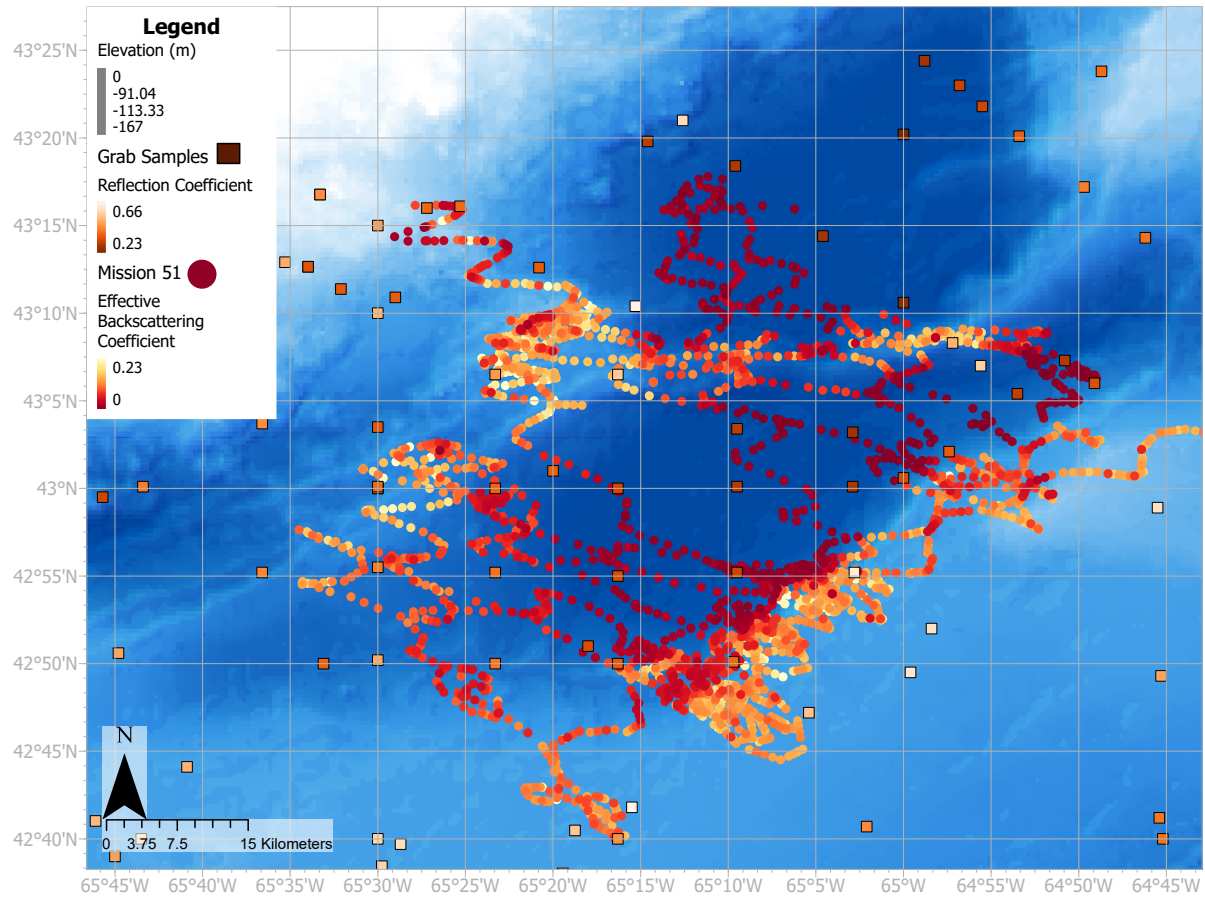


Figure 4.17: effective backscattering coefficients for Mission 51 using seafloor return backscatter averaged over glider downcast. Values are mapped on top of GEBCO bathymetry.

The reflection coefficient estimates for the surficial geology units are shown in Figure 4.18. Br is assumed to be a hard surface with a reflection coefficient of 1. PgTsg ranges from sand to gravel and has an estimated  $RC$  range of 0.42–0.49. Gd is described as dense or stiff diamict and has an estimated  $RC$  range of 0.34–0.49. The unit LgSLs contains mainly mud and sand with little gravel and has an estimated  $RC$  range of 0.3–0.37. Units GMm and PGMm are described as clayey silt or silty clay and have estimated  $RC$  ranges of 0.19–0.2. However, GMm is also described as containing scattered clasts which would locally raise the reflection coefficient in this sediment. Thus in Figure 4.18, a darker color for PgMm indicates lower reflection coefficient estimates.

Figure 4.18 shows reflection coefficients calculated using mean grain size from grab samples collected by the USGS and the GSC indicated with square markers. These reflection coefficient values range from 0.23–0.66. Lower reflection coefficient values are typically in deeper water, whereas higher values are typically found on and near banks, and close to the ridge-like feature that separates the two lobes of Roseway Basin.

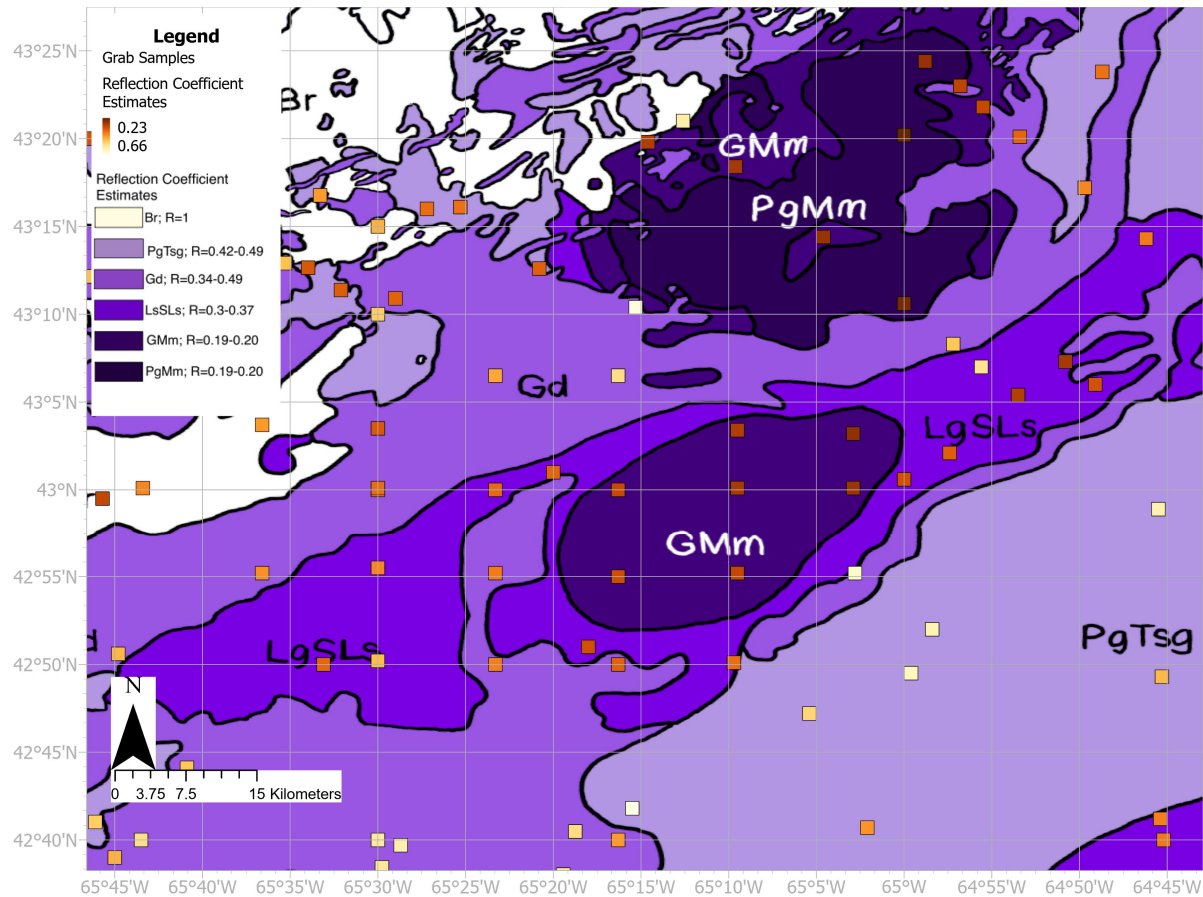


Figure 4.18: Calculated reflection coefficients for the physical grab samples combined from the USGS and the GSC data are plotted on top of the reflection coefficient estimates of the surficial geology map from *Philibert et al. (2022)*. Lighter colors indicate larger reflection coefficients whereas darker colors indicate lower reflection coefficients. Square markers indicate the location of the grab samples.

#### 4.6.2.1 Coefficient Comparisons

The grab sample reflection coefficients are compared to the surficial geology reflection coefficient estimates in Figure 4.18 (*GSC*, 2020; *USGS*, 2014; *Philibert et al.*, 2022). In the deepest parts of Roseway Basin, the surficial geology and grab sample reflection coefficient estimates are in agreement. Low reflection coefficients are found in basins and higher reflection coefficients are typically found in regions where the surficial geology maps indicate larger grain sizes or bedrock. Some discrepancies occur at the border between Gd and LgSLs between 43°5' N and 43°10' N, 65°W and 64°55' W, where two high values of grab sample reflection coefficient (0.54 in the LgSLs region and 0.5 in the Gd region), and a slight increase in grab sample reflection coefficient values in the west/southwest region of GMm in the lower lobe of Roseway Basin. For both of these discrepancies, the calculated effective backscattering coefficients for the single-beam echo sounder data are more similar to the grab sample reflection coefficients than the surficial geology coefficient estimates.

The effective backscattering coefficients calculated for missions 38 and 51 are compared to reflection coefficients calculated using the mean grain size of physical grab samples in Figure 4.19 (*USGS*, 2014; *GSC*, 2020). Although the amplitudes between glider-derived effective backscattering coefficients and those calculated from sediment mean grain sizes differ, the trends are the same. Smaller values are found in basins, larger coefficients are found on banks and the ridge between the two lobes of Roseway Basin, and intermediary values are found on slopes and in regions where the surficial geology may be transitioning from one type to another.

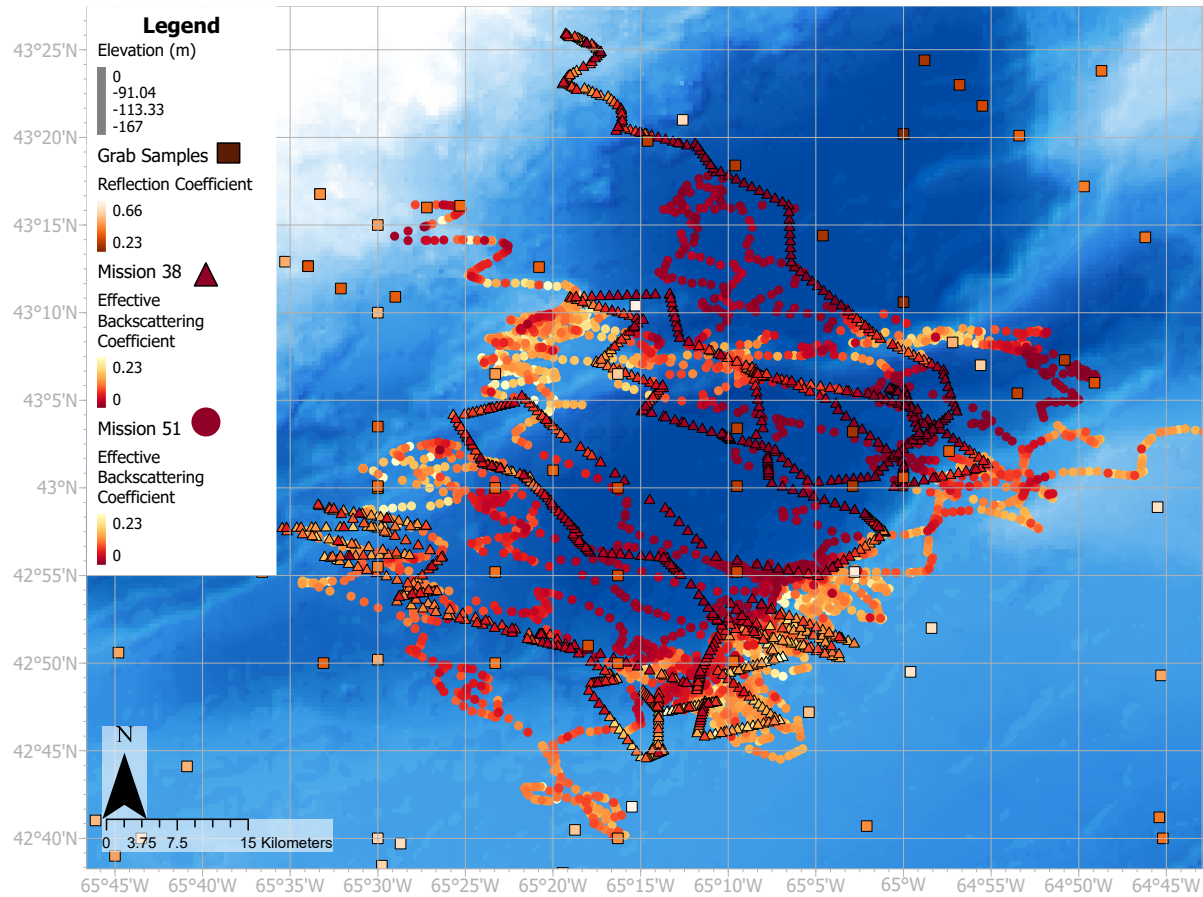


Figure 4.19: Calculated effective backscattering coefficients for missions 38 and 51 compared to reflection coefficients calculated for physical grab samples. Lighter colors indicate larger coefficient values whereas darker colors indicate lower coefficient values. Grab samples are shown as square markers, mission 38 data are shown as triangle markers, and mission 51 data are shown as circle markers. Data are plotted on top of GEBCO 2022 DEM.

The effective backscattering coefficients calculated on the single-beam backscatter data are compared to the reflection coefficient estimates for the GSC surficial geology map in Figure 4.20. In most regions, the calculated effective backscattering coefficients agree with reflection coefficient estimates based on the literature. In mission 38, the middle of transect 3 and some of transect 4 pass over glacial marine mud, which is described as clayey-silt or silty clay with scattered clasts, which is estimated to have a small reflection coefficient because of the fine sediment grain size. However, the calculated effective backscattering coefficients for these transects fall in the middle of the range of values for this mission. Transect 7 exhibits some of the lowest effective backscattering coefficient values around the LgSLs sediment which, while being fine-grained, is described as "muddy sand or silt with little gravel" in *Philibert et al.* (2022). For mission 51, lower calculated effective backscattering coefficients occur in regions with lower estimated reflection coefficients (PgMm, GMm, LgSLs), whereas higher effective backscattering coefficients occur in regions with higher reflection coefficient estimates (Gd, PgTsg, Br).

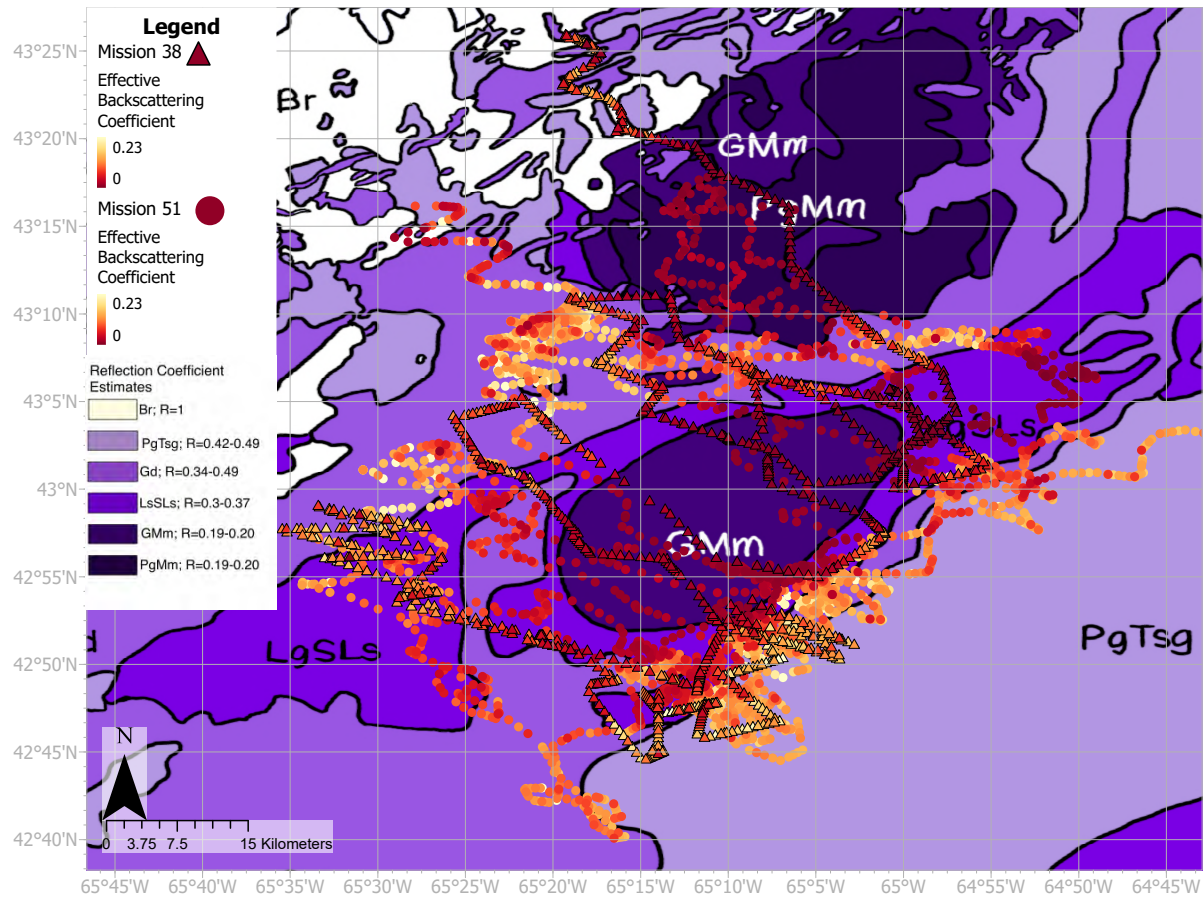


Figure 4.20: Calculated effective backscattering coefficients for missions 38 and 51 plotted on top of the calculated reflection coefficient estimates of the surficial geology map from *Philibert et al. (2022)*. Lighter colors indicate larger coefficients whereas darker colors indicate lower coefficients. Mission 38 is indicated by triangle markers and 51 is indicated by circle markers.

## **4.7 Discussion**

### **4.7.1 Environmental Seafloor Data Sets**

The bathymetry and geomorphology of the continental shelf can be used as an aid to estimate seafloor sediment types along with backscatter returns. Typically, softer sediments can be found in basins whereas coarser or mixed sediments might occur on higher, flat regions of the shelf (*Jolliffe, 1978*). This distribution is due to the amount of energy needed to keep sediments of different grain sizes suspended. Coarser sediment requires more energy to become suspended in the water column and thus will fall out first in the direction of flow. Softer, smaller-grained sediments will stay suspended in the water column further downstream. Based on the bathymetry and geomorphology of this study area, the flow of water and sediment would be from shallower areas into the deeper basins, so coarser materials are expected in regions of shallower water, whereas smaller-grained sediments are expected in basins.

On the scales of the basins and banks in this region, sediment grain size and bathymetry are closely linked. Silt and clay are most often found in basins while sand, gravel, and boulders are found on banks. Moraines are found throughout the shelf region, but when exposed, create the ridge-like feature that separates the two deeper regions of Roseway Basin (*Todd, 2016*). Physical grab samples examined in this study show higher percentages of mud found in the deeper regions of the basin, higher percentages of sand on slopes of the basin and on banks, and higher percentages of gravel south of Roseway Basin, in the region stretching from Browns Bank to Baccaro Bank this also agrees with sediment distribution maps in the literature (*Todd et al., 1999; Todd, 2016; Todd and Kostylev, 2011; King, 1970; Piper, 1986, 1991; Vilks and Rashid, 1976*).

### **4.7.2 Seafloor Segmentation**

Estimated seafloor type based on the ranges of backscatter maxima for each cluster are shown in Table 4.6. Based on the maximum backscatter of clusters in Mission 38,

cluster 1 is identified as the coarsest material (when compared to other clusters), and thus could be gravel, mixed sediment, or sand. Clusters 2 and 3 are softer sediment and may be combinations of sand and mud. Based on the backscatter from mission 51, cluster 1 is identified as a coarser sediment (gravel, mixed gravel, and sand) and cluster 2 indicates a softer sediment (mud or sandy mud). Much of mission 51 and mission 38 overlap, thus they should show similar clustering results. The difference in the number of clusters between Mission 38 and 51 causes some confusion as much of cluster 3 in mission 38 overlaps with cluster 2 in mission 51 and the maximum backscatter of all clusters is within the same range (i.e. between 0.85 and 0.45 for normalized values, or between 210 and 180 dB). Some differences in the two missions analyzed are simply due to the differences in cluster number between the glider missions. A number of different clustering methods were attempted to segment both mission 38 and 51 into the same number of clusters, including K-means clustering (with and without the use of PCA as a way to reduce dimensionality and enhance extracted features). However, the combination of multi-dimensional scaling for the ordination of the data before using density-based clustering as the method of segmentation produced clusters for both missions which had the least amount of overlap when statistics were plotted. Other differences in clusters between glider missions could be due to the difference in spatial resolution of the data, or due to the different gliders used on missions, though it could have a more complex reason as well. It could be that, while sufficient for one mission (i.e. Mission 38), the attenuation and transmission loss estimates used to correct spherical spreading due to range in the water column were not sufficient for both glider datasets.

In the segmentation results for mission 38, there is a clear grain size gradient from the largest grain size (i.e. larger backscatter amplitude) found surrounding the basins to the smallest grain size (i.e. smallest backscatter amplitude) found in deeper regions of the basins. This agrees with the literature (*Todd et al.*, 1999; *Todd and Kostylev*, 2011; *Todd*, 2016; *Drapeau and King*, 1972; *Piper*, 1991; *Vilks and Rashid*, 1976), the physical grab

Cluster	Sediment Type	Backscatter Range	
		Mission 38	Mission 51
1	Sand/Gravel	0.69-0.85	0.6-0.85
2	Sand/Mud	0.57-0.69	0.45-0.6
3	Mud	0.46-0.57	-

Table 4.6: Suggested sediment types for each cluster for glider Missions 38 and 51 based on the range of backscatter magnitude.

samples (USGS, 2014; GSC, 2020), the surficial sediment map (Philibert *et al.*, 2022), and how the bathymetry suggests sediment transport would occur. The segmentation for mission 51 follows expected trends for the most part. The cluster with the lowest backscatter (cluster 2), was identified in regions where soft sediment is expected (in basins). However, cluster 1 was assigned in many regions where softer sediment is shown in the surficial sediment maps Philibert *et al.* (2022). Interestingly, points assigned to cluster 2 around 43°5' N and 64°50' W occur near a patch of clayey-sandy-silty material according to Drapeau and King (1972) which has been removed in the updated surficial sediment map. The glider seafloor returns could be picking up on changes in sediment in this region that were overlooked in the geology map updates.

There is a region that seems to be miss-classified in mission 38 (43.1-43.2°N and -65.3°W). The segmentation data in this region shows cluster 3 surrounded by cluster 2, indicating a softer sediment gradient, though the bathymetry does not indicate a basin in this area, and literature suggests that recessional moraines may exist in this area (Todd, 2016). The closest grab samples show higher percentages of gravel and sand in this region, and the percent mud is quite low. The surficial sediment map shows intrusions of fine-grained sediment near this area, however, the borders of these sediments may not be realistic (Figure 4.13). This anomaly occurs along transects 5 and 6 of the glider mission. The backscatter maximums for each cluster in each transect can be compared to each other using the boxplots in Figure 4.11. The maximum backscatter distribution for cluster 2 from transect 5 is narrow and falls within the range of cluster 2 from other transects. Therefore

all returns assigned to this cluster are likely due to the seafloor properties. Cluster 2 from transect 6 has a wide maximum backscatter distribution compared to other clusters, with values that could be assigned to either cluster 1 or 2, however, the median value is closest to those in cluster 2. With such a wide distribution, it is possible that some returns classified as cluster 2 may have closer backscatter maximums to those in cluster 1.

Examining the averaged seafloor backscatter returns along the glider path for transects 5 and 6 can give a clearer picture of why certain clusters were misclassified. Figure 4.14 shows the isolated bottom returns from transects 5 and 6 from the southwest of the track to the northeast. In both transects, backscatter returns differ visibly between the assigned clusters in both maximum backscatter and isolated return width. Along these transects, the discrepancy at approximately 50 km in transect 5 and between 0 and 5 km in transect 6. The magnitude of these returns aligns with the approximate magnitude of cluster 2, therefore these returns are indicative of the seafloor properties in this region but could indicate the presence of bedforms rather than a change in sediment. Because Euclidean distances were calculated on these range-corrected bottom returns with no other variables, it's likely that these anomalies have to do with other features of these returns, such as width, slope, or shape. To reconcile why the classes of these transects don't match with the backscatter or effective backscattering coefficient data, it's possible that changes to the processing procedure need to be made for future analysis of these data.

The classifications for both missions analyzed in this survey indicate different seafloor sediment properties at Roseway Basin and the surrounding slopes and banks. The clustering results are consistent with the surficial geology units presented in *Philibert et al. (2022)* and physical grab samples from the *USGS (2014)* and the *GSC (2020)*. Segmentation results from more glider missions in this region could increase the spatial resolution of these classes and perhaps the precision of surficial sediment properties defined. However, the classification of sediment was performed in both of these missions. Due to the categorical nature of the segmentation results and the few cluster assignments, some nuance is lost

when comparing the clusters to existing datasets and to each other.

### **4.7.3 Effective backscattering and Reflection Coefficients**

At normal incidence, reflection coefficients can be used as a metric to determine certain geophysical properties of the seafloor, such as bulk sediment density, based on how much energy is lost (*Jackson and Richardson, 2006*). A reflection coefficient of 1 indicates the incident wave is reflected back completely, while a reflection coefficient near zero indicates very little of the reflected wave is received at the transducer. In terms of absorption in sediment, coarser material would yield reflection coefficients closer to 1, while finer-grained sediment would yield coefficients closer to zero. While not a reflection coefficient, the effective backscattering coefficient calculated from glider backscatter data can be used as a proxy for determining differences in surficial sediment, as this parameter is related to properties such as grain size, seafloor roughness, and density.

Because the single-beam echo sounders equipped on the Slocum gliders for each mission are calibrated, the calculated effective backscattering coefficients can be directly compared to each other (Figure 4.20). The effective backscattering coefficients for each of these missions are lowest in the deeper regions of Roseway Basin and are increased on slopes, banks, and the ridge-like feature between the two parts of the basin. Differences between the two missions occur in the southwestern part of the basin. These discrepancies are not large and could be due to the averaging of downcasts, which smoothed the data and could have skewed some of the maximum backscatter values for downcasts that traveled over different sediment types. The glider-derived effective backscattering coefficients show more spatial agreement than the segmentation results because the quantitative values of effective backscattering coefficients present a more gradual transition between lower and higher values than the categorical clusters. Furthermore, the segmentation results present two distinct clusters for mission 51 and 3 for mission 38, which makes comparisons between the two missions more difficult.

When compared to reflection coefficients calculated from grab samples and estimated

from the surficial geology units, the magnitudes of the glider-derived effective backscattering coefficients are very low, with maxima  $\Gamma \leq 2$  for both glider missions. The equation used for these glider-derived calculations, adjusted from the active sonar equation, is a simple method of accounting for losses and gains of backscatter amplitude. It is possible that terms such as attenuation and transmission loss were underestimated due to the assumption of a homogeneous water column (i.e. constant salinity and temperature). These low effective backscattering coefficient magnitudes were likely caused in part by the simplification of the backscatter strength parameter in the active sonar equation as well. This parameter is based on a number of factors that describe the surface sediment roughness, properties associated with the insonified area of the seafloor, and the heterogeneous sediment properties from which the acoustic wave can scatter (*Jackson and Richardson, 2006; Bjørnø et al., 2017*). Therefore, these values can only be used as a proxy to determine sediment distribution and trends in the distribution of these coefficients can be compared to the seafloor data set reflection coefficients rather than the effective backscattering coefficient values.

The trends in the glider-derived effective backscattering coefficients are in agreement with reflection coefficients calculated using grain size data from grab samples collected by *USGS (2014)* and *GSC (2020)* (Figure 4.19) and with coefficient estimates from surficial geology units (Figure 4.20). As in the segmentation data, there are a few discrepancies between the glider and grab sample-derived coefficients and the estimated coefficients from surficial geology units. The region between 43°5' N and 43°10' N, 65°W and 64°55' W shows agreement between glider and grab sample-derived reflection coefficients, but is not in agreement with the surficial geology coefficient estimates. As discussed in Section 4.7.2, the shapes and distribution of surficial geology units in *Philibert et al. (2022)* are likely inaccurate both because the basemap data used in this region were published by *King (1970)* and utilized spatial interpolation. While *Philibert et al. (2022)* updated the shapes of the surficial geology units based on recent bathymetry and geomorphology data from

single beam sonar and the GEBCO DEM, no geoacoustic data were used to update the basemap at this location.

Based on the agreement between the reflection coefficients computed from seafloor environmental data and glider-derived effective backscattering coefficient calculations, it is clear that these data are indicative of geoacoustic seafloor properties. Because the glider-derived values are quantitative rather than categorical, these data are more descriptive of seafloor properties than the segmentation results. If more missions of the existing glider SBES data are analyzed, the spatial resolution of these data can be increased. The addition of these effective backscattering coefficient data could increase the spatial resolution and accuracy of sediment distribution models or existing maps.

#### **4.7.4 Limitations**

There are several limitations present when used for the application of seafloor segmentation, both in the data and collection platform. The autonomous gliders used in this survey can only carry so many instruments and both maintain their desired buoyancy and their battery life. A single-beam echo sounder is ideal for these platforms both in weight and power consumption, whereas other systems that may be better suited towards ground discrimination (i.e. multi-beam or split-beam echo sounder) are heavier onboard the vehicle and require a higher payload both to collect and process data (*Finkl and Makowski, 2016; Wöflfl et al., 2019*). The Slocum gliders which collected data for this study were equipped with a number of different instruments (including a hydrophone and sensors which measure environmental data such as oxygen, chlorophyll a, multispectral irradiance, temperature, and salinity), all of which are more suited to the planned purpose of the glider missions than ground-discriminating sonar instruments.

Single-beam echo sounder backscatter has been used to infer surficial and sub-bottom geological properties for nearly a century (*Smith and Nichols, 1953; Smith and Li, 1966*). Early seafloor discrimination often assumed that the seafloor was entirely homogeneous and that the only change in received signal amplitude was caused by sediment type. Later

researchers raised the question: if the geoacoustic properties of the seafloor are affected by surface roughness, sub-bottom properties, benthic ecosystems, and bedforms, as well as grain size and sediment sorting, what do these received signals actually represent (*Gardner et al.*, 1991; *Finkl and Makowski*, 2016)? Because of both large-scale mapping endeavors (including physical sediment grab-samples, underwater photography, and sonar) as well as innovations in sonar technology, many of these questions are more easily answered.

Many limitations arise in the data products themselves that must be accounted for in the interpretation of the segmentation results. Most commercial seafloor discrimination algorithms such as QTC View and RoxAnn use two seafloor returns to categorize seafloor type (*Finkl and Makowski*, 2016; *Serpetti et al.*, 2011; *Lee and Lin*, 2018; *Hamilton*, 2001). These algorithms use statistics describing the shape of the seafloor returns to categorize the backscatter into different groups before assigning seafloor types. QTC in particular uses 166 different statistics, or features, to describe the seafloor returns. The backscatter profiles in both glider missions examined in this survey do not allow for this type of analysis. The seafloor returns produced by the echo sounder in this study are at quite a long range from the transducer such that little to no penetration into the sediment layers are occurring. Thus, there is no second seafloor return to add features to the segmentation analyses. Furthermore, the amplitude of seafloor backscatter returns is not only determined by grain size or bulk sediment density, but also by seafloor roughness, heterogeneity, and porosity (*Jackson and Richardson*, 2006). While each of these properties relates to each other in some way, the interpretation of the backscatter amplitude must always be done whilst keeping in mind other possibilities. While the interpretations presented in this study are in agreement with other data sets and sediment distribution theory, arguments for other interpretations of the clusters (such as bedforms like those found on Browns Bank (*Todd et al.*, 1999)) can be made.

The data used for validation in this thesis also have a number of limitations to consider.

The GEBCO bathymetry is helpful when discussing the relationship between geomorphology and sediment distribution, however, with a resolution of 15 arc seconds (approximately 450 meters), some smaller-scale features are missing. While physical grab samples contain the most quantitative analysis, these data are few and far between. They form a picture of the surficial geology in this region, but these data are too low resolution to make accurate one-to-one comparisons with the glider data at all locations.

The surficial geology of Nova Scotia, New Brunswick, and the Scotian shelf and slope was compiled in a report by *Philibert et al. (2022)*. The authors themselves discuss the limitations of their surficial geology map in the written report. No ground truth data (i.e. sediment grabs and cores, and underwater photography or video) were used in these updates. Rather, *Philibert et al. (2022)* updated these maps with more recently published, higher-resolution surficial geology maps and hydroacoustic data from a number of sources. On the southwestern Scotian Shelf in regions where numerous data and surficial geology maps were lacking, Non-Navigational Bathymetric data (NONNA) from CHS data were used to interpret sediment makeup close to shore and shaded relief data derived from Olex single-beam data were used for interpretation further out on shelves and slopes. At the study site, NONNA data only reach to the northeastern lobe of Roseway Basin, and even these transects are quite far apart, thus the GEBCO DEM remains the highest-resolution bathymetry in the region. Shaded relief maps were used to reshape the surficial geology maps and reinterpret some sediments as recessional moraines and bedrock, but the map in this region remains largely the same as was published in *Fader et al. (2004)*, and long before that in *Drapeau and King (1972)*.

The accuracy of these surficial sediment maps can be assessed by comparing them with grab samples in this region. While large-scale trends remain the same (i.e. softer sediments found in basins; coarser sediments found on banks and basin edges), Figure 4.18 shows that there are discrepancies between the surficial geology units and grab samples, especially around transitional regions from basins to slopes or slopes to banks. Based on Figures 4.19

and 4.20, the glider SBES-derived effective backscattering coefficients are more similar to the grab sample-derived reflection coefficients than either are to the estimates calculated from the surficial geology map. Had the authors of this map included both the grab sample and SBES backscatter data in their updates, it is possible that these anomalies could have been addressed and corrected, allowing for a more accurate depiction of the seabed of the Scotian shelf.

Though these data can be difficult to analyze due to the limitations of the backscatter data, the single-beam echo sounder data from these glider missions are capable of providing information about the geophysical properties of the seafloor. While Roseway Basin is an ideal setting for the case studies presented in this study due to the amount of preexisting data in this region, other glider missions have been carried out in places where less information about the makeup of the seafloor exists. These SBES analyses can therefore add geophysical information to places that may be lacking accurate or updated sediment maps.

## **4.8 Conclusion**

Seafloor backscatter returns from two glider missions were used in a density-based clustering algorithm in order to create surficial sediment distribution maps in Roseway Basin on the Scotian Shelf. The resulting clusters from each mission were compared to each other, and then compared with bathymetry, physical grab samples, and a surficial sediment map. Mission 38 yielded 3 clusters with distinctly different backscatter maximums and Mission 51 yielded 2 distinct clusters. Clusters with lower maximum backscatter values are found in basins and around regions with higher ratios of mud or sand.

The overarching motivation for this chapter was to determine whether data from single-beam sonars calibrated for short-range detection in the water column could be used to extract surficial sediment properties from the seafloor. By using multidimensional scaling and density-based clustering, seafloor backscatter return data were segmented into clusters

representing up to 3 different grain sizes. Therefore, the goal of this chapter was achieved. The seafloor segmentation of Mission 38 was especially successful, with most of the extents of clusters 2 and 3 agreeing with all of the comparison data. Mission 51, while somewhat successful (i.e. finer-grained sediments do occur within the bounds of the comparison data) does not entirely describe the surficial sediment of this region. Thus, future methodology for segmenting different glider missions will likely have to adapt to each unique glider path and study environment.

The CEOTR group has deployed over 126 gliders since 2014 and over 70% of these gliders were equipped with a single beam echo sounder to monitor backscatter in the water column (*CEOTR, 2022*). Until this study, the SBES backscatter data from these surveys have never been used for ground discrimination purposes. Though most of these surveys have historically taken place at Roseway Basin and near Halifax, NS (which has been mapped quite extensively), the CEOTR group also deploys gliders in the Gulf of St. Lawrence, the Laurentian Channel, and even further north in the Labrador Sea. This study shows that these data contain information about sediment properties that can be used as a proxy to determine sediment type and could improve the accuracy of sediment distribution models and surficial geology maps.

---

## CHAPTER 5

---

### CONCLUSIONS

This thesis presents results that can be split into two subjects under the umbrella of novel approaches to seafloor mapping. The first, encompassing Chapters 2 and 3, deals with the design, construction, testing, and utilization of a novel surveying platform while the second, Chapter 4, discusses how SBES profiling data collected using Slocum gliders can be used in novel ways for seafloor mapping. In the first subject, Chapter 2 details the development of the SWASH system, including its design and construction as well as programming and testing the autonomy. The system was tested at Horseshoe Island Park in the Northwest Arm. Several autonomous paths were planned to gauge the success of the hovercraft's autonomy. Following the design and testing of the SWASH system, the platform was used to survey an eelgrass bed in Cole Harbour, Nova Scotia in Chapter 3. Side-scan and single beam sonar imagery and segmentation from side-scan backscatter data were used to identify and spatially map submerged vegetation in this region. Chapter 4 discusses the use of single-beam backscatter data collected from a Slocum glider to map surficial sediment at Roseway Basin. Seafloor sediment type was interpreted for two glider missions using segmentation via a density-based clustering algorithm and effective scattering coefficients.

## **5.1 Key Findings and Implications**

### **5.1.1 Seafloor Mapping with Novel Platforms in Shallow Water**

Throughout the development and testing of the SWASH system in Chapter 2, the hovercraft completed autonomous paths planned in the northwest arm with varying degrees of accuracy. Especially when flown in autonomous mode, this platform tends to drift in other directions than the craft's heading, thus instruments that require a platform moving in a relatively straight line (i.e. side-scan sonar) can not be used if the hovercraft is not flown manually in relatively calm conditions. Instruments that take point measurements can be used successfully in both manual and automatic modes, so this platform could be successfully used as an autonomous craft when equipped with these types of instruments (e.g. SBES).

Chapter 2 determined that the SWASH system could be used as a remotely operated surveying platform in shallow waters. Furthermore, this surveying platform could provide an alternative to crewed vessels, AUVs, or USVs which have propulsion mechanisms under the water that could damage the habitats and environments they are seeking to study. The SWASH system was the first attempt at producing an uncrewed hovercraft platform that could comprehensively map shallow water regions (<3.5m) at high resolutions, and provide data to characterize seafloor properties and submerged vegetation features.

In Cole Harbour and other similar estuarine systems in this region, habitat mapping is infrequent at best, and non-existent at worst. In recent years, Ecology Action Center (EAC) has promoted an eelgrass monitoring citizen science project in which anyone can take pictures of the vegetation and send in their location for a rough estimate of eelgrass presence throughout Nova Scotia (*Ecology Action Center*, 2020). While this could give information on eelgrass beds where the population is in drastic or rapid decline (i.e. large loss of above-ground biomass), more high-resolution maps are needed to determine eelgrass population dynamics. Chapter 3 used statistics calculated on SSS imagery and SBES profiles to identify features on the seafloor that could be interpreted as vegetation.

Although the methods for segmentation and classification for both SSS and SBES data were inspired by successful studies such as *Barrell and Grant (2013)*, *Barrell et al. (2015)*, *Sabol et al. (2002)*, and *Quester Tangent Corp. (2004)*, single-beam segmentation failed to provide clusters that isolated backscatter returns primarily with or without vegetation and were deemed unsuccessful. However, vegetation was identified in SSS and SBES imagery as well as through SSS segmentation results. While at high resolutions, some features identified in segmentation were misidentified as vegetation, in lower resolutions many of these features were averaged out.

Chapter 3 determined that while the sonar instruments and SWASH platform had difficulty surveying in extremely shallow water (<1m), information about the distribution of eelgrass was able to be extracted from the data. Although there are limitations to how the data can be interpreted spatially, the SWASH system was able to survey and provide distribution maps of the submerged vegetation in this region while not disrupting the environment. In general, the complexity of sensing systems on the craft has not been exploited, with payload and power capacity available to integrate more systems, such as oceanographic sensors (i.e. CTD, oxygen, pH, fluorescence). It is likely that with updates and improvements to the system, many of the limitations encountered in this study can be minimized or removed entirely.

The development of an autonomous surveying hovercraft continues past the surveys examined in this thesis. While the original SWASH prototype was retired soon after the final field survey analyzed in Chapter 3, a second prototype is being developed and tested, which has more power, separate steering and thrust motors, a longer telemetry range, and cleaner power sources (battery-powered electric fans rather than a gasoline engine). These design recommendations came from the work described in this thesis. This new prototype alone may solve many of the challenges faced during the surveys examined in this thesis and could allow for habitat mapping in regions like Cole Harbour during high tide when interactions between sonar and vegetation are less likely to decrease data quality.

Developing platforms that can overcome the challenges of surveying in coastal and nearshore regions is imperative for creating high-resolution maps *Patterson et al. (2022); Manley (2016)*. Chapters 2 and 3 exemplified the challenge of developing and testing new and novel platforms. The SWASH system was tested in a sheltered region without vegetation that reached the sonar transducers and was pushed to its limit when utilized for habitat mapping, to the point where some data was unable to be successfully analyzed quantitatively. The reality of creating novel monitoring platforms to solve surveying issues is that they require constant editing, upgrading, and tweaking the systems to keep up with payload and data demands while also catering to the challenges of surveying in areas that may be difficult to maneuver (*Patterson et al., 2022; Finkl and Makowski, 2016*).

### **5.1.2 Novel Approaches to Data Analysis for the Purpose of Seafloor Mapping**

Through the analysis of SBES seafloor returns at Roseway Basin in Chapter 4, clustering results yielded three clusters for Mission 38 and two clusters for Mission 51. Cluster 3, which had the lowest range in backscatter was found in regions with higher percentages of mud or muddy sand, cluster 2 was found in regions where mixed sand and mud (with sand at higher ratios) is dominant, and cluster 1 is found most often in regions where sand or coarse sediments are more likely be found. These clusters generally agree with the descriptions of surficial geology units given by *Philibert et al. (2022)* and with percent grain size from combined grab samples from the GSC and USGS *USGS (2014); GSC (2020)*. Effective scattering coefficients calculated on the seafloor returns for both missions were compared to effective scattering coefficients estimated from grab sample grain sizes and estimated grain size based on descriptions of the surficial geology units (*Philibert et al., 2022; USGS, 2014; GSC, 2020*). With minor spatial differences between the surficial geology maps and glider-derived coefficients, the patterns in sediment distribution agree between the glider data and comparison datasets.

This is the first study in which the single beam backscatter data intended for water

column zooplankton measurements has been used for ground discrimination. The resulting segments and effective scattering coefficients provide an accurate distribution of seafloor reflectivity, which can be related to seafloor hardness. The maps presented in Chapter 4 help to increase the spatiotemporal coverage of seafloor data by introducing a data processing approach that uses existing acoustic backscatter data to infer information about the geoacoustic properties of the seafloor. With so little of the seafloor mapped at a high resolution (*Mayer et al., 2018*) presently, utilizing opportunistic data to its full capabilities can aid in reaching the goals set out by the UN (*Ryabinin et al., 2019*). To date, nearly 100 surveys have been completed by the CEOTR group since 2014 with Slocum gliders equipped with calibrated SBES instruments *CEOTR (2022)*. This number continues to climb when every year, as more surveys are completed with these gliders. If more of these glider missions deployed by CEOTR are analyzed in this way, the spatial resolution of results within the same region will increase, and regions that are less frequently mapped can utilize this information to improve our understanding of surficial sediment patterns and aid in further studies.

## **5.2 The Future of Ocean Mapping with Uncrewed Vehicles**

In 2021, the United Nations proclaimed 2021-2030 an international Decade of Ocean Science for Sustainable Development (*Ryabinin et al., 2019*). This designated the current decade as a time to aim for progress in ocean research and technology to work towards the goals of gaining more knowledge about the global ocean and using such knowledge to inform policy to protect the sea and citizens that rely on it. A “Comprehensive Map of the Ocean” was deemed an important research priority (*Ryabinin et al., 2019*). This includes high-resolution bathymetry and geomorphology of the seafloor, a subject in which significant progress is being made due to the efforts of the Seabed 2030 project (*Mayer et al., 2018; GEBCO Compilation Group, 2022*). However, a completely comprehensive

ocean map does not only include bathymetry, but also geological, physical, and biological properties of the seafloor (Ryabinin *et al.*, 2019). While technological advances should still be made to increase the effectiveness of these platforms, data collected from uncrewed vehicles are already helping to fill spatial and temporal gaps in seafloor biogeophysical data (Finkl and Makowski, 2016; Manley, 2016; Jiang *et al.*, 2021; Patterson *et al.*, 2022). Chapters 2 and 3 show that there is still progress to be made with sampling platforms for mapping in shallow water environments, while Chapter 4 shows that SBES data for water column profiling can be fully exploited for mapping purposes. The current progress made concerning the collection of seafloor biological, geological, and physical data with uncrewed vehicles shows the potential these platforms have for the future of seafloor mapping and exemplifies the likelihood of reaching the goals dictated by the Decade of Ocean Science (Ryabinin *et al.*, 2019).

---

# APPENDIX A

---

## SUPPLEMENTARY MATERIALS FOR CHAPTER 2

The wind speed and direction at the two locations on the Halifax peninsula, mentioned in Chapter 2, are shown in Figure A.1.

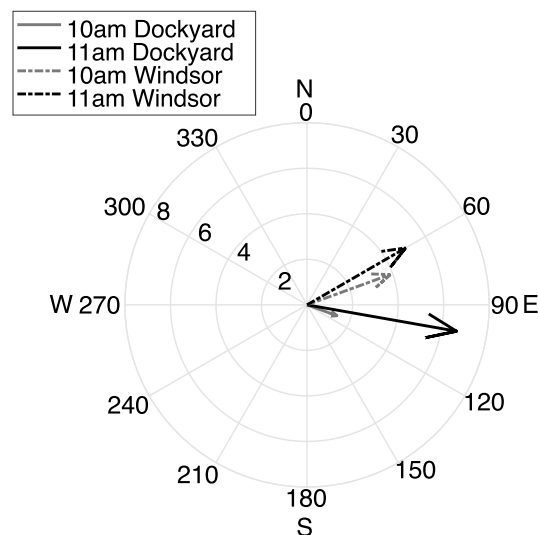


Figure A.1: Wind direction (deg) and speed ( $m s^{-1}$ ) at two locations on the Halifax Peninsula: Halifax Dockyards and Windsor Park at 10 and 11 am on 28 April 2019. The arrows point in the direction in which the wind was blowing, and the arrow length indicates speed. Dashed lines indicate wind from Windsor Park and solid lines indicate wind from the Halifax Dockyards.

Hovercraft tracks and waypoints from autonomous missions 1, 3, and 4 from 28 April 2019 are shown in Figures A.2-A.4.

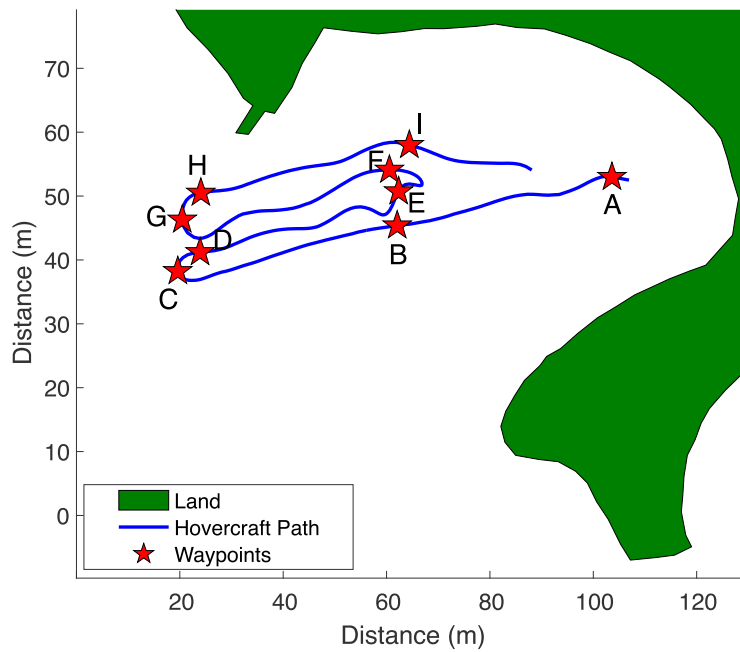


Figure A.2: Hovercraft Mission 1 from 28 April 2019. The hovercraft path is shown via a blue line and the planned waypoints are shown with red stars and labeled.

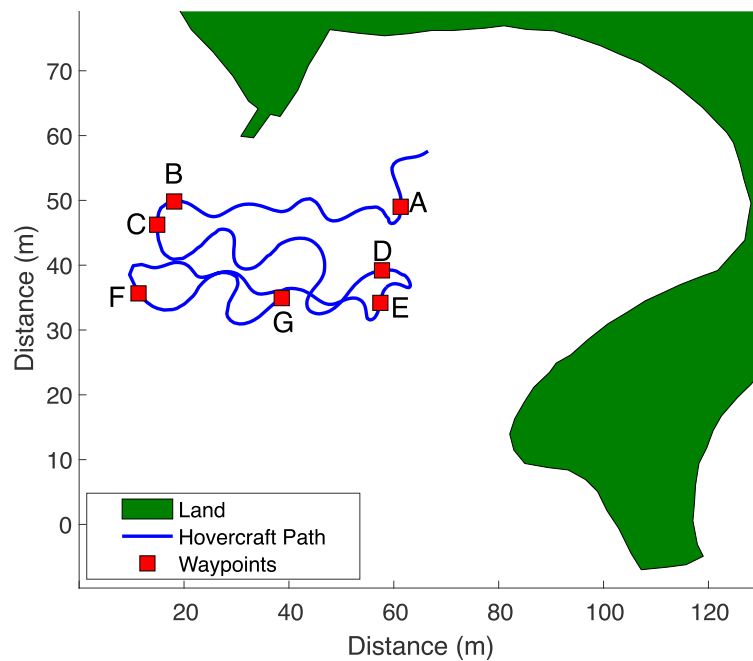


Figure A.3: Hovercraft Mission 4 from 28 April 2019. The hovercraft path is shown via a blue line and the planned waypoints are shown with red squares and labeled.

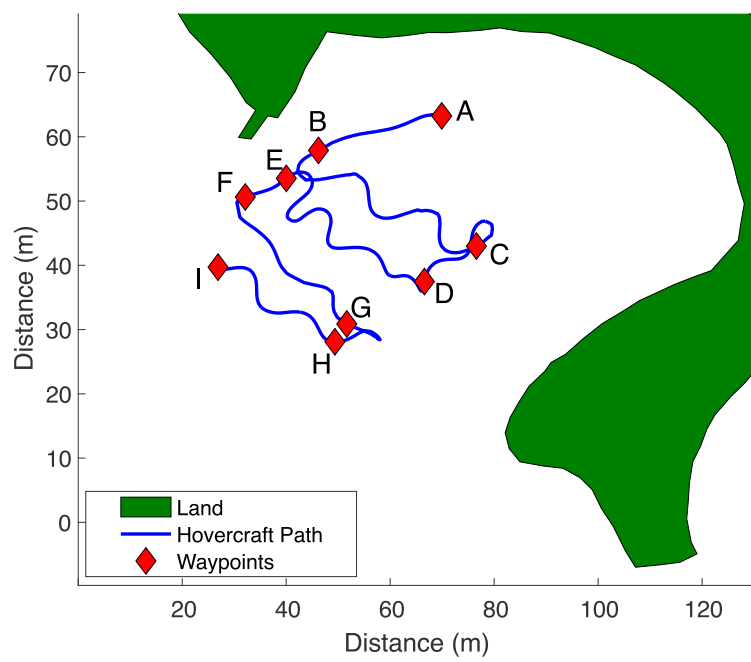


Figure A.4: Hovercraft Mission 4 from 28 April 2019. The hovercraft path is shown via a blue line and the planned waypoints are shown with red diamonds and labeled.

---

## APPENDIX B

---

### SUPPLEMENTAL FIGURES FOR CHAPTER 3

Examples in the range of blade length and canopy height at the eelgrass bed surveyed in Chapter 3 are shown in Figures B.2 and B.1.



Figure B.1: Short eelgrass blade measured from end of roots to tallest blade tip collected on 29, July, 2020. This blade measured approximately 15in long.



Figure B.2: Eelgrass blade measured from end of roots to tallest blade tip collected on 29, July, 2020. This blade measured approximately 56in long.

Side-scan and single beam imagery and SSS segmentation results are presented for the transects not discussed in depth in this study. Table B.1 indicates the deep and shallow transects collected for this study and corresponding figure numbers. Based on where the transects overlap, the imagery and classification from these transects can be compared to each other. The black, dashed lines on the map of the study site and sonar imagery are used as boundaries perpendicular to the shore between which all transects analyzed for this study are found.

<b>Transect Date and Number</b>	<b>Figure(s)</b>
<b>Shallow Transects</b>	
29 July 2020, T2	Figures B.3-B.4
18 August 2020, T1	Figure B.5
29 July 2021, T1, T3	Figures B.6, B.7
<b>Deep Transects</b>	
01 September 2020, T1-T2	Figures B.8-B.9
25 September 2020, T1, T3-T4	Figures B.10-B.12
15 October 2020, T1-T2	Figures B.13-B.14
29 July 2021, T2	Figure B.15

Table B.1: Hovercraft transects not thoroughly discussed in the main text of Chapter 3. The date, transect numbers, and figure references are included in this table.

The shallow water transects not thoroughly discussed in Chapter 3 are shown in Figures B.3- B.7. These transects were collected close to the shore of the tidal flat in water shallower than 1m. The SSS swath width from all of these transects overlaps at multiple points entirely or at one side. Each of these transects shows interaction with the SBES transducer along the transect and interaction with at least one of the SSS transducers.

The deep water transects not thoroughly discussed in Chapter 3 are shown in Figures B.8- B.15. These transects were collected in water depths between 1m-3.5m. Spatially, these transects occur further from the shore of the tidal flat than the shallow water transects and extend into the deeper channel. The SSS swath from some of these transects overlaps entirely or on one side at places.

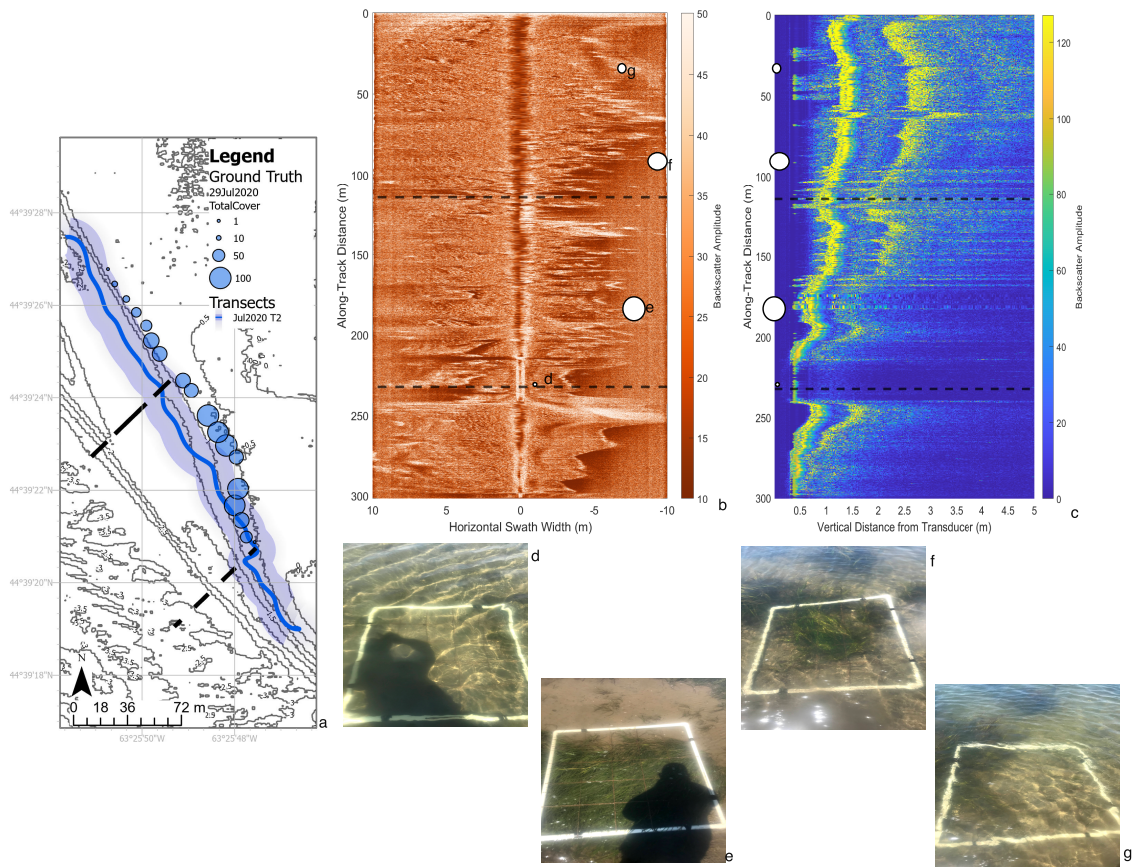


Figure B.3: The (a) hovercraft transect and ground truth values from July 2020, Transect 2, (b) side-scan imagery, (c) single beam imagery, and (d-g) select ground truth photos are shown. Sonar images (a,b) are oriented such that the origin indicates the southernmost point on the transect. White dots on the sonar images (b,c) show the along-track and horizontal positions of the ground truth photos (d-g), and their sizes indicate the total percent cover of 0%, 96%, 68%, and 16%.

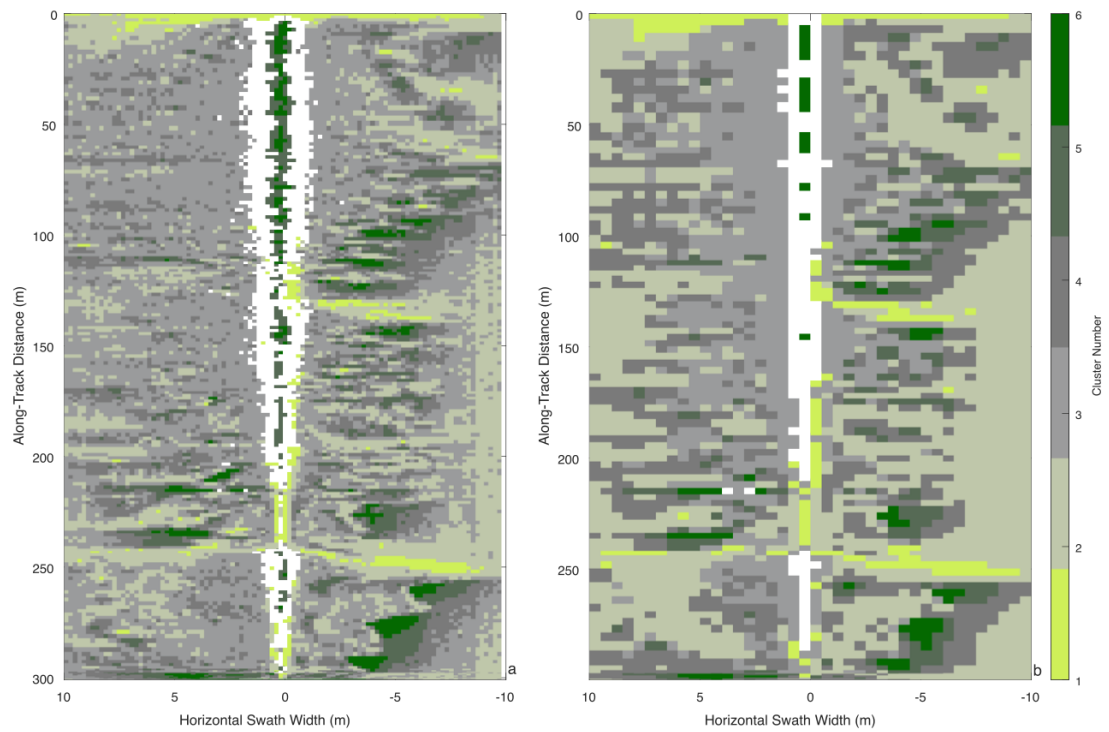


Figure B.4: Side-scan segmentation at a resolution of (a) 50x20 pixels and (b) 100x50 pixels for Scenario C: Transect 2, 29 July 2020. Cluster 1 indicates highlights, clusters 2-4 indicate bare sediment, and clusters 5-6 indicate shadows. Cluster 7 only exists at the nadir and was omitted from these figures.

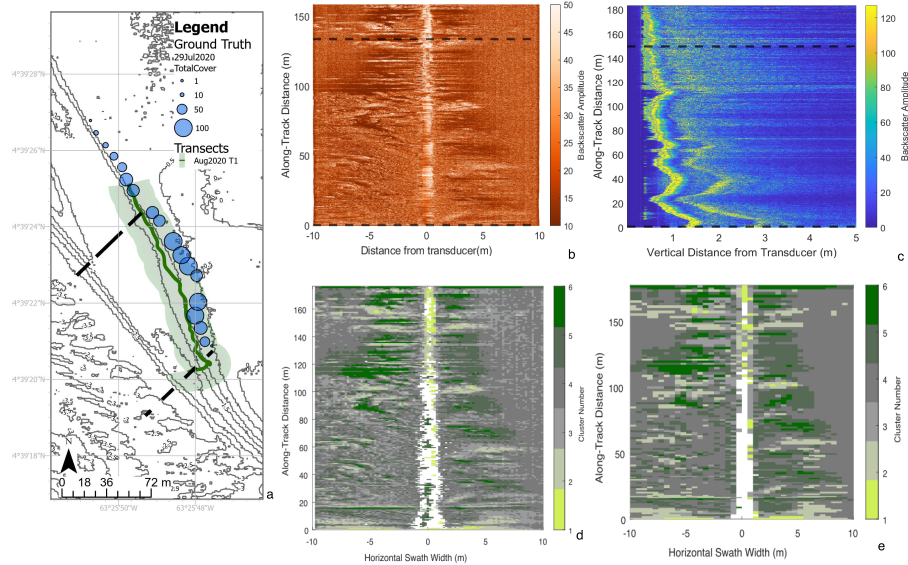


Figure B.5: The (a) hovercraft transect and nearby ground truth data for Transect 1 collected in August 2020, (b) side-scan and (c) single beam imagery, and (d) high-resolution side-scan classification. Sonar imagery and classification transects (b-d) are oriented such that the origin indicates the southernmost point on the transect.

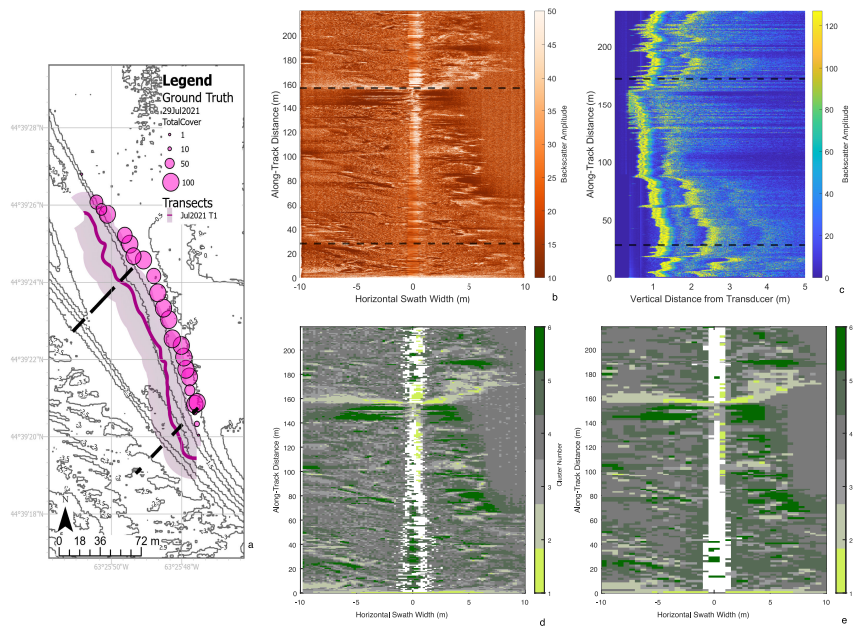


Figure B.6: The (a) hovercraft transect and nearby ground truth data for Transect 1 collected on July 29, 2021, (b) side-scan and (c) single beam imagery, and (d) high-resolution side-scan classification. Sonar imagery and classification transects (b-d) are oriented such that the origin indicates the southernmost point on the transect.

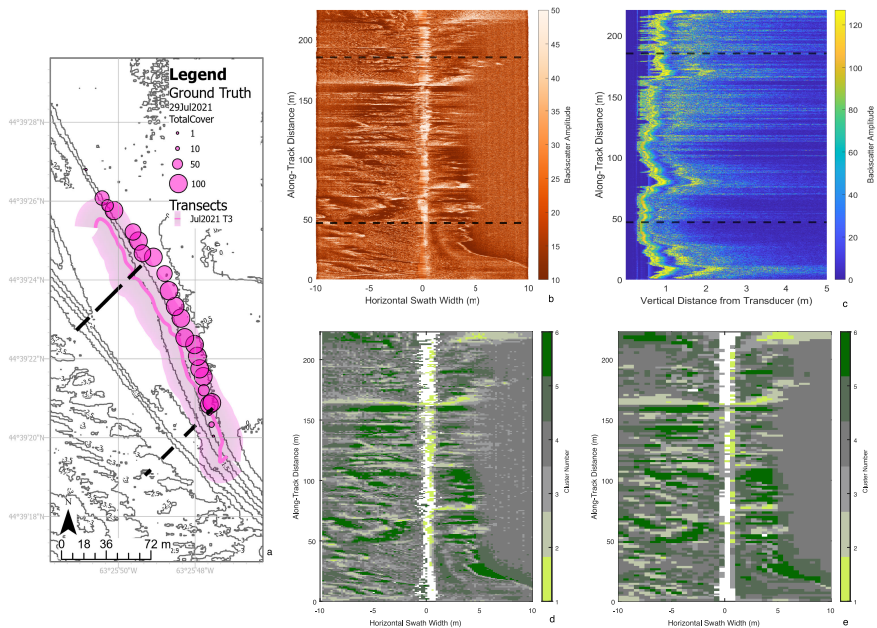


Figure B.7: The (a) hovercraft transect and nearby ground truth data for Transect 3 collected on July 29, 2021, (b) side-scan and (c) single beam imagery, and (d) high-resolution side-scan classification. Sonar imagery and classification transects (b-d) are oriented such that the origin indicates the southernmost point on the transect.

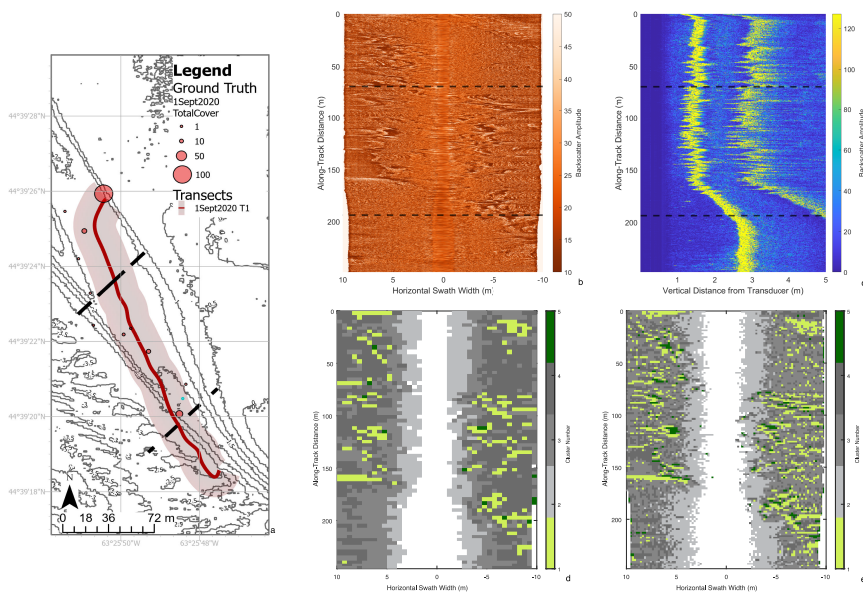


Figure B.8: The (a) hovercraft transect and nearby ground truth data for Transect 1 collected on September 1, 2020, (b) side-scan and (c) single beam imagery, and (d) high-resolution side-scan classification. Sonar imagery and classification transects (b-d) are oriented such that the origin indicates the southernmost point on the transect.

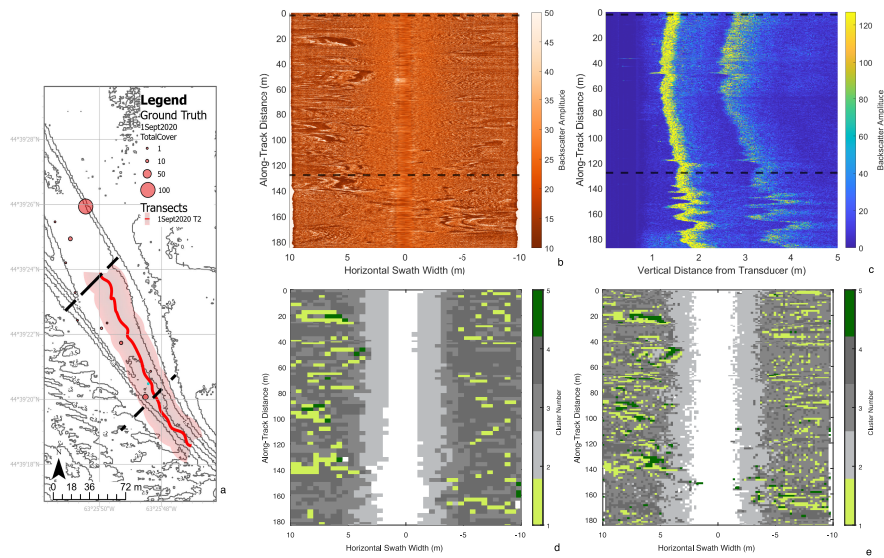


Figure B.9: The (a) hovercraft transect and nearby ground truth data for Transect 2 collected on September 1, 2020, (b) side-scan and (c) single beam imagery, and (d) high-resolution side-scan classification. Sonar imagery and classification transects (b-d) are oriented such that the origin indicates the southernmost point on the transect.

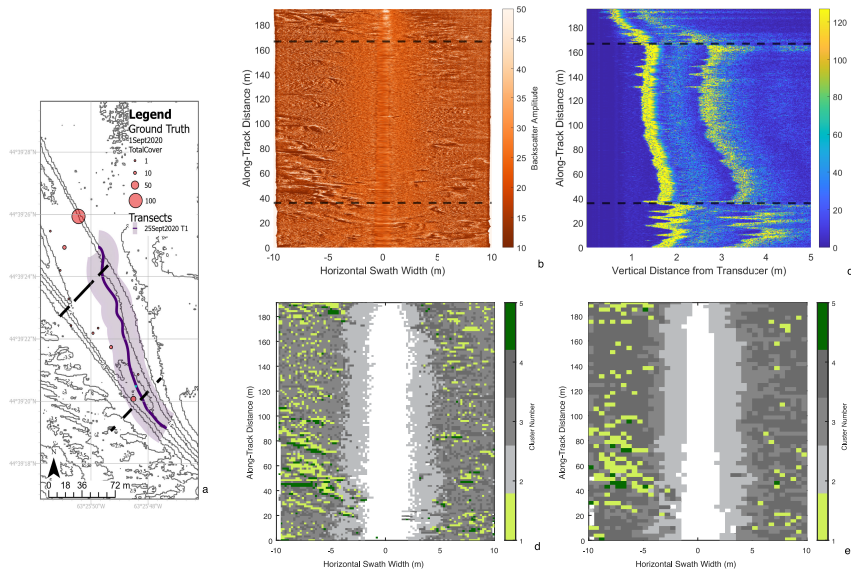


Figure B.10: The (a) hovercraft transect and nearby ground truth data for Transect 1 collected on September 25, 2020, (b) side-scan and (c) single beam imagery, and (d) high-resolution side-scan classification. Sonar imagery and classification transects (b-d) are oriented such that the origin indicates the southernmost point on the transect.

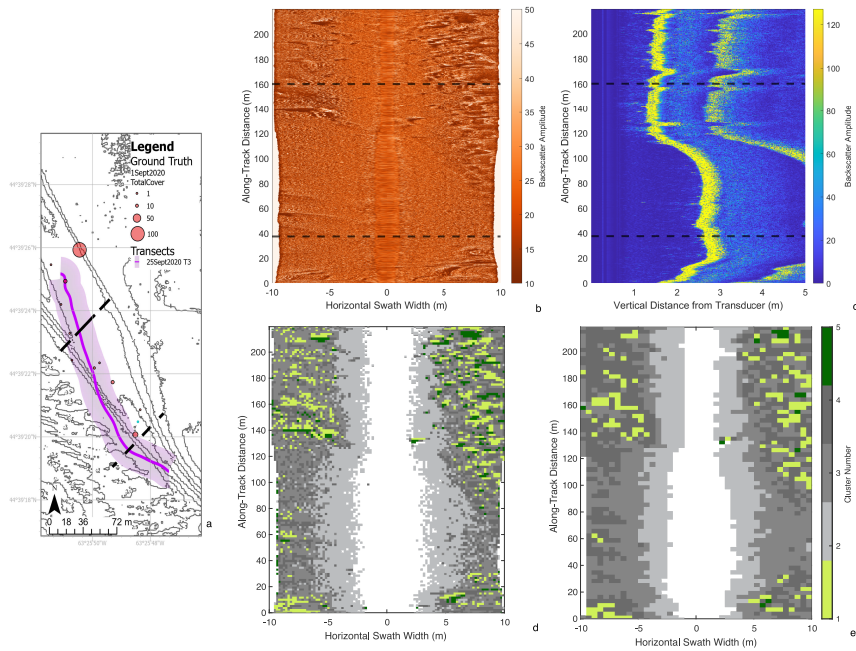


Figure B.11: The (a) hovercraft transect and nearby ground truth data for Transect 3 collected on September 25, 2020, (b) side-scan and (c) single beam imagery, and (d) high-resolution side-scan classification. Sonar imagery and classification transects (b-d) are oriented such that the origin indicates the southernmost point on the transect.

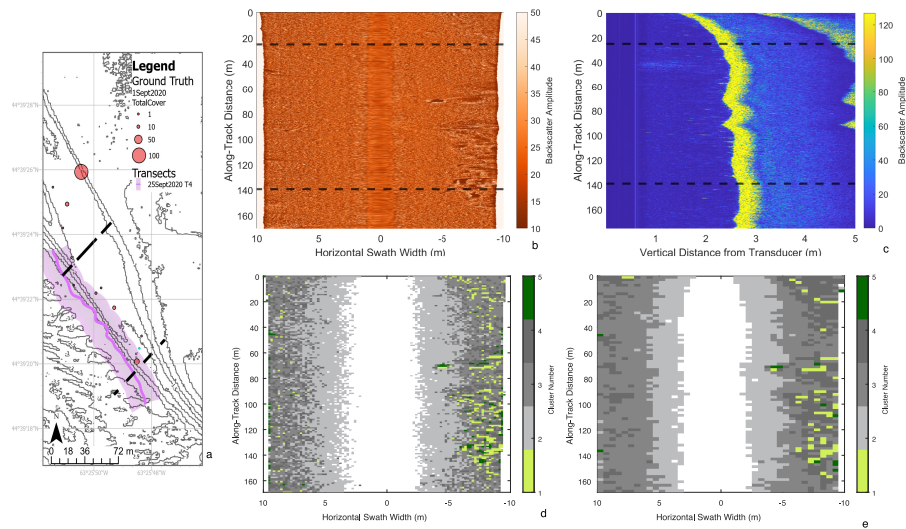


Figure B.12: The (a) hovercraft transect and nearby ground truth data for Transect 4 collected on September 25, 2020, (b) side-scan and (c) single beam imagery, and (d) high-resolution side-scan classification. Sonar imagery and classification transects (b-d) are oriented such that the origin indicates the southernmost point on the transect.

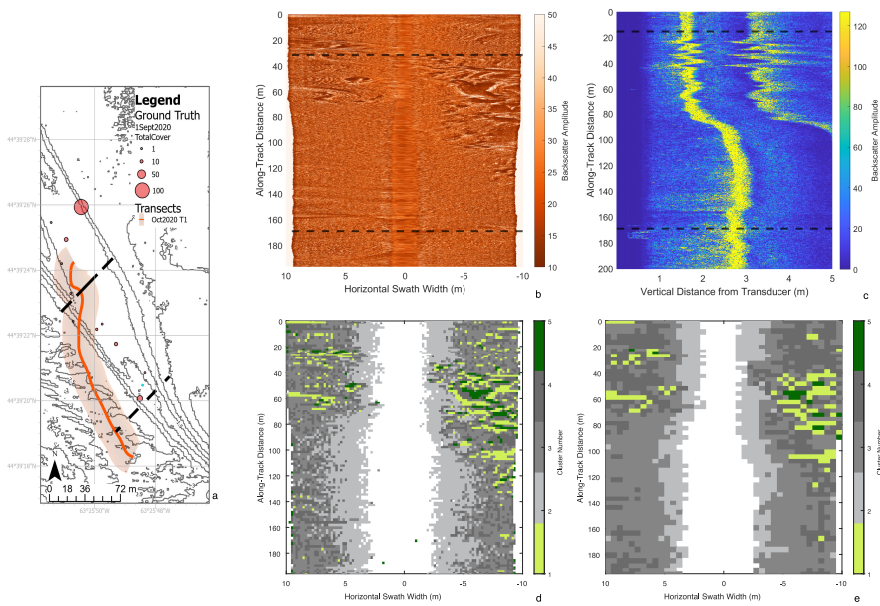


Figure B.13: The (a) hovercraft transect and nearby ground truth data for Transect 1 collected on October 15, 2020, (b) side-scan and (c) single beam imagery, and (d) high-resolution side-scan classification. Sonar imagery and classification transects (b-d) are oriented such that the origin indicates the southernmost point on the transect.

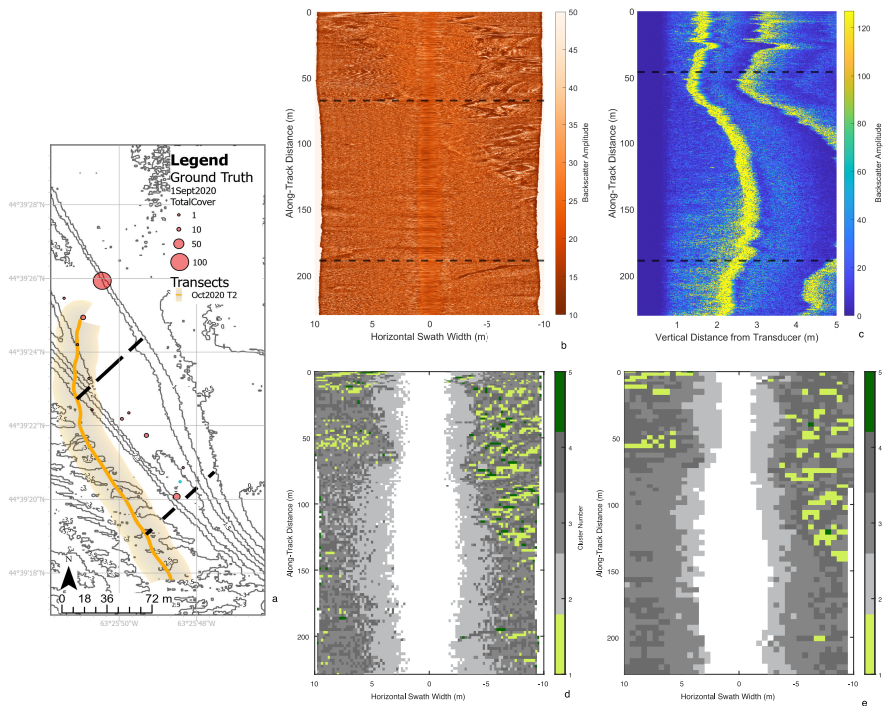


Figure B.14: The (a) hovercraft transect and nearby ground truth data for Transect 2 collected on October 15, 2020, (b) side-scan and (c) single beam imagery, and (d) high-resolution side-scan classification. Sonar imagery and classification transects (b-d) are oriented such that the origin indicates the southernmost point on the transect.

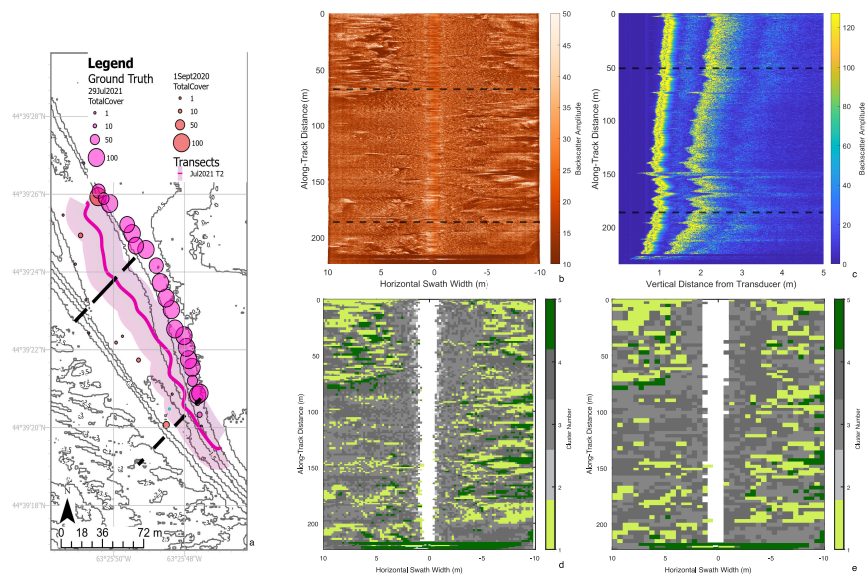


Figure B.15: The (a) hovercraft transect and nearby ground truth data for Transect 2 collected on July 29, 2021, (b) side-scan and (c) single beam imagery, and (d) high-resolution side-scan classification. Sonar imagery and classification transects (b-d) are oriented such that the origin indicates the southernmost point on the transect.

# BIBLIOGRAPHY

- Agrafiotis, P., D. Skarlatos, T. Forbes, C. Poullis, M. Skamantzari, and A. Georgopoulos, Underwater Photogrammetry in Very Shallow Waters: Main challenges and caustics effect removal, in *International Society for Photogrammetry and Remote Sensing*, 2018.
- Ainslie, M. A., and J. G. McColm, A Simplified Formula for Viscous and Chemical Absorption in Sea Water, *The Journal of the Acoustical Society of America*, 103, 1671–1672, 1998.
- Alexandrou, D., and D. Pantzartzis, A Methodology for Acoustic Seafloor Classification, *IEEE Journal of Oceanic Engineering*, 18, 81–86, 1993.
- Amyot, J. R., *Hovercraft Technology, Economics and Applications*, vol. 11, Elsevier, Amsterdam, the Netherlands, 1989.
- ArduPilot Dev, First Drive with Rover, Webpage, 2020, accessed on: 15 June 2020. <https://ardupilot.org/rover/docs/rover-first-drive.html#>.
- Bachman, R., Estimating Velocity Ratio in Marine Sediment, *The Journal of the Acoustical Society of America*, 86, 2029–2032, 1989.
- Bachmann, C. M., M. J. Montes, R. A. Fusina, C. Parrish, J. Sellars, A. Weidemann, W. Goode, C. R. Nichols, P. Woodward, K. McIlhany, et al., Bathymetry Retrieval from Hyperspectral Imagery in the Very Shallow Water Limit: A case study from the 2007 Virginia Coast Reserve (VCR'07) multi-sensor campaign, *Marine Geodesy*, 33, 53–75, 2010.
- Barrell, J., Does Eelgrass (*Zostera marina*) Meet the Criteria as an Ecologically Significant Species?, *DFO Canadian Science Advisory Secretariat Science Advisory Report 2009/018*, Fisheries and Oceans Canada, 2009.
- Barrell, J., and J. Grant, Detecting Hot and Cold Spots in a Seagrass Landscape Using Local Indicators of Spatial Association, *Landscape Ecology*, 28, 2005–2018, 2013.
- Barrell, J., J. Grant, A. Hanson, and M. Mahoney, Evaluating the Complementarity of Acoustic and Satellite Remote Sensing for Seagrass Landscape Mapping, *International Journal of Remote Sensing*, 36, 4069–4094, 2015.
- Berthold, T., A. Leichter, B. Rosenhahn, V. Berkahn, and J. Valerius, Seabed Sediment Classification of Side-Scan Sonar Data Using Convolutional Neural Networks, in *2017 IEEE Symposium Series on Computational Intelligence (SSCI)*, pp. 1–8, Honolulu, HI, 2017.
- Bjørnø, L., T. Neighbors, and D. Bradley, *Applied Underwater Acoustics*, Elsevier, 2017.
- Blondel, P., *The handbook of Sidescan Sonar*, Springer Science & Business Media, 2010.

- Blondel, P., and O. G. Sichi, Textural Analyses of Multibeam Sonar Imagery from Stanton Banks, Northern Ireland Continental Shelf, *Applied Acoustics*, 70, 1288–1297, 2009.
- Botrel, M., C. Hudon, P. P. Biron, and R. Maranger, Combining Quadrat, Rake and Echosounding to Estimate Submerged Aquatic Vegetation Biomass at the Ecosystem Scale, *BioRxiv*, pp. 2022–03, 2022.
- Brown, C. J., A. J. Hewer, W. J. Meadows, D. S. Limpenny, K. M. Cooper, and H. L. Rees, Mapping Seabed Biotopes at Hastings Shingle Bank, Eastern English Channel. Part 1. Assessment using sidescan sonar, *Journal of the Marine Biological Association of the United Kingdom*, 84, 481–488, 2004.
- Brown, C. J., A. Mitchell, D. S. Limpenny, M. R. Robertson, M. Service, and N. Golding, Mapping Seabed Habitats in the Firth of Lorn off the West Coast of Scotland: Evaluation and comparison of habitat maps produced using the acoustic ground-discrimination system, Roxann, and sidescan sonar, *ICES Journal of Marine Science*, 62, 790–802, 2005.
- Brown, C. J., S. J. Smith, P. Lawton, and J. T. Anderson, Benthic Habitat Mapping: A review of progress towards improved understanding of the spatial ecology of the seafloor using acoustic techniques, *Estuarine, Coastal and Shelf Science*, 92, 502–520, 2011.
- Buckingham, B., K. A. Whilden, M. Shields, Y. Liu, S. F. DiMarco, and A. H. Knap, Slocum Glider Observations of the Subsurface Chlorophyll-a Maximum on the Texas Continental Shelf Boundary, in *Global Oceans 2020: Singapore–US Gulf Coast*, pp. 1–5, IEEE, 2020.
- Carvalho, F., M. Y. Gorbunov, M. J. Oliver, C. Haskins, D. Aragon, J. T. Kohut, and O. Schofield, FIRE Glider: Mapping *in situ* chlorophyll variable fluorescence with autonomous underwater gliders, *Limnology and Oceanography: Methods*, 18, 531–545, 2020.
- CEOTR, Coastal Environmental Observation Technology and Research. Glider Deployments, Webpage, 2022, accessed on: 20 November 2022, <https://ceotr.ocean.dal.ca/gliders/deployments/all>.
- Cervenka, P., and C. De Moustier, Sidescan Sonar Image Processing Techniques, *IEEE Journal of Oceanic Engineering*, 18, 108–122, 1993.
- Cochrane, G. R., and K. D. Lafferty, Use of Acoustic Classification of Sidescan Sonar Data for Mapping Benthic Habitat in the Northern Channel Islands, California, *Continental Shelf Research*, 22, 683–690, 2002.
- Collie, J. S., S. J. Hall, M. J. Kaiser, and I. R. Poiner, A Quantitative Analysis of Fishing Impacts on Shelf-Sea Benthos, *Journal of Animal Ecology*, 69, 785–798, 2000.
- Collier, J., and C. J. Brown, Correlation of Sidescan Backscatter with Grain Size Distribution of Surficial Seabed Sediments, *Marine Geology*, 214, 431–449, 2005.

- Collier, J., and S. Humber, Time-Lapse Side-Scan Sonar Imaging of Bleached Coral Reefs: A case study from the seychelles, *Remote Sensing of Environment*, 108, 339–356, 2007.
- Costello, C. T., and W. J. Kenworthy, Twelve-Year Mapping and Change Analysis of Eelgrass (*Zostera marina*) Areal Abundance in Massachusetts (USA) Identifies Statewide Declines, *Estuaries and Coasts*, 34, 232–242, 2011.
- D’amico, A., and R. Pittenger, A Brief History of Active Sonar, *Aquatic Mammals*, 35, 426–434, 2009.
- Davis, R., M. Baumgartner, A. Comeau, D. Cunningham, K. Davies, A. Furlong, H. Johnson, S. L’Orsa, T. Ross, C. Taggart, et al., Tracking whales on the Scotian Shelf using Passive Acoustic Monitoring on Ocean Gliders, in *OCEANS 2016 MTS/IEEE*, pp. 1–4, IEEE, Monterey, CA, 2016.
- Dernie, K., M. Kaiser, and R. Warwick, Recovery Rates of Benthic Communities Following Physical Disturbance, *Journal of Animal Ecology*, 72, 1043–1056, 2003.
- Descamp, P., G. Pergent, L. Ballesta, and M. Foulquié, Underwater Acoustic Positioning Systems as Tool for *Posidonia oceanica* Beds Survey, *Comptes Rendus Biologies*, 328, 75–80, 2005.
- Diebel, J., Representing Attitude: Euler angles, unit quaternions, and rotation vectors, *Matrix*, 58, 1–35, 2006.
- Dierssen, H. M., and A. E. Theberge, Bathymetry: Assessing methods, *Encyclopedia of Ocean Sciences*, 2014.
- DJI, Products DJI Drones, Webpage, 2021, accessed on: 02 June 2021. <https://store.dji.com/ca/product/matrice-600-pro>.
- Drapeau, G., and L. King, Surficial Geology of the Yarmouth-Browns Bank Map Area, *Geological Survey of Canada Paper 0072-0024*, Atlantic Geosciences Centre, Bedford Institute of Oceanography, 1972.
- Ecology Action Center, EAC Eelgrass Monitoring Project, Webpage, 2020, accessed on: 09 December 2020. <https://www.inaturalist.org/projects/eac-eelgrass-monitoring-project>.
- Eriander, L., E. Infantes, M. Olofsson, J. L. Olsen, and P.-O. Moksnes, Assessing Methods for Restoration of Eelgrass (*Zostera marina* L.) in a Cold Temperate Region, *Journal of Experimental Marine Biology and Ecology*, 479, 76–88, 2016.
- Fader, G., T. Lynds, R. Miller, D. Parrott, S. Hynes, and A. Sherin, Scotian Shelf Regional Surficial Geology Compilation, *Open File 4671*, Geological Survey of Canada, 2004.
- Ferreira, H., C. Almeida, A. Martins, J. Almeida, N. Dias, A. Dias, and E. Silva, Autonomous Bathymetry for Risk Assessment with ROAZ Robotic Surface Vehicle, in *Oceans 2009-Europe*, pp. 1–6, IEEE, 2009.

- Ferretti, R., M. Bibuli, M. Caccia, D. Chiarella, A. Odetti, A. Ranieri, E. Zereik, and G. Bruzzone, Towards *Posidonia* Meadows Detection, Mapping and Automatic Recognition Using Unmanned Marine Vehicles, *IFAC-PapersOnLine*, 50, 12386–12391, 2017.
- Finkl, C. W., and C. Makowski (Eds.), *Seafloor Mapping Along Continental Shelves: Research and techniques for visualizing benthic environments*, vol. 13, Springer, Switzerland, 2016.
- Fisher, F., and V. Simmons, Sound absorption in sea water, *The Journal of the Acoustical Society of America*, 62, 558–564, 1977.
- Foster-Smith, R. L., C. J. Brown, W. J. Meadows, W. H. White, and D. S. Limpenny, Mapping Seabed Biotopes at Two Spatial Scales in the Eastern English Channel. Part 2. Comparison of two acoustic ground discrimination systems, *Journal of the Marine Biological Association of the United Kingdom*, 84, 489–500, 2004.
- Galvez, D. S., S. Papenmeier, L. Sander, H. C. Hass, V. Fofonova, A. Bartholomä, and K. H. Wiltshire, Ensemble Mapping and Change Analysis of the Seafloor Sediment Distribution in the Sylt Outer Reef, German North Sea from 2016 to 2018, *Water*, 13, 2254, 2021.
- Garbary, D. J., A. G. Miller, J. Williams, and N. R. Seymour, Drastic Decline of an Extensive Eelgrass Bed in Nova Scotia Due to the Activity of the Invasive Green crab (*Carcinus maenas*), *Marine Biology*, 161, 3–15, 2014.
- Gardner, J. V., M. E. Field, H. Lee, B. E. Edwards, D. G. Masson, N. Kenyon, and R. B. Kidd, Ground-truthing 6.5 kHz Side Scan Sonographs: What are we really imaging?, *Journal of Geophysical Research: Solid Earth*, 96, 5955–5974, 1991.
- Gavazzi, G. M., F. Madricardo, L. Janowski, A. Kruss, P. Blondel, M. Sigovini, and F. Foglini, Evaluation of Seabed Mapping Methods for Fine-Scale Classification of Extremely Shallow Benthic Habitats—Application to the Venice Lagoon, Italy, *Estuarine, Coastal and Shelf Science*, 170, 45–60, 2016.
- GEBCO Compilation Group, GEBCO 2022 Grid, 2022.
- Giordano, F., G. Mattei, C. Parente, F. Peluso, and R. Santamaria, Integrating Sensors Into a Marine Drone for Bathymetric 3D Surveys in Shallow Waters, *Sensors*, 16, 41, 2016.
- Green, E. P., and F. T. Short, *World Atlas of Seagrasses*, University of California Press, 2003.
- Greene, A., A. F. Rahman, R. Kline, and M. S. Rahman, Side Scan Sonar: A cost-efficient alternative method for measuring seagrass cover in shallow environments, *Estuarine, Coastal and Shelf Science*, 207, 250–258, 2018.
- Grizzle, R. E., M. A. Brodeur, H. A. Abeels, and J. K. Greene, Bottom Habitat Mapping Using Towed Underwater Videography: Subtidal oyster reefs as an example application, *Journal of Coastal Research*, 24, 103–109, 2008.

- GSC, Geological Survey of Canada. Seabed Grain Size Analyses, Offshore Canada, Webpage, 2020, contains information licensed under the Open Government Licence – Canada. <https://open.canada.ca/data/en/dataset/093e437e-ee35-fd32-7da0-807848ec5d64/resource/15551b16-ed4f-411c-9318-b0781a75cb25>.
- Guenther, G. C., Airborne Lidar Bathymetry, in *Digital Elevation Model Technologies and Applications: The DEM users manual*, vol. 2, p. 655, Citeseer, 2007.
- Gumusay, M. U., T. Bakirman, I. Tuney Kizilkaya, and N. O. Aykut, A Review of Seagrass Detection, Mapping and Monitoring Applications Using Acoustic Systems, *European Journal of Remote Sensing*, 52, 1–29, 2019.
- Halifax Regional Municipality, LiDAR DEM 1m 2018, 2020, accessed on: 15 August 2022. Data retrieved from Halifax Open Data Files, <https://www.halifax.ca/home/open-data/open-data-files>.
- Hamilton, E., and R. Bachman, Sound Velocity and Related Properties of Marine Sediments, *The Journal of the Acoustical Society of America*, 72, 1891–1904, 1982.
- Hamilton, L., Acoustic Seabed Classification Systems, *Tech. Rep. DSTO-TN-0401*, Defense Science and Technology Organisation, Aeronautical and Maritime Research Laboratory, Victoria, Australia, 2001.
- Han, G., C. G. Hannah, J. W. Loder, and P. C. Smith, Seasonal variation of the three-dimensional mean circulation over the scotian shelf, *Journal of Geophysical Research: Oceans*, 102, 1011–1025, 1997.
- Hanson, A. R., Status and Conservation of Eelgrass, *Zostera Marina*, in Eastern Canada, *Technical Report Series No. 412*, Environment Canada, Canadian Wildlife Service, Atlantic Region, 2004.
- Hassan, S. R., M. Zakaria, M. Arshad, and Z. Abd Aziz, Evaluation of Propulsion System Used in URRG-Autonomous Surface Vessel (ASV), *Procedia Engineering*, 41, 607–613, 2012.
- IHO, *International Hydrographic Organization Standards for Hydrographic Surveys S-44*, International Hydrographic Organization, Monte Carlo, Monaco, 2020.
- Jackson, D., and M. Richardson, *High-Frequency Seafloor Acoustics*, Springer, New York, NY, USA, 2006.
- Javaid, M. Y., M. Ovinis, T. Nagarajan, and F. B. Hashim, Underwater Gliders: A review, in *MATEC Web of Conferences*, vol. 13, p. 02020, EDP Sciences, 2014.
- Jiang, Y.-M., S. E. Dosso, J. Bonnel, P. S. Wilson, and D. P. Knobles, Passive Acoustic Glider for Seabed Characterization at the New England Mud Patch, *IEEE Journal of Oceanic Engineering*, 2021.

- Jo, W., Y. Hoashi, L. L. P. Aguilar, M. Postigo-Malaga, J. M. Garcia-Bravo, and B.-C. Min, A Low-Cost and Small USV Platform for Water Quality Monitoring, *HardwareX*, 6, 2019.
- Jolliffe, I. P., Littoral and Offshore Sediment Transport, *Progress in Physical Geography*, 2, 264–308, 1978.
- Jones, M. E., L. Miller, D. L. Woodruff, and D. W. Ewert, Mapping of Submerged Aquatic Vegetation Using Autonomous Underwater Vehicles in Nearshore Regions, in *OCEANS 2007*, pp. 1–7, 2007.
- Kerfoot, J., and D. Aragon, Long Duration Underwater Glider Dataset: Indian Ocean from Perth, Australia to Mirissa, Sri Lanka, *Data in Brief*, 31, 2020.
- Kimball, P., J. Bailey, S. Das, R. Geyer, T. Harrison, C. Kunz, K. Manganini, K. Mankoff, K. Samuelson, T. Sayre-McCord, et al., The WHOI Jetyak: An autonomous surface vehicle for oceanographic research in shallow or dangerous waters, in *2014 IEEE/OES Autonomous Underwater Vehicles (AUV)*, pp. 1–7, IEEE, 2014.
- King, L. H., Surficial Geology of the Halifax-Sable Island Map Area, *Marine Science Papers 1*, Canada Department of Energy, Mines, and Resources, Marine Sciences Branch, 1970.
- King, L. H., and B. MacLean, Pockmarks on the Scotian Shelf, *Geological Society of America Bulletin*, 81, 3141–3148, 1970.
- Kostylev, V. E., B. J. Todd, G. B. Fader, R. Courtney, G. D. Cameron, and R. A. Pickrill, Benthic Habitat Mapping on the Scotian Shelf Based on Multibeam Bathymetry, Surficial Geology and Sea Floor Photographs, *Marine Ecology Progress Series*, 219, 121–137, 2001.
- Krapivner, R., Origin of Diamictons on the Barents Sea Shelf, *Lithology and Mineral Resources*, 44, 120–134, 2009.
- Lee, W. S., and C. Y. Lin, Mapping of Tropical Marine Benthic Habitat: Hydroacoustic classification of coral reefs environment using single-beam (RoxAnn) system, *Continental Shelf Research*, 170, 1–10, 2018.
- Leica Geosystems AG, Bathymetric LiDAR Sensors, Webpage, 2021, accessed on: 02 June 2021. <https://leica-geosystems.com/products/airborne-systems/bathymetric-lidar-sensors/leica-chiroptera>.
- Li, P., and Y. Zhang, A New Model of Gaps Patching for Side-Scan Sonar Images Based on Heading Optimization Strategy, in *2020 IEEE International Conference on Mechatronics and Automation (ICMA)*, pp. 345–349, IEEE, 2020.

- Loder, J. W., G. Han, C. G. Hannah, D. A. Greenberg, and P. C. Smith, Hydrography and baroclinic circulation in the scotian shelf region: winter versus summer, *Canadian Journal of Fisheries and Aquatic Sciences*, 54, 40–56, 1997.
- Lucieer, V., Object-Oriented Classification of Sidescan Sonar Data for Mapping Benthic Marine Habitats, *International Journal of Remote Sensing*, 29, 905–921, 2008.
- Lurton, X., *Underwater Acoustics: An introduction*, vol. 1, Springer, 2002.
- Lyons, A. P., A. L. Anderson, and T. H. Orsi, Modeling Acoustic Volume Backscatter from Two Shallow-Water Marine Environments by Side-Scan Sonar, in *Proceedings of OCEANS'94*, vol. 1, pp. I-862, IEEE, 1994.
- Lyons, A. P., S. F. Johnson, D. A. Abraham, and E. Pouliquen, High-Frequency Scattered Envelope Statistics of Patchy Seafloors, *IEEE Journal of Oceanic Engineering*, 34, 451–458, 2009.
- Malthus, T. J., and E. Karpouzli, On the Benefits of Using Both Dual Frequency Side Scan Sonar and Optical Signatures for the Discrimination of Coral Reef Benthic Communities, *Advances in Sonar Technology*, pp. 165–186, 2009.
- Malthus, T. J., and P. J. Mumby, Remote Sensing of the Coastal Zone: An overview and priorities for future research, *International Journal of Remote Sensing*, 24, 2805–2815, 2003.
- Manley, J. E., Unmanned Maritime Vehicles, 20 years of commercial and technical evolution, in *OCEANS 2016 MTS/IEEE Monterey*, pp. 1–6, IEEE, 2016.
- Marbà, N., D. Krause-Jensen, P. Masqué, and C. M. Duarte, Expanding Greenland Seagrass Meadows Contribute New Sediment Carbon Sinks, *Scientific Reports*, 8, 14024, 2018.
- Martinez, M. L., A. Intralawan, G. Vazquez, O. Perez-Maqueo, P. Sutton, and R. Landgrave, The Coasts of Our World: Ecological, economic and social importance, *Ecological Economics*, 63, 254–272, 2007.
- Mayer, L., M. Jakobsson, G. Allen, B. Dorschel, R. Falconer, V. Ferrini, G. Lamarche, H. Snaith, and P. Weatherall, The Nippon Foundation—GEBCO Seabed 2030 Project: The quest to see the world's oceans completely mapped by 2030, *Geosciences*, 8, 63, 2018.
- Mayer, L. A., Frontiers in Seafloor Mapping and Visualization, *Marine Geophysical Researches*, 27, 7–17, 2006.
- McCarthy, E., Acoustic Characterization of Submerged Aquatic Vegetation, *NATO. SACLANTCEN*, 1997.
- McCarthy, E., and B. Sabol, Acoustic Characterization of Submerged Aquatic Vegetation: Military and environmental monitoring applications, in *OCEANS 2000 MTS/IEEE Conference and Exhibition. Conference Proceedings (Cat. No. 00CH37158)*, vol. 3, pp. 1957–1961, IEEE, 2000.

- McCullough, D., Significant Habitats: Atlantic Coast Initiative (SHACI), Halifax Regional Municipality, units 4-6, *Canadian Manuscript Report of Fisheries and Aquatic Sciences 2724*, Fisheries & Oceans Canada, Maritimes Region, Oceans & Habitat Branch, Bedford Institute of Oceanography, 2005.
- McKenzie, L. J., M. A. Finkbeiner, and H. Kirkman, Methods for Mapping Seagrass Distribution, *Global Seagrass Research Methods*, pp. 101–121, 2001.
- McLarty, M. J., D. Gonzalez-Socoloske, A. Alvarez-Alemán, and J. Angulo-Valdés, Manatee Habitat Characterization Using Side-Scan Sonar, *Journal of the Marine Biological Association of the United Kingdom*, 100, 173–179, 2020.
- Medwin, H., C. S. Clay, and T. K. Stanton, *Fundamentals of Acoustical Oceanography*, Acoustical Society of America, 1999.
- Mehvar, S., T. Filatova, A. Dastgheib, E. De Ruyter van Steveninck, and R. Ranasinghe, Quantifying Economic Value of Coastal Ecosystem Services: A review, *Journal of marine science and engineering*, 6, 5, 2018.
- Misiuk, B., V. Lecours, and T. Bell, A Multiscale Approach to Mapping Seabed Sediments, *PLoS One*, 13, 2018.
- Möller, T., Mapping and Modelling of the Spatial Distribution of Benthic Macrovegetation in the NE Baltic Sea with a Special Focus on the Eelgrass *Zostera marina* Linnaeus, 1753, Ph.D. thesis, Tartu University, 2017.
- Monpert, C., M. Legris, C. Noel, B. Zerr, and J. M. Le Caillec, Studying and Modeling of Submerged Aquatic Vegetation Environments Seen by a Single Beam Echosounder, in *Proceedings of Meetings on Acoustics ECUA2012*, vol. 17, Acoustical Society of America, 2012.
- Montefalcone, M., A. Rovere, V. Parravicini, G. Albertelli, C. Morri, and C. N. Bianchi, Reprint of “Evaluating Change in Seagrass Meadows: A time-framed comparison of side scan sonar maps”, *Aquatic Botany*, 115, 36–44, 2014.
- Moore, K. A., and F. T. Short, *Zostera: Biology, ecology, and management*, in *Seagrasses: Biology, Ecology and Conservation*, pp. 361–386, Springer, 2007.
- Murphy, G. E., J. C. Dunic, E. M. Adamczyk, S. J. Bittick, I. M. Côté, J. Cristiani, E. A. Geissinger, R. S. Gregory, H. K. Lotze, M. I. O’Connor, et al., From Coast to Coast to Coast: Ecology and management of seagrass ecosystems across Canada, *Facets*, 6, 139–179, 2021.
- Murray, R. M., Z. Li, S. S. Sastry, and S. S. Sastry, *A Mathematical Introduction to Robotic Manipulation*, CRC Press, 1994.
- National Defence, R. C. A. F., Flying a Drone in the Halifax Region – Royal Canadian Air Force, 2021, accessed on: November 2021, <https://www.canada.ca/en/air-force/corporate/wings/12-wing/drone.html>.

- Neckles, H. A., A. R. Hanson, P. Colarusso, R. N. Buchsbaum, and F. T. e. Short, Status, Trends, and Conservation of Eelgrass in Atlantic Canada and the Northeastern United States: Workshop report, *Tech. rep.*, University of Southern Maine, Muskie School of Public Service, Casco Bay Estuary Partnership, Portland, Maine, USA, 2009.
- Norton, A. R., Acoustic Methods for Mapping and Characterizing Submerged Aquatic Vegetation Using a Multibeam Echosounder, Ph.D. thesis, University of New Hampshire, 2019.
- O'Brien, J. M., M. C. Wong, and R. R. Stanley, Fine-Scale Ensemble Species Distribution Modelling of Eelgrass (*Zostera marina*) to Inform Nearshore Conservation Planning and Habitat Management, *Frontiers in Marine Science*, 9, 19, 2022.
- Ocheltree, K., and L. Frizzel, Sound Field Calculation for Rectangular Sources, *IEEE Transactions on Ultrasonics, Ferroelectrics, and Frequency Control*, 36, 242–248, 1989.
- O'Neill, J. D., and M. Costa, Mapping Eelgrass (*Zostera marina*) in the Gulf Islands National Park Reserve of Canada Using High Spatial Resolution Satellite and Airborne Imagery, *Remote Sensing of Environment*, 133, 152–167, 2013.
- Oversmith, R., and R. Leadon, Concept Whisper: A buoyancy-propelled, multiple cycle undersea glider vehicle., *Technical report gd/c-62-206a*, General Dynamics/Convair, San Diego, 1962.
- Paling, E., M. Fonseca, M. van Katwijk, and M. van Kuelen, Coastal Wetland Restoration and Management: Seagrass restoration., in *Coastal Wetlands: An integrated ecosystems approach*, edited by G. Perilo, E. Wolanski, D. Cahoon, and M. Brinson, pp. 685–714, Elsevier BV, Amsterdam, the Netherlands, 2009.
- Patterson, R. G., E. Lawson, V. Udyawer, G. B. Brassington, R. A. Groom, and H. A. Campbell, Uncrewed Surface Vessel Technological Diffusion Depends on Cross-Sectoral Investment in Open-Ocean Archetypes: A systematic review of USV applications and drivers, *Frontiers in Marine Science*, 8, 2015, 2022.
- Pattiaratchi, C., L. M. Woo, P. G. Thomson, K. K. Hong, and D. Stanley, Ocean Glider Observations around Australia, *Oceanography*, 30, 90–91, 2017.
- Philibert, G., B. Todd, D. Campbell, E. King, A. Normandeau, S. Hayward, E. Patton, and L. Campbell, Updated Surficial Geology Compilation of the Scotian Shelf Bioregion, Offshore Nova Scotia and New Brunswick, *Open file 8911*, Geological Survey of Canada, 2022.
- Piper, D., *The Marine Geology of the Inner Scotian Shelf Off the South Shore, Nova Scotia*, Paper 85–19, Geological Survey of Canada, 1986.
- Piper, D. J., Seabed Geology of the Canadian Eastern Continental Shelf, *Continental Shelf Research*, 11, 1013–1035, 1991.

- Preston, J., A. Christney, L. Beran, and W. Collins, Statistical Seabed Segmentation—From images and echoes to objective clustering, in *Proceedings of the Seventh European Conference on Underwater Acoustics, ECUA*, pp. 5–8, Citeseer, 2004.
- Quester Tangent Corp., *QTC IMPACT. Acoustic Seabed Classification. User Manual*, Quester Tangent Corporation, Marine Technology Centre, Sidney, BC, Canada, 2004.
- Rains, C., Analytical Investigation of the Performance Characteristics of Cyclic Glide Undersea Vehicles, *Tech. rep.*, General Dynamics Corp, San Diego, CA, 1968.
- Record, S., N. Charney, R. Zakaria, and A. M. Ellison, Projecting Global Mangrove Species and Community Distributions Under Climate Change, *Ecosphere*, 4, 1–23, 2013.
- Reed IV, T. B., and D. Hussong, Digital Image Processing Techniques for Enhancement and Classification of SeaMARC II Side Scan Sonar Imagery, *Journal of Geophysical Research: Solid Earth*, 94, 7469–7490, 1989.
- Rende, S. F., A. Bosman, R. Di Mento, F. Bruno, A. Lagudi, A. D. Irving, L. Dattola, L. D. Giambattista, P. Lanera, R. Proietti, et al., Ultra-High-Resolution Mapping of *Posidonia oceanica* (L.) Delile Meadows through Acoustic, Optical Data and Object-Based Image Classification, *Journal of Marine Science and Engineering*, 8, 647, 2020.
- Röhr, M. E., C. Boström, P. Canal-Vergés, and M. Holmer, Blue Carbon Stocks in Baltic Sea Eelgrass (*Zostera marina*) Meadows, *Biogeosciences*, 13, 6139–6153, 2016.
- Röhr, M. E., M. Holmer, J. K. Baum, M. Björk, K. Boyer, D. Chin, L. Chalifour, S. Cimon, M. Cusson, M. Dahl, et al., Blue Carbon Storage Capacity of Temperate Eelgrass (*Zostera marina*) Meadows, *Global Biogeochemical Cycles*, 32, 1457–1475, 2018.
- Ryabinin, V., J. Barbière, P. Haugan, G. Kullenberg, N. Smith, C. McLean, A. Troisi, A. Fischer, S. Aricò, T. Aarup, et al., The UN Decade of Ocean Science for Sustainable Development, *Frontiers in Marine Science*, 6, 470, 2019.
- Sabol, B., M. Graves, and J. Preston, Evaluation of Multibeam Hydrographic System Performance in Dense Seagrass, *Proceedings Hydro2007. May*, pp. 14–17, 2007.
- Sabol, B. M., R. Eddie Melton, R. Chamberlain, P. Doering, and K. Haurert, Evaluation of a Digital Echo Sounder System for Detection of Submersed Aquatic Vegetation, *Estuaries*, 25, 133–141, 2002.
- Sarnthein, M., R. Gersonde, S. Niebler, U. Pflaumann, R. Spielhagen, J. Thiede, G. Wefer, and M. Weinelt, Overview of Glacial Atlantic Ocean Mapping (GLAMAP 2000), *Paleoceanography*, 18, 2003.
- Saxena, N., Atanu Basu, A Review of Shallow-Water Mapping Systems, *Marine Geodesy*, 22, 249–257, 1999.

- Schubert, P. R., W. Hukriede, R. Karez, and T. B. Reusch, Mapping and Modeling Eelgrass *Zostera marina* Distribution in the Western Baltic Sea, *Marine Ecology Progress Series*, 522, 79–95, 2015.
- Serpetti, N., M. Heath, E. Armstrong, and U. Witte, Blending Single Beam RoxAnn and Multi-Beam Swathe QTC Hydro-Acoustic Discrimination Techniques for the Stonehaven Area, Scotland, UK, *Journal of Sea Research*, 65, 442–455, 2011.
- Sheffer, T., and H. Guterman, Geometrical Correction of Side-Scan Sonar Images, in *2018 IEEE International Conference on the Science of Electrical Engineering in Israel (ICSEE)*, pp. 1–5, Eliat, Israel, 2018.
- Short, F., T. Carruthers, W. Dennison, and M. Waycott, Global Seagrass Distribution and Diversity: A bioregional model, *Journal of Experimental Marine Biology and Ecology*, 350, 3–20, 2007.
- Short, F. T., A. C. Mathieson, and J. Nelson, Recurrence of the Eelgrass Wasting Disease at the Border of New Hampshire and Maine, USA, *Marine Ecology Progress Series*, pp. 89–92, 1986.
- Short, F. T., L. K. Muehlstein, and D. Porter, Eelgrass Wasting Disease: Cause and recurrence of a marine epidemic, *The Biological Bulletin*, 173, 557–562, 1987.
- Siderius, M., C. H. Harrison, and M. B. Porter, A Passive Fathometer Technique for Imaging Seabed Layering Using Ambient Noise, *The Journal of the Acoustical Society of America*, 120, 1315–1323, 2006.
- Smith, D. T., and W. Li, Echo-Sounding and Sea-Floor Sediments, *Marine Geology*, 4, 353–364, 1966.
- Smith, W., and H. B. Nichols, Mapping Water-Saturated Sediments by Sonic Methods, *The Scientific Monthly*, 77, 36–41, 1953.
- Stępień, B., Can a Ship Be its Own Captain? Safe manning of autonomous and uncrewed vessels, *Marine Policy*, 148, 105451, 2023.
- Stevens, A. W., J. R. Lacy, D. P. Finlayson, and G. Gelfenbaum, Evaluation of a Single-Beam Sonar System to Map Seagrass at Two Sites in Northern Puget Sound, Washington, *Tech. rep.*, US Geological Survey, 2008.
- Stocks, J., M. Rodgers, J. Pera, and D. Gilligan, Monitoring Aquatic Plants: An evaluation of hydroacoustic, on-site digitising and airborne remote sensing techniques, *Knowledge & Management of Aquatic Ecosystems*, p. 27, 2019.
- Symons, W. O., E. J. Sumner, P. J. Talling, M. J. Cartigny, and M. A. Clare, Large-Scale Sediment Waves and Scours on the Modern Seafloor and Their Implications for the Prevalence of Supercritical Flows, *Marine Geology*, 371, 130–148, 2016.

- Thayer, G. W., W. J. Kenworthy, and M. S. Fonseca, The Ecology of Eelgrass Meadows of the Atlantic Coast: A community profile, *Tech. Rep. FWS/OBS-84/02*, Fish and Wildlife Service, 1984.
- Thom, R. M., S. L. Blanton, D. L. Woodruff, G. D. Williams, and A. B. Borde, Carbon Sinks in Nearshore Marine Vegetated Ecosystems, in *Proceedings of First National Conference on Carbon Sequestration*, pp. 14–17, 2001.
- Todd, B., Recessional Moraines on the Southern Scotian Shelf of Atlantic Canada, *Geological Society, London, Memoirs*, 46, 257–258, 2016.
- Todd, B. J., and V. E. Kostylev, Surficial Geology and Benthic Habitat of the German Bank Seabed, Scotian Shelf, Canada, *Continental Shelf Research*, 31, S54–S68, 2011.
- Todd, B. J., G. B. Fader, R. C. Courtney, and R. A. Pickrill, Quaternary Geology and Surficial Sediment Processes, Browns Bank, Scotian Shelf, Based on Multibeam Bathymetry, *Marine Geology*, 162, 165–214, 1999.
- Tyler-Walters, H., and C. Arnold, Sensitivity of Intertidal Benthic Habitats to Impacts Caused by Access to Fishing Grounds, *Ccw policy research report no. 08/13*, Cyngor Cefn Gwlad Cymru/Countryside Council for Wales, 2008.
- Universal Hovercraft, Hovercraft kits, Webpage, 2016, accessed on: 02 June 2021. <https://web.archive.org/web/20210930052354/https://www.hovercraft.com/content/>.
- USGS, U.S. Geological Survey East-Coast Sediment Analysis: Procedures, database, and GIS data, *Open-file report: 2005-1001*, U.S. Geological Survey, Coastal and Marine Geology Program, Woods Hole Coastal and Marine Science Center, Woods Hole, MA, 2014.
- Valentine, P. C., Sediment Classification and the Characterization, Identification, and Mapping of Geologic Substrates for the Glaciated Gulf of Maine Seabed and Other Terrains, Providing a Physical Framework for Ecological Research and Seabed Management, *U.S. Geological Survey Scientific Investigations Report 2019-5073*, US Geological Survey, 2019.
- van der Hoop, J. M., A. S. M. Vanderlaan, and C. T. Taggart, Absolute Probability Estimates of Lethal Vessel Strikes to North Atlantic Right Whales in Roseway Basin, Scotian Shelf, *Ecological Applications*, 22, 2021–2033, 2012.
- Vandermeulen, H., Drop and Towed Camera Systems for Ground-Truthing High Frequency Sidescan in Shallow Waters, *Tech. Rep. 2687*, Canadian Technical Report Fisheries and Aquatic Sciences, Dartmouth, Nova Scotia, 2007.
- Vandermeulen, H., An Echosounder System Ground-Truthed by Towfish Data: A method to map larger nearshore areas, *Canadian Technical Report of Fisheries and Aquatic Sciences 2958*, Fisheries and Oceans Canada, 2011.

- Vandermeulen, H., Bay-Scale Assessment of Eelgrass Beds using Sidescan and Video, *Helgoland Marine Research*, 68, 559–569, 2014.
- Vilks, G., and M. A. Rashid, Post-Glacial Paleo-Oceanography of Emerald Basin, Scotian Shelf, *Canadian Journal of Earth Sciences*, 13, 1256–1267, 1976.
- Wang, Z., S. F. DiMarco, and K. Polzin, Turbulence Observations in the Northern Gulf of Mexico from a Slocum Glider, in *2018 OCEANS-MTS/IEEE Kobe Techno-Oceans (OTO)*, pp. 1–6, IEEE, 2018.
- Webb, D. C., P. J. Simonetti, and C. P. Jones, SLOCUM: An underwater glider propelled by environmental energy, *IEEE Journal of Oceanic Engineering*, 26, 447–452, 2001.
- Whipp, E., and D. Horne, Digitising of Side-Scan Sonar Signals, *Ultrasonics*, 14, 201–204, 1976.
- Wilson, K. L., and H. K. Lotze, Climate Change Projections Reveal Range Shifts of Eelgrass *Zostera marina* in the Northwest Atlantic, *Marine Ecology Progress Series*, 620, 47–62, 2019.
- Wilson, K. L., M. A. Skinner, and H. K. Lotze, Eelgrass (*Zostera marina*) and Benthic Habitat Mapping in Atlantic Canada Using High-Resolution SPOT 6/7 Satellite Imagery, *Estuarine, Coastal and Shelf Science*, 226, 2019.
- Wöfl, A.-C., H. Snaith, S. Amirebrahimi, C. W. Devey, B. Dorschel, V. Ferrini, V. A. Huvenne, M. Jakobsson, J. Jencks, G. Johnston, et al., Seafloor Mapping—The challenge of a truly global ocean bathymetry, *Frontiers in Marine Science*, p. 283, 2019.
- Zemanek, J., Beam Behavior within the Nearfield of a Vibrating Piston, *The Journal of the Acoustical Society of America*, 49, 181–191, 1971.
- Zhou, M., R. Bachmayer, and B. deYoung, Mapping the Underside of an Iceberg with a Modified Underwater Glider, *Journal of Field Robotics*, 36, 1102–1117, 2019.
- Zolich, A., A. Faltynkova, G. Johnsen, and T. A. Johansen, Portable Catamaran Drone — An uncrewed sampling vehicle for micro-plastics and aquaculture research, in *OCEANS 2022, Hampton Roads*, pp. 1–6, 2022.